A Study of Finite Amplitude Bifurcations
in Plane Poiseuille Flow

Thesis by

Israel Soibelman

In Partial Fulfillment of the Requirements

for the Degree of

Doctor of Philosophy

California Institute of Technology

Pasadena, California

June, 1989

(Submitted 6 March 1989)

I would like to dedicate this thesis to the memory of my father, Samuel Soibelman. This thesis would never have been possible without my father's love and support.

Acknowledgments

Finally, my parents' support and love have been present at every stage of my education. They have given me more than I can ever give back. This thesis is for them.

Abstract

Plane Poiseuille flow is known to be linearly unstable at a Reynolds number of 5772.22 (Drazin and Reid, 1981). In experiments, however, transition to turbulent flow is seen to occur at a Reynolds number of 1000 (Nishioka and Asai, 1985). In an attempt at resolving this conflict, we search for 2D and 3D nonlinear bifurcations at low Reynolds number.

Because we wish to study secondary bifurcations, we compute the 2D waves which bifurcate from plane Poiseuille flow. These waves were first computed by Zahn, *et al.*, (1975), and the critical Reynolds number, based on constant pressure, was found to be approximately 2900. To find 2D bifurcations, we study the 2D superharmonic stability of the 2D waves. The stability picture is found to change when switching from a constant flux to constant average pressure gradient boundary condition. For both boundary conditions, we find several Hopf bifurcations on the upper branch of the 2D waves.

We calculate the periodic orbits which emanate from these bifurcations and find that no branch extends below the critical 2D wave Reynolds number. We also confirm the results of Jimenez (1988) who detected one of the branches we calculate with a time dependent formulation.

To find 3D bifurcations, we study the 3D stability of the 2D waves. Several branches of 3D waves are calculated. In particular, we study 3D bifurcations at a spanwise wave number of 2. No bifurcations are found to branches which extend to low Reynolds numbers. This result conflicts with those found by Rozhdestvensky

and Simakin (1984) with a time dependent formulation.

In addition, we study 3D oblique waves and 3D standing-travelling waves (standing in the streamwise direction) which bifurcate from plane Poiseuille flow. In particular, we study the bifurcation at spanwise wave numbers greater than .365. Contrary to Bridges' (1988) hypothesis, we find that no branches extend to low Reynolds numbers.

Table of Contents

List of Figures

List of Tables

CHAPTER 1

INTRODUCTION

1.1 Background

The work presented in this thesis was motivated by the wish to understand the transition of laminar flow to turbulent flow. In particular, we studied the transition in plane Poiseuille flow. Plane Poiseuille flow is the viscous incompressible flow between two parallel surfaces driven by a streamwise pressure gradient The basic laminar solution for the velocity field is the parabolic profile:

$$u = U_0(1 - (\frac{y}{h})^2). \tag{1.1}$$

A linear stability analysis is the natural first step in studying stability of the basic flow. The governing equation for disturbances of the form

$$u' = \hat{u}(y)e^{i\alpha(x-ct)}, \tag{1.2}$$

where α is the wave number, and c is the complex phase speed is the Orr-Sommerfeld equation. Only one eigenfunction of the Orr-Sommerfeld equation is known to have an eigenvalue whose imaginary part, $c_i(\alpha, Re)$, becomes greater than zero in a region of the $\alpha-Re$ plane. The curve of marginal stability, $c_i = 0$, is known as the Orr-Sommerfeld curve, and the critical Reynolds number of this curve is 5772.22.

Unlike other hydrodynamic stability problems, however, the critical Reynolds number from linear theory does not coincide with the experimentally observed critical Reynolds number. The experiments of Carlson, Widnall and Peeters (1982), Nishioka and Asai (1985) and Alavyoon, Henningson and Alfresson (1986) all found that transition occurred at a Reynolds number of ≈ 1000. This result suggests that

finite amplitude disturbances initiate transition. This conclusion is also supported by the observations from plane Couette flow. Plane Couette flow is the viscous incompressible flow between two parallel surfaces driven by the upper surface. The basic laminar solution for the velocity field is

$$u = U_0 \frac{y}{h}. \tag{1.3}$$

Plane Couette flow is believed to be linearly stable for all Reynolds number (Drazin and Reid, 1981). The experiments by Reichardt (1956), however, suggest that transition to turbulence is very much like in plane Poisueille flow and occurs at a Reynolds number of ≈ 750. Clearly, finite amplitude disturbances need to be investigated to understand transition.

Two approaches have been used to study finite amplitude disturbances. One approach utilizes a time dependent simulation of the disturbance. This approach has been used by Orszag and Kells (1980), Orszag and Patera (1980, 1981, 1983) Kleiser (1982), Kim (1983), Zang (1987) and many other authors. The advantages to this approach include the feasibility of high resolution numerics, and the ability to simulate experimentally observed flows. The disadvantages to such an approach include the inability to calculate unstable solutions, the lack of control over the solution form, and the difficulty in implementing a parameter search of steady solutions.

An alternative approach, which we use in this thesis, is to search for specific types of steady equilibrium solutions. This approach is capable of computing unstable solutions. Also, the solution form can be specified, and a parameter search can be undertaken in solution space. A major disadvantage to this approach is that high resolution numerics are not feasible. As will be shown in Chapter 2, however, with spectral methods a few modes is often sufficient to give good qualitative and

sometimes quantitative results. Also, as will be discussed in the conclusion, a new approach by Tuckerman (1988) may allow increased resolution.

Our approach to finding the finite amplitude disturbances is based on Saffman's (1983) hypothesis that the transition from the laminar state to the turbulent state is dependent on the existence of intermediate vortical states and that turbulence is the 3D instability of these states and their complex interactions. Typical examples of vortical states are states that are periodic in space or time. The exact nature of the vortical state remains to be determined. Among the many possibilities are 2D travelling waves, quasi-periodic solutions, and 3D waves. Although the form of the vortical solution is not specified, the solution should exist at low Reynolds number and the instabilities of the solution should grow on the convective time scale observed in experiment.

1.2 2D Waves

Perhaps the simplest example of a vortical state are 2D travelling waves. Chen and Joseph (1973) have proved the existence of 2D travelling waves which bifurcate from plane Poiseuille flow. The first attempt to compute these waves was undertaken by Noether (1921). Noether studied equilibrium wave disturbances by truncating his equations at $N = 1$ modes. This approximation is called the "mean-field" approximation and only takes into account the correction to the mean flow and the first harmonic. No higher harmonics are studied. Using asymptotic expansions, Meksyn and Stuart (1951) obtained an approximate solution for these equations. They found that the critical Reynolds number decreases with increasing disturbance amplitude. The critical Reynolds number eventually passes through a minimum and increases. The minimum critical Reynolds number was found to be at a wave number larger than the the maximum wave number on the Orr-Sommerfeld curve. These results have been confirmed by more accurate numerical computations. Zahn

et al. (1974) numerically computed these solutions with $N = 2$ modes and found a nonlinear neutral surface. Herbert (1977) used a spectral collocation technique and found the minimum critical Reynolds number of the neutral surface at $Re = 2935$ and $\alpha = 1.323$ for $N = 4$ modes. These calculations show that the critical Reynolds number is reduced by a factor of 2 from linear theory. However, there is still a large discrepancy from the experimentally observed critical Reynolds number of ≈ 1000. In addition, the results show that even for a low mode calculation, $N = 1$ modes, the results are qualitatively correct. This is surprising because the first nonlinear interaction involves the second harmonic.

In Chapter 2, we repeat these calculations because we wish to study 2D and 3D secondary bifurcations. Because we use a more accurate procedure to determine the minimum critical Reynolds number, there are slight discrepancies between Herbert's results and our own. In addition, we outline the numerical scheme which will be implemented throughout this thesis.

The discussion so far has been restricted to steady 2D waves. Orszag and Patera (1983) found quasi-steady 2D waves well below $Re = 2900$. These states eventually decay, but the decay rate is so slow that Orszag and Patera consider these states effectively steady. A 3D stability analysis is then implemented under the assumption that the variation of the 2D states on the slow time scale can be neglected. As an initial condition for this stability analysis, they give a 2D state which is steady. The 3D perturbations are found to grow explosively if the amplitude of the 2D state is sufficiently large and the decay rate of the 2D state is sufficiently small. Below a Reynolds number of ≈ 1000, they find that the 2D decay rate is too large for 3D disturbances to grow. Based on these results, Orszag and Patera propose that transition is the 3D instability of 2D quasi-steady flows.

There are, however, two criticisms which can be made of their hypothesis.

pothesis. First, no 2D quasi-steady states have been found in circular Poiseuille flow. Therefore, in circular Poiseuille flow multiple time scaling arguments can not be applied. Secondly, no detailed multiple time scaling analysis has been undertaken to support the hypothesis in plane Poiseuille flow. With these reservations in mind and with the motivation of Saffman's hypothesis, we searched for steady solutions at low Reynolds number.

1.3 2D Stability of 2D Waves

In Chapter 3, we study the 2D superharmonic stability of 2D waves. Previously, stability studies have focused on the 3D stability of 2D waves. This is due to the observation that 3D instabilities grow on a convective time scale while 2D disturbances grow on a viscous time scale. As transition occurs explosively, it is believed that 3D instabilities initiate transition. Our efforts, however, are aimed at finding bifurcations to 2D states which exist at low Reynolds number. The 3D instabilities of these states would then lead to transition.

In Chapter 3, we show that the 2D stability of 2D waves is a function of how the 2D wave Reynolds number is defined. The Reynolds number can be defined by fixing the spatially averaged pressure gradient to be constant, or by fixing the flux to be constant. For constant flux disturbances, we find that the lower branch of the 2D waves is unstable and a stability transition occurs at the limit point. The upper branch, however, does not remain stable. Two different pairs of complex conjugate eigenvalues cross the imaginary axis transversely. These crossings are Hopf bifurcations.

For constant pressure disturbances, we find that the lower branch is unstable but a stability transition does not occur at the nose. Instead, another eigenvalue becomes unstable at the nose. The two unstable eigenvalues merge on the upper branch and subsequently stabilize. The point of stabilization is a Hopf bifurcation.

This Hopf bifurcation is not present in the case of constant flux disturbances. In addition, we find two more Hopf bifurcations on the upper branch. These Hopf bifurcations correspond to the Hopf bifurcations found in constant flux disturbances. These Hopf bifurcations imply the existence of periodic solutions or, in a fixed frame of reference, quasi-periodic solutions.

1.4 Qausi-Periodic Solutions

In Chapter 4, we compute the branches of periodic orbits which emanate from the Hopf bifurcations found in Chapter 3. Previously, Jimenez (1988) found one of the branches that we detected with a time dependent code. The Hopf bifurcation for this branch occurs on the upper branch of the 2D waves at a Reynolds number of ≈ 5000 and $\alpha = 1.0$. Jimenez found that the Reynolds number of this branch increases with increasing amplitude. We confirm these results with our calculation. In addition, we calculate several branches which Jimenez did not detect. Because Jimenez used a time dependent code, he could not detect Hopf bifurcations once the upper branch destabilizes. Also, Jimenez used a Reynolds number based on constant flux. A new Hopf bifurcation appears when the Reynolds number is based on constant pressure. For the Hopf bifurcation which only appears in the case of constant pressure disturbances, we find that the Reynolds number initially decreases. A limit point, however, is reached before the Reynolds number extends below the critical 2D wave Reynolds number. For the other branches of periodic orbits, the Reynolds number increases with increasing amplitude and does not turn back.

1.5 3D Waves

In Chapter 5, we study 3D steady waves. The existence of 3D steady waves below the critical 2D wave Reynolds number is still an open question. Goldshtik and Shtern (1983) found steady subharmonic 3D waves (subharmonic in the stream-wise direction) down to a Reynolds number of 1000. Pugh (1988) repeated this

calculation and found the same low Reynolds number solutions when using similar resolution. Upon increasing resolution, however, the result disappeared. Pugh's results are also questionable since he ignored the effect of the superharmonic components in the 3D waves.

Orszag and Kells (1981) found that no stable steady superharmonic 3D solutions exist below the critical Reynolds number of the 2D waves. Rozhdesventsky and Simakin (1984), however, implemented the same numerical scheme and found stable 3D states down to a Reynolds number of 1313 (based on constant flux) at a spanwise wave number of 2 and a streamwise wave number of 1.25. Pugh (1988) investigated 3D waves which bifurcate from the 2D wave for spanwise wave numbers less than .5. No 3D waves were found below the critical 2D wave Reynolds number.

In an attempt to confirm Rozhdesventsky and Simakin's results, we investigated the 3D waves which bifurcate from 2D waves at high spanwise wave numbers ($\beta = 2$). We found that no 3D waves extended below the critical 2D wave Reynolds number.

Bridges (1988) has proved the existence of oblique 3D waves and 3D waves which are travelling in the streamwise direction and standing in the spanwise direction (we will refer to these as standing travelling waves, STW) which bifurcate from plane Poiseuille flow. Bridges observed that for spanwise wave numbers greater than .365, it appeared possible that the STW would extend to low Reynolds number. In Chapter 5, we calculate the branches of oblique waves and STW which bifurcate from plane Poiseuille flow. We show that no 3D oblique or 3D STW extend below the critical Reynolds number of the 2D waves.

CHAPTER 2

STEADY TWO DIMENSIONAL WAVES

2.1 Introduction

In this chapter, we study the 2D waves found in plane Poiseuille flow. Chen and Joseph (1973) proved the existence of 2D travelling wave solutions which bifurcate from plane Poiseuille flow. In addition, several authors have conducted numerical studies of these waves (for example, Zahn et al., 1974, Herbert 1976, Milinazzo and Saffman , 1985). We repeat these calculations to study 2D and 3D secondary bifurcations.

We show that our calculations yield results which are in good agreement with the previous efforts, and we discuss some important features of these flows.

2.2 Calculation of Bifurcation Points

Consider the 2D Navier-Stokes equations for incompressible flow in the primitive variable formulation:

$$\rho(\frac{\partial \tilde{u}}{\partial t} + (\tilde{u} \cdot \nabla)\tilde{u}) = -\nabla p + \mu \nabla^2 \tilde{u} \tag{2.1}$$

$$\nabla \cdot \tilde{u} = 0, \tag{2.2}$$

where $\tilde{u} = (u, v)$. One can introduce a streamfunction $\psi(x, y, t)$ by letting

$$u = \frac{\partial \psi}{\partial y}$$
$$v = -\frac{\partial \psi}{\partial x}. \tag{2.3}$$

With the streamfunction as defined by (2.3), one can transform (2.1)–(2.2) to the equivalent streamfunction formulation:

$$\frac{\partial \nabla^2 \Psi}{\partial t} + \Psi_y \nabla^2 \Psi_x - \Psi_x \nabla^2 \Psi_y = \nu \nabla^4 \Psi, \tag{2.4}$$
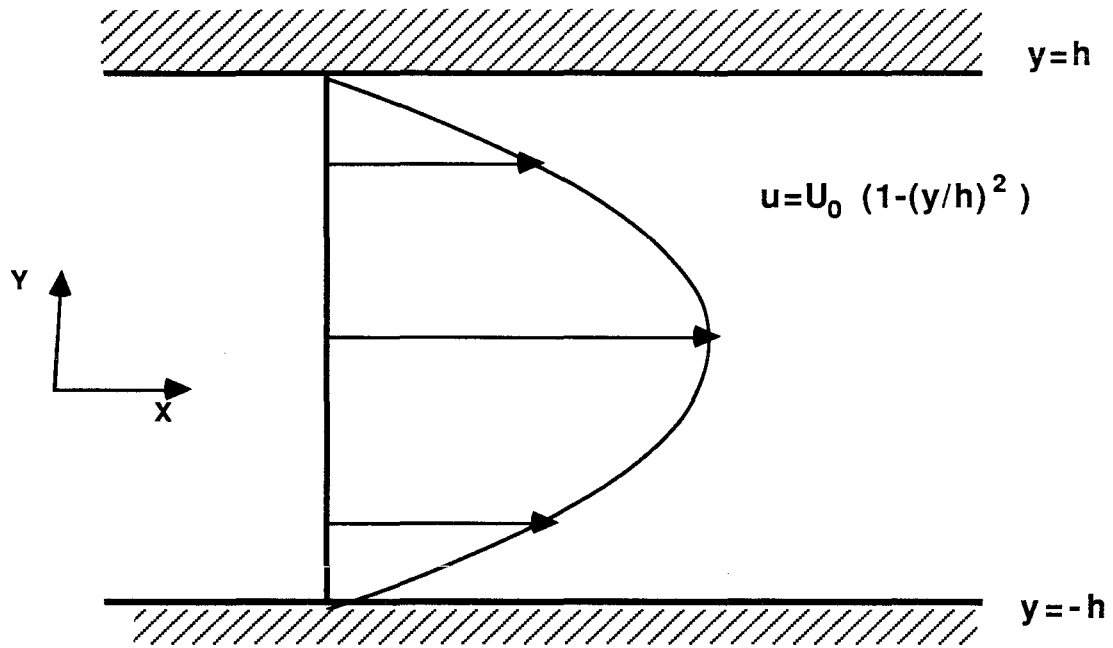
Figure 2.1. Geometry of plane Poiseuille flow.

$$u = U_0 \left(1 - (y/h)^2\right)$$
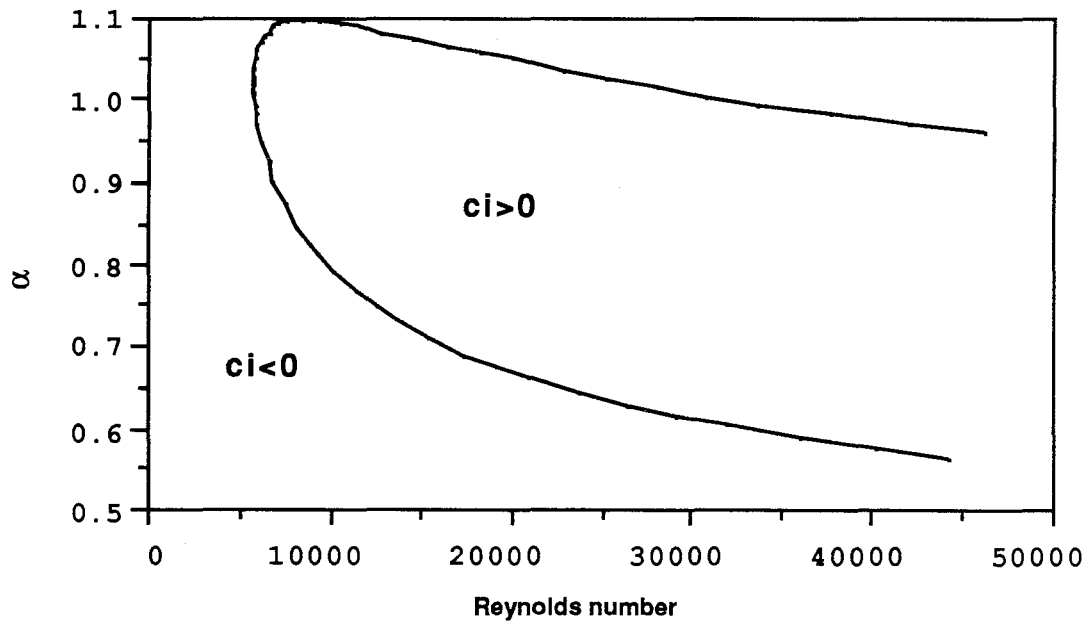
Figure 2.2. Orr-Sommerfeld curve.

where the subscripts denote differentiation. For flow down a channel, see Figure 2.1, an exact solution to (2.4) is $\Psi = U_0(y - \frac{y^3}{3h^2})$. This solution satisfies the no slip boundary conditions,

$$u = \frac{\partial \Psi}{\partial y} = 0 \qquad y = \pm h$$
$$v = -\frac{\partial \Psi}{\partial x} = 0 \qquad y = \pm h, \tag{2.5}$$

and has a parabolic velocity profile. We call this the basic solution and let $\Psi_b \equiv U_0(y - \frac{y^3}{3h^2})$. To find bifurcations to 2D travelling waves, we study the stability of Ψ_b to infinitesimal disturbances. Thus let

$$\Psi = \Psi_b + \epsilon \phi(y) e^{i\alpha(x-ct)} \tag{2.6}$$

where α is the wave number and $c = c_r + ic_i$ is the complex phase speed of the disturbance. Substituting (2.6) into (2.4)–(2.5) and nondimensionalizing by the channel half width h and the characteristic velocity U_0, (2.4)–(2.5) become

$$\frac{1}{i\alpha Re}(D^2 - \alpha^2)^2 \phi = (U - c)(D^2 - \alpha^2)\phi - U''\phi = 0 \tag{2.7}$$

$$\alpha\phi = D\phi = 0 \qquad y = \pm 1, \tag{2.8}$$

where $Re = \frac{U_0 h}{\nu}$ is the Reynolds number, $D = \frac{d}{dy}$ and $U = 1 - y^2$ is the dimensionless basic velocity. Equation (2.7) is known as the Orr-Sommerfeld equation. For a given wave number and Reynolds number, equations (2.7) and (2.8) constitute an eigenvalue problem for the eigenvalue c and the eigenfunction $\phi(y)$.

Only one eigenfunction of (2.7) is known to have an eigenvalue $c(\alpha, Re)$ whose imaginary part becomes greater than zero in a region of the α–Re plane (Drazin and Reid, 1981). The curve of marginal stability for this eigenvalue, $c_i = 0$, is shown in Figure 2.2. If one holds the wave number fixed and increases the Reynolds number in order to pass through the marginal stability curve, the eigenvalue and

its complex conjugate cross the imaginary axis transversely. Therefore, the curve

of marginal stability also represents a curve of Hopf bifurcation points.

2.3 Numerical Method for Detection of Bifurcation Points

To solve this problem numerically, we impose two additional equations to specify the phase and amplitude of the disturbance. One convenient way is to set

$$\Re(\phi''(y = -1)) = c1$$

$$\Im(\phi''(y = -1)) = c2, \tag{2.9}$$

where $c1$ and $c2$ are constants.

We applied the software package AUTO developed by Doedel and Kernevez (1985) to solve (2.7)-(2.9). This software considers first order systems of the form

$$u'(y) = f(u(y), \lambda), \qquad y \in [0, 1], \quad u(\cdot), f(\cdot, \cdot) \in \mathbf{R}^n, \quad \lambda \in \mathbf{R}^{n_\lambda}, \tag{2.10}$$

subject to the general boundary conditions

$$b_i(u(0), u(1), \lambda) = 0, \qquad i = 1, 2, \cdots n_b, \tag{2.11}$$

and general integral constraints

$$\int_0^1 q_i(u(y), \lambda) dy = 0, \qquad i = 1, 2, \cdots, n_q. \tag{2.12}$$

In order for the problem to be well posed, we require that $n_\lambda = n_b + n_q - n + 1$. This implies that there will be one free parameter and we can usually calculate solution curves to (2.10). The software approximates the differential equation, boundary conditions and integral constraints by the method of collocation at m Gauss points with piecewise Lagrange polynomials that belong to the class $C[0, 1]$. Specifically, we define a mesh

$$\{y = y_0 < y_1 < \cdots < y_N = 1\}, \qquad \Delta y_j = y_{j+1} - y_j, \quad (0 \le j \le N - 1),$$

and for each j, we introduce the Lagrange basis polynomials

$$\{w_{j,i}(y)\}, \quad j = 0, 1, \cdots, N-1, \qquad i = 0, 1, \cdots, m,$$

defined by

$$w_{j,i}(y) = \prod_{k=0, k\neq i}^{m} \frac{y - y_{j+\frac{k}{m}}}{y_{j+\frac{i}{m}} - y_{j+\frac{k}{m}}}, \qquad y_{j+\frac{i}{m}} \equiv y_j + \frac{i}{m}\Delta y_j.$$

Note that we transform the geometry of our problem so that $y \in [0, 1]$. The collocation method now consists of finding

$$p_j(y) = \sum_{i=0}^{m} w_{j,i}(y)u_{j+\frac{i}{m}},$$

such that

$$p'_j(z_{j,i}) = f(p_j(z_{j,i}, \lambda), \qquad i = 1, \cdots, m \quad j = 0, 1, \cdots, N-1, \qquad (2.13)$$

where in each subinterval $[y_{j-1}, y_j]$ the points $\{z_{j,i}\}_{i=1}^{m}$ are the zeroes of the mth degree Legendre polynomial relative to that subinterval. With the above choice of basis, u_j and $u_{j+\frac{i}{m}}$ are to approximate the continuous problem at y_j and $y_{j+\frac{i}{m}}$ respectively.

In a similar manner, AUTO discretizes the integral conditions by a quadrature formula over each subinterval:

$$\sum_{j=0}^{N-1} \sum_{i=0}^{m} w_{j,i}q_k(u_{j+\frac{i}{m}}, \lambda) = 0, \qquad k = 1, \cdots, n_q. \qquad (2.14)$$

The discrete boundary conditions are

$$b_i(u_0, u_N, \lambda) = 0, \quad i = 1, \cdots, n_b. \qquad (2.15)$$

To compute solution branches, AUTO uses pseudo-arclength continuation and adjoins the equation

$$\int_0^1 (u(y) - u_0(y))^* \dot{u}_0(t)dt + (\lambda - \lambda_0)^* \dot{\lambda} - \Delta s = 0,$$

where (u_0, λ_0) is the previously computed point on the solution branch and $(\dot{u}_0, \dot{\lambda}_0)$ is the normalized tangent vector at that point. The discretized version of this equation is

$$\sum_{j=0}^{N-1} \sum_{i=0}^{m} w_{j,i}(u_{j+\frac{i}{m}} - (u_0)_{j+\frac{i}{m}})^*(\dot{u}_0)_{j+\frac{i}{m}} + (\lambda - \lambda_0)^*\dot{\lambda} - \Delta s = 0. \qquad (2.16)$$

Equations (2.13)–(2.16) form a system of $mnN+n_b+n_q+1$ nonlinear equations. Newton iteration is used to solve this system along the solution branch.

We used four collocation points and up to 50 mesh points to accurately resolve the boundary layers formed at high Reynolds numbers. In addition, we adjusted the mesh after every step. AUTO uses an adaptive mesh scheme which minimizes the local discretization error.

To continue along the solution branch, we made use of AUTO's adaptive stepsize capabilities. If the Newton iteration converges rapidly then the stepsize is increased. If the Newton iterations converges slowly or fails to converge, then the stepsize is halved. If a preselected maximum stepsize is reached, then the stepsize will not exceed that value. If a preselected minimum stepsize is reached, then the program will signal nonconvergence.

We defined convergence to have occurred if the Newton increments satisfied

$$\frac{|\Delta\lambda|}{1+|\lambda|} < 10^{-6}, \quad \frac{\|\Delta u\|_\infty}{1+\|u\|_\infty} < 10^{-6}.$$

To compute the marginal curve, an initial guess must be provided for the eigenfunction, eigenvalue, and the other parameters. The eigenvalue spectrum for (2.4) has been derived for $Re \ll 1$ (Drazin and Reid, 1981). Using this spectrum as an initial guess, we continue the solution to the curve where $c_i = 0$. The curve is shown in Figure 2.2 and we found the minimum Reynolds number to be 5772.22.

This value compares well with the value computed by Orszag (1971) and Davey (1974).

In summary, we have calculated the curve of marginal stability which also represents a curve of Hopf bifurcations to 2D travelling waves.

2.4 Calculation of Two Dimensional Steady Waves

We look for steady 2D travelling waves in the streamwise direction with phase speed c. Letting $\Psi(x, y, t) = \Psi_b + \psi(\tilde{x}, y)$ where $\tilde{x} = x - ct$ and nondimensionalizing by the channel half width h and the centerline velocity U_0, (2.1) becomes

$$(U - c)\nabla^2 \Psi_x - \frac{1}{Re}\nabla^4 \Psi - U''\Psi_x + \Psi_y \nabla^2 \Psi_x - \Psi_x \nabla^2 \Psi_y = 0, \qquad (2.17)$$

where we write x for $\tilde{x}$.

Using a spectral decomposition, we let

$$\psi(x, y) = \sum_{n=-\infty}^{\infty} \hat{\psi}_n(y) e^{i\alpha n x} \qquad (2.18)$$

yielding the modal equations,

$$-\frac{1}{Re}\left(S_x^4 + 2S_x^2\frac{d^2}{dy^2} + \frac{d^4}{dy^4}\right)\hat{\psi}_n + (U - c)\left(S_x^2 + \frac{d^2}{dy^2}\right)S_x\hat{\psi}_n - U''S_x\hat{\psi}_n$$

$$+\hat{\psi}_y * \left(S_x^2 + \frac{d^2}{dy^2}\right)S_x\hat{\psi} - (S_x\hat{\psi}) * \left(S_x^2 + \frac{d^2}{dy^2}\right)\frac{d\hat{\psi}}{dy} = 0, \qquad (2.19)$$

where $S_x f_n = i\alpha n f_n$ and $f * g = \sum_{m=-\infty}^{\infty} f_{n-m} g_m$ is the convolution of the two Fourier series. The reality of $\psi(x, y)$ requires

$$\hat{\psi}_{-n}(y) = \hat{\psi}_n^*(y)$$

implying that only modes $n \geq 0$ need to be determined.

The modal no slip boundary conditions are

$$\frac{d\hat{\psi}_n}{dy} = 0 \qquad y = \pm 1 \qquad n \geq 0$$

$$i\alpha n \hat{\psi}_n = 0 \qquad y = \pm 1 \qquad n > 0. \tag{2.20}$$

For $n = 0$, the zero mode of v is identically zero and we must specify two additional boundary conditions. As ψ is arbitrary to within a constant, we let

$$\hat{\psi}_0(-1) = 0. \tag{2.21}$$

One boundary condition is still undetermined. This indeterminacy results from an arbitrariness in choosing the nondimensionalizing velocity U_0. One possible choice is to define U_0 such that there is no perturbation to the average flux. The average flux Q is

$$Q = \frac{\alpha}{2\pi} \int\limits_{0}^{\frac{2\pi}{\alpha}} \int\limits_{-h}^{+h} u \, dy \, dx, \tag{2.22}$$

where we are using the dimensional form for these variables. Letting $u = \frac{\partial \Psi}{\partial y}$ and $\Psi = \Psi_b + \psi(x, y)$, we obtain

$$Q = [\Psi_b + \hat{\psi}_0]_{-h}^{+h} \tag{2.23}$$

where the streamfunction is in dimensional form. To permit no perturbation to the average flux, we set

$$[\hat{\psi}_0]_{-h}^{+h} = 0. \tag{2.24}$$

Equations (2.15) and (2.12) yield the additional boundary condition

$$\hat{\psi}_0(h) = 0 \tag{2.25a}$$

or in dimensionless form

$$\hat{\psi}_0(1) = 0. \tag{2.25b}$$

Alternatively, one can define U_0 such that there is no perturbation to the average pressure gradient. The average pressure gradient P is

$$P = \frac{\nu}{2h} [\Psi_{b,yy} + \hat{\psi}_{0,yy}]_{-h}^{+h}, \tag{2.26}$$

where the above is in dimensional form. To allow no perturbation to the average pressure gradient, we set the additional boundary condition

$$[\hat{\psi}_{0,yy}]_{-h}^{+h} = 0 \qquad (2.27a)$$

or in dimensionless from

$$[\hat{\psi}_{0,yy}]_{-1}^{+1} = 0. \qquad (2.27b)$$

Equations (2.25) and (2.27) represent the two limits of zero average flux perturbation and zero average pressure gradient perturbation. In general, it is possible to take a linear combination of these flows and thus there is a continuous range of boundary conditions.

Corresponding to (2.25) and (2.27) are two different Reynolds number Re_Q and Re_P. Equation (2.24) implies

$$Q = \frac{4U_Q h}{3} \qquad (2.28)$$

and thus

$$Re_Q = \frac{hU_Q}{\nu} = \frac{3Q}{4\nu}. \qquad (2.29)$$

Alternatively, equation (2.27) implies

$$P = -\frac{2\nu U_P}{h^2} \qquad (2.30)$$

and thus

$$Re_P = \frac{hU_P}{\nu} = -\frac{h^3 P}{2\nu^2}. \qquad (2.31)$$

It is important to note that these Reynolds numbers represent different scalings of the problem and not different physics. In fact, using (2.29) and (2.31) one can show that

$$Re_P = Re_Q(1 - \frac{1}{4}[\hat{\psi}_{0Q,yy}]_{-1}^{+1}), \qquad (2.32)$$

where $\hat{\psi}_{0Q,yy}$ denotes that the second derivative was calculated with the constant flux boundary condition. For planar Poiseuille flow these two Reynolds numbers are equivalent. In general $Re_P = f(Re_Q, \alpha)$ and for 2D waves $Re_P > Re_Q$(Saffman, 1983).

An additional equation is required to eliminate the arbitrary phase shift in the x direction. If $\hat{\psi}_n$ is a solution for a given c, $\hat{\psi}_n e^{in\delta\alpha}$ is also a solution where δ is arbitrary. To eliminate this indeterminacy, we set

$$\frac{\Im(\psi_1''(y = -1))}{\Re(\psi_1''(y = -1))} = constant. \tag{2.33}$$

To continue the solution branch of the travelling wave solutions of (2.17) into the nonlinear regime, it is convenient to define a nonlinear amplitude. One possible choice is related to the disturbance energy:

$$A_E{}^2 = \frac{15}{16} \sum_{n=-N}^{N} {}' \int_{-1}^{+1} |u_n(y)|^2 + |v_n(y)|^2 \, dy, \tag{2.34}$$

where the prime indicates that the $n = 0$ mode is not included, and the $\frac{15}{16}$ factor is chosen so that the energy of the basic flow is normalized to one.

2.5 Numerical Method for 2D Waves

Truncating (2.19) at some number of modes, we are left to solve a finite system of nonlinear ODE's. We implement the discretization method described in section (2.1) and compute solution branches to the resulting nonlinear algebraic system by pseudo-arclength continuation. An initial guess is provided by the eigenfunction calculation described in section 2.3.

2.6 Results

Several authors have calculated the 2D waves discussed in this chapter. We have repeated the calculation to enable the study of 2D and 3D secondary bifurcations

to be discussed in the later chapters. As a check on our calculations, we show that our results are in good agreement with the earlier calculations.

In Figure 2.3, we plot amplitude versus Reynolds number for $\alpha = 1.02$. The zero amplitude point corresponds to the critical Reynolds number on the Orr-Sommerfeld curve. For each point on the Orr-Sommerfeld curve, there is a bifurcating nonlinear solution branch. These solution branches form a nonlinear neutral surface. In addition, solution branches exist for wave numbers larger than the maximum wave number on the Orr-Sommerfeld curve.

In Table 2.1, we compare our values for the critical Reynolds number of the nonlinear neutral surface , based on constant pressure, to Herbert's (1976) results for $N = 1$, $N = 2$ and $N = 3$ modes. As shown in the table, there are slight quantitative discrepancies between Herbert's (1976) results and our own. These discrepancies can be attributed to the more accurate procedure which was used in our calculation.

Herbert (1976) found the critical Reynolds number by determining the limit point in Reynolds number for each wave number. This is a very tedious procedure which can lead to errors since the critical wave number can be missed. We used a two parameter continuation of the limit point to determine the critical Reynolds number. Two parameter continuation of limit points is described in Keller (1988) and is implemented in AUTO. To check our results, we computed the critical Reynolds number at the critical wave number given by Herbert (1976) and confirmed his results.

In summary, we have calculated the marginal stability curve for plane Poiseuille flow. The points on this curve are bifurcation points to 2D travelling waves. We calculated the nonlinear neutral surface which is formed from the solution branches of these waves. The critical Reynolds number of this surface was found to be

approximately 2900 based on constant pressure gradient and 2600 based on constant flux. Although this reduces the critical Reynolds number from linear theory by a factor of 2 there is still a large discrepancy from the Reynolds number of ≈ 1000 found in experiment.

In the next chapter, we will study the 2D stability of the 2D waves. We will search for bifurcations to other 2D states which exist below the critical 2D wave Reynolds number.
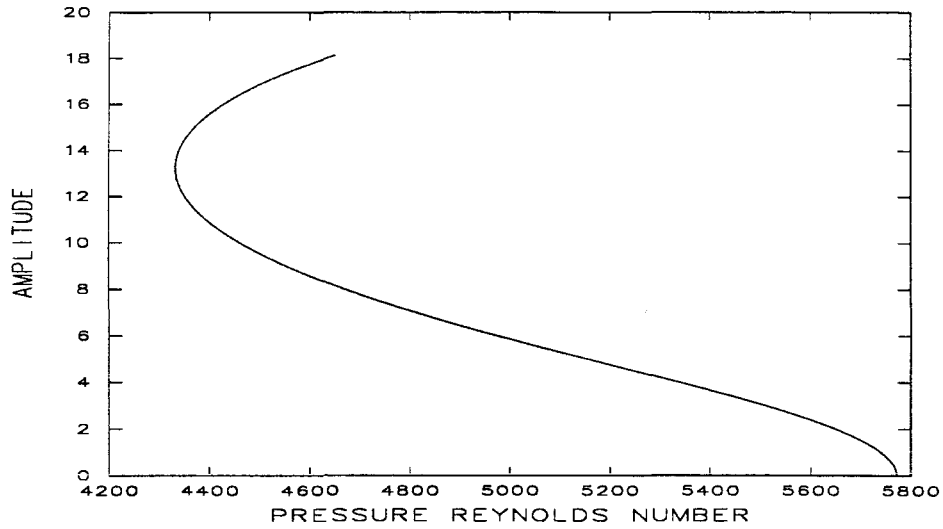
Figure 2.3. Cross-section of nonlinear neutral surface for $\alpha = 1.02$.

Table 2.1. Comparison of 2D waves results with Herbert (1976).

Parameters	Herbert (1976)			Present		
	N=1	N=2	N=3	N=1	N=2	N=3
α	1.2220	1.3130	1.3201	1.2222	1.3129	1.3179
Re_p	2825.56	2701.74	2911.6	2825.56	2701.72	2911.36
c	.3458	.3663	.3643	.3458	.3663	.3640

CHAPTER 3

2D STABILITY OF 2D WAVES

3.1 Introduction

In this chapter, we examine the 2D stability of the 2D waves found in plane Poiseuille flow. In particular, we are interested in the stability of these flows to perturbations of the same wavelength as the 2D wave.

In chapter one, we studied the 2D waves which bifurcate from plane Poiseuille flow. No 2D waves were found below a Reynolds number of 2600 (based on flux). This suggests that some other 2D or 3D steady state will be needed to explain the experimentally observed transition Reynolds number of approximately 1000. The search for such flows motivates the work in this chapter. We study the 2D stability of 2D waves in search of bifurcations to other 2D states which may exist below a Reynolds number of 2600.

An earlier 2D stability analysis by Pugh (1988) pointed out some interesting features. A typical cross-section of the 2D wave surface is shown in Figure 2.3. Orszag and Patera (1981) predicted that the lower branch of this surface is unstable to 2D disturbances with a stability transition occurring at the turning point. However, as Pugh showed numerically, in general this prediction is incorrect. In fact, although neutrally stable eigenmodes are present at the turning point, unstable eigenmodes may also be present. In addition, Pugh found bifurcations to quasi-periodic solutions on the upper branch. At these bifurcations, there is a change of stability.
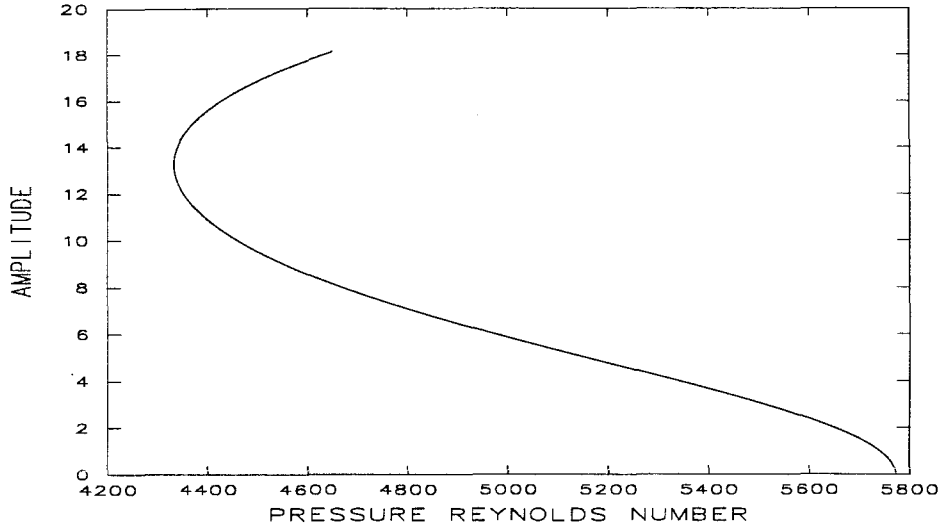
Figure 3.1. Typical cross-section of nonlinear netural surface.

We have improved on Pugh's results by a performing a more extensive numerical study. Several new bifurcations have been found, and some errors in Pugh's work are pointed out.

3.2 Problem Formulation

We wish to perturb the steady 2D flows discussed in the previous chapter. Thus, consider the dimensionless form of the streamfunction formulation in a moving frame of reference

$$\frac{\partial}{\partial t}(\nabla^2 \Psi) - \frac{1}{Re}\nabla^4 \Psi + (\Psi_y - c)\nabla^2 \Psi_x - \Psi_x \nabla^2 \Psi_y = 0 \qquad (3.1)$$

where c is the phase speed. We use Floquet theory to study the stability of the 2D waves. In a steady frame of reference the 2D states can be described by a

streamfunction

$$\Psi_{2D}(x,y) = \Psi_{2D}(x + \frac{2\pi}{\alpha}, y) \qquad (3.2)$$

where α is the wave number of the 2D wave.

Then linear perturbations exist of the form

$$\Psi(x,y,t) = \Psi_{2D}(x,y) + \epsilon e^{i(px+\sigma t)} \sum_{-\infty}^{+\infty} \zeta_n(y)e^{i\alpha n x} \qquad (3.3)$$

where σ and ζ_n are the eigenvalue and eigenfunction respectively and p specifies the wavelength of the the disturbance. We let $p = 0$, which corresponds to superharmonic disturbances, and

$$\Psi_{2D}(x,y) = \Psi_b + \psi(x,y) \qquad (3.4),$$

where Ψ_b is the streamfunction of the basic flow and $\psi(x,y)$ represents a 2D secondary flow. Substituting (3.4) into (3.3), equation (3.1) becomes

$$-\frac{1}{Re}(S_x^4\hat{\zeta}_n + 2S_x^2\hat{\zeta}_{n,yy} + \hat{\zeta}_{n,yyyy}) + S_x((U-c)(S_x^2\hat{\zeta}_n + \hat{\zeta}_{n,yy}) - U''\hat{\zeta}_n)$$
$$+ \hat{\psi}_y * (S_x(S_x^2\hat{\zeta} + \hat{\zeta}_{yy})) + \hat{\zeta}_y * (S_x(S_x^2\hat{\psi} + \hat{\psi}_{yy})) \qquad (3.5)$$
$$- (S_x\hat{\psi}) * (S_x^2\hat{\zeta}_y + \hat{\zeta}_{yyy}) - (S_x\hat{\zeta}) * (S_x^2\hat{\psi}_y + \hat{\psi}_{yyy}) = \sigma(S_x^2\hat{\zeta}_n + \hat{\zeta}_{n,yy})$$

where U is the dimensionless basic velocity and we have used the spectral representation for $\psi(x,y)$. Applying the no slip boundary conditions at the walls we have in modal form

$$n \neq 0 \qquad \zeta_n'(\pm 1) = 0 \qquad (u_n(\pm 1) = 0)$$

$$\zeta_n(\pm 1) = 0 \qquad (v_n(\pm 1) = 0)$$

$$n = 0 \qquad \zeta_0'(\pm 1) = 0 \qquad (u_0(\pm 1) = 0). \qquad (3.6)$$

For $n = 0$, $v_0 = 0$ is identically satisfied and two additional boundary conditions must be given. As the streamfunction is arbitrary to within a constant, we let

$$\hat{\zeta}_0(-1) = 0. \qquad (3.7).$$

The final boundary condition is determined by fixing the parametrization of the problem. Two possible choices are

$$\hat{\zeta}_0(+1) - \hat{\zeta}_0(-1) = 0 \qquad \text{constant flux} \qquad (3.8)$$

or

$$\sigma(\hat{\zeta}_0(+1) - \hat{\zeta}_0(-1)) = \frac{1}{Re}(\hat{\zeta}_{0,yy}(+1) - \hat{\zeta}_{0,yy}(-1)) \qquad \text{constant pressure.} \quad (3.9)$$

Note that we will denote the constant average flux and constant average pressure gradient disturbances by constant flux and constant pressure respectively.

To derive (3.9), consider the dimensionless momentum equation in the x direction:

$$\frac{\partial u}{\partial t} + u\frac{\partial u}{\partial x} + v\frac{\partial u}{\partial y} = -\frac{\partial p}{\partial x} + \frac{1}{Re}\nabla^2 u$$

. Using integration by parts and the continuity equation, the convective terms disappear upon averaging in the x direction and integrating over the channel width. The momentum equation, therefore, becomes

$$[\frac{\partial \psi_0}{\partial t}]_{-1}^{+1} = -2P + \frac{1}{Re}[\psi_{0,yy}]_{-1}^{+1},$$

where we have used the streamfunction, P is the average pressure gradient, and only the zero mode is present for the streamfunction since we are averaging over x. Substituting (3.3) for the streamfunction and specfiying no perturbation to the basic pressure gradient, we derive (3.9) and (2.27).

By failing to consider the time derivative in the Navier-Stokes equation, Pugh incorrectly stated the constant pressure boundary condition as

$$\hat{\zeta}_{0,yy}(+1) - \hat{\zeta}_{0,yy}(-1) = 0 \qquad (3.10).$$

As can be seen from (3.9), this omission should introduce errors for large Reynolds number, and in fact this will be shown numerically.

3.3 Numerical Method

We implemented the method of spectral collocation (Orszag and Gottlieb, 1983) to solve the system of ODE's and boundary conditions described by (3.5)–(3.9). We let

$$\hat{\zeta}_n(y) = \sum_{k=0}^{N} a_{nk} \tilde{T}_k(y) \tag{3.11}$$

where $\tilde{T}_k(y)$ is a modified Chebyshev polynomial. Chebyshev polynomials were used to accurately resolve the boundary layers. The polynomials are modified to satisfy the boundary conditions (3.6)–(3.8) identically. For constant average flux we set

$$\tilde{T}_k(y) = (1 - y^2)^2 T_k(y) \tag{3.12}$$

and for constant average pressure gradient

$$\tilde{T}_k(y) = \int_{-1}^{y} (1 - x^2) T_k(x) \, dx \tag{3.13}$$

where $T_k(y) = \cos k(\cos^{-1} y)$. Derivatives of $\hat{\zeta}_n(y)$ are computed by differentiating the Chebyshev modes.

Substituting (3.11) into (3.5) it remains to solve a system of algebraic equations for a_{nk} ($n = 0, \ldots, N, k = 0, \ldots, K$). With the modifications described by (3.12) and (3.13), the boundary conditions (3.6)–(3.8) are identically satisfied, and only (3.9) must be imposed on the system of equations. Orszag and Gottlieb have shown that the maximum error can be minimized by evaluating at the maxima of the Kth Chebyshev polynomial. Evaluating at these maxima ($\theta_j = j\pi/K, y_j = \cos \theta_j, j = 0, \ldots, K$) and truncating (3.5) at a finite number of modes, we only need to solve a discrete generalized eigenvalue problem of the form

$$G\tilde{a} = \sigma B\tilde{a} \tag{3.14}$$

for the complex eigenvalue σ and complex eigenvector $\tilde{a}$.

Because large errors were incurred when using standard generalized eigenvalue solvers, we inverted the matrix B and solved the regular eigenvalue problem

$$C\tilde{a} = \sigma\tilde{a} \qquad \text{where} \qquad C = B^{-1}G. \tag{3.15}$$

The matrix C is complex if one uses the exponential form of the Fourier series shown in (3.3). Because the secondary flow is real, a real formulation for the matrix C can be derived by writing the Fourier series in trigonometric form. The real formulation effectively reduces the memory requirements of the computation by a factor of 4. Even for a low Fourier mode calculation, the real formulation reduces the memory requirements drastically. We should also note that the necessity for inverting the matrix B in (3.14) motivated the modification of the Chebyshev polynomials described by (3.12)–(3.13). The enforcement of the time independent boundary conditions (3.6)–(3.7) on (3.14) would introduce rows of zeroes in the matrix B and prevent its inversion.

3.4 Numerical Results

Calculations were performed for both constant flux and constant pressure disturbances. All of the calculations to be discussed were for $\alpha = 1.1$. Let us first consider constant flux disturbances. In Figure 3.2, we plot the maximum growth rate as a function of Reynolds number for $N = 1$ Fourier mode and $K = 70$ Chebyshev modes. The most unstable eigenvalue is always real in the range of Reynolds number shown. The lower branch is unstable with a stability transition occurring at the nose.

At the nose, there are two neutrally stable eigenvalues. As Pugh has shown, one eigenvalue is always zero on the 2D wave branch. This eigenvalue corresponds to the trivial phase shift solution of our system. In addition, there is a

ble eigenvalue at the nose with geometric multiplicity one and algebraic multiplicity two. Although a stability transition occurs at the nose, the upper branch does not remain stable. As shown in Figure 3.3, a complex eigenvalue goes unstable at a Reynolds number of 6300. As the eigenvalue and its complex conjugate cross the imaginary axis transversely, the point of stability transition represents a secondary Hopf bifurcation. The periodic flows emanating from this bifurcation together with the underlying steady waves lead to quasi-periodic solutions. Jimenez (1988) detected this bifurcation and followed the quasi-periodic flows with a time dependent code. In the next chapter, we will compute these flows with a steady code.

In Figure (3.4) we plot the maximum growth rate as a function of Reynolds number for $N = 2$ Fourier modes and $K = 70$ Chebyshev modes. As in the one Fourier mode calculation, the lower branch is unstable with a stability transition occurring at the nose. However, as shown in Figures 3.5–3.6, we now find two Hopf bifurcations occurring on the upper branch. The first Hopf bifurcation occurs at a Reynolds number of 5600 with period 20.6. The second Hopf bifurcation occurs at a Reynolds number of 6125 and with period 18.6. It is interesting to note that because Jimenez used a time dependent code he did not detect that two Hopf bifurcations are present. As the upper branch is unstable after the first Hopf bifurcation, a time dependent code could not detect the second Hopf bifurcation. In Figures 3.7–3.9, we plot the appropriate graphs for the N=3 Fourier modes and K=70 Chebyshev modes calculation. Only a quantitative difference can be seen from the $N = 2$ calculation. We repeated these calculations for $N = 4$ Fourier modes and again no qualitative difference was seen.
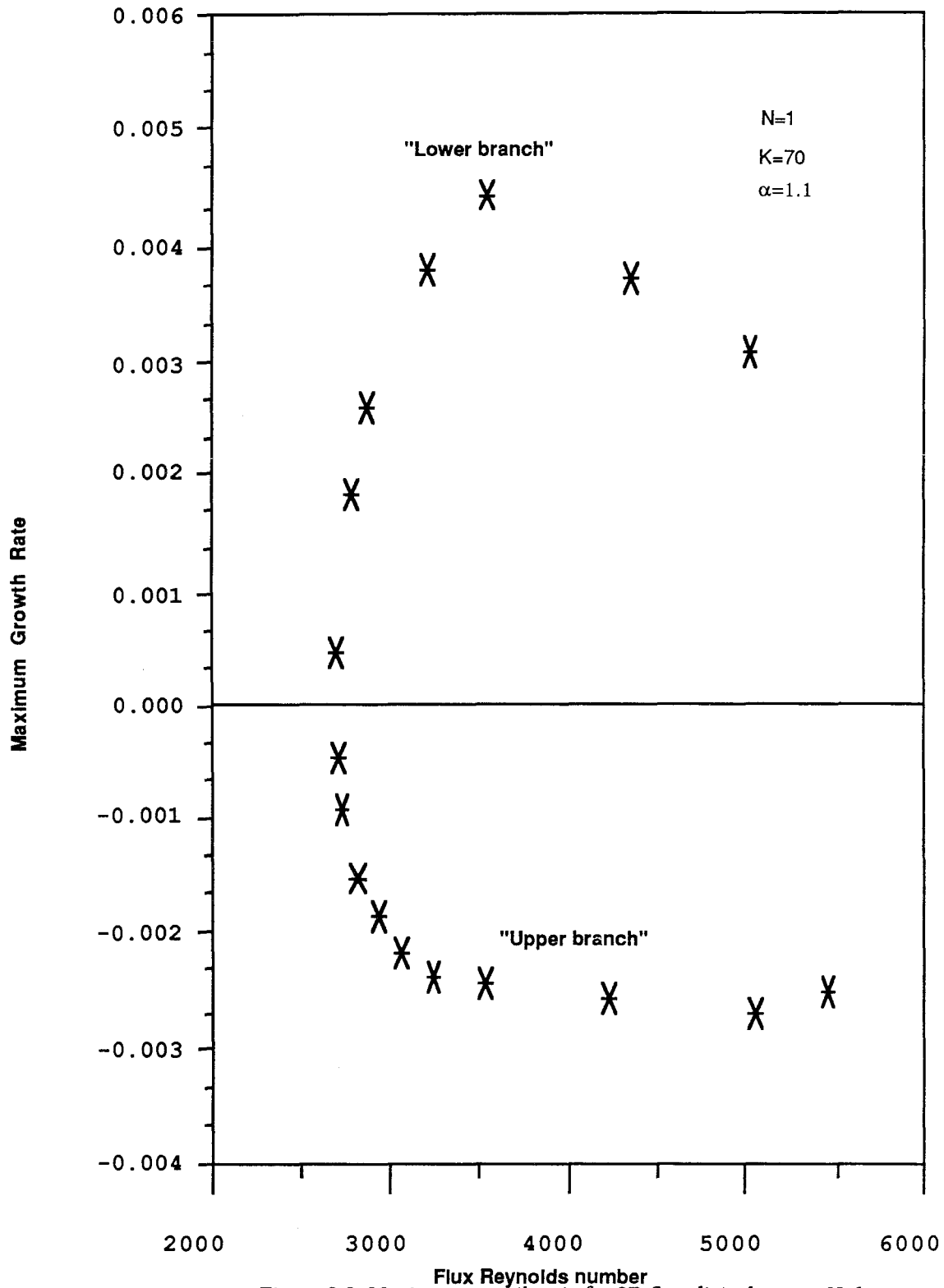
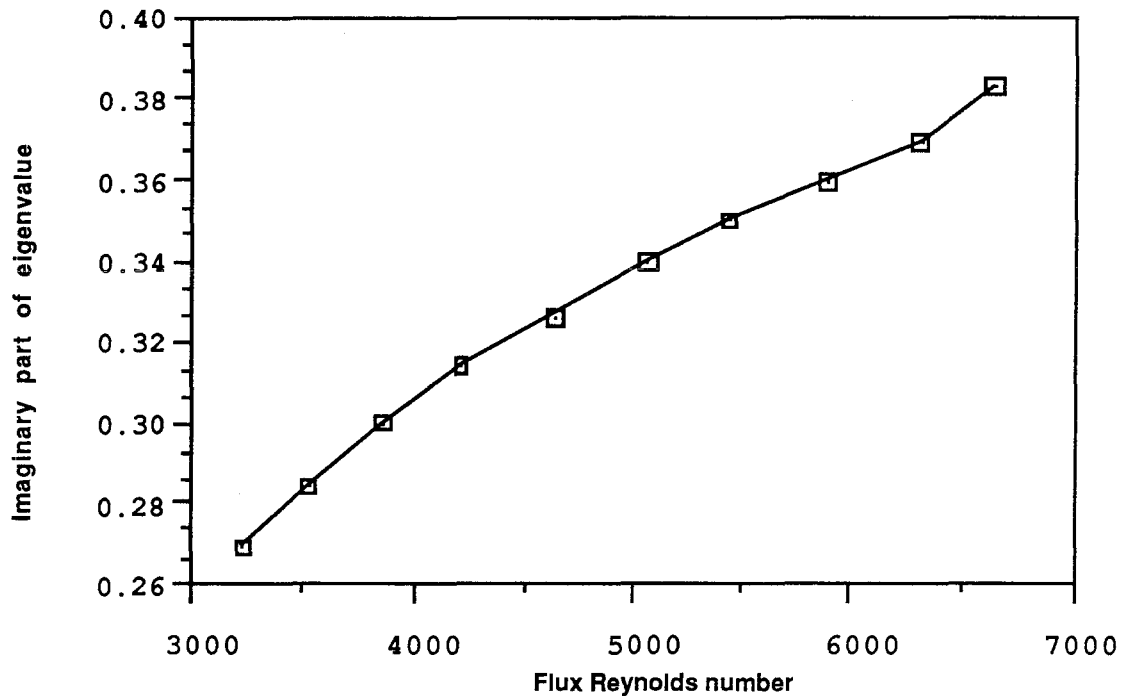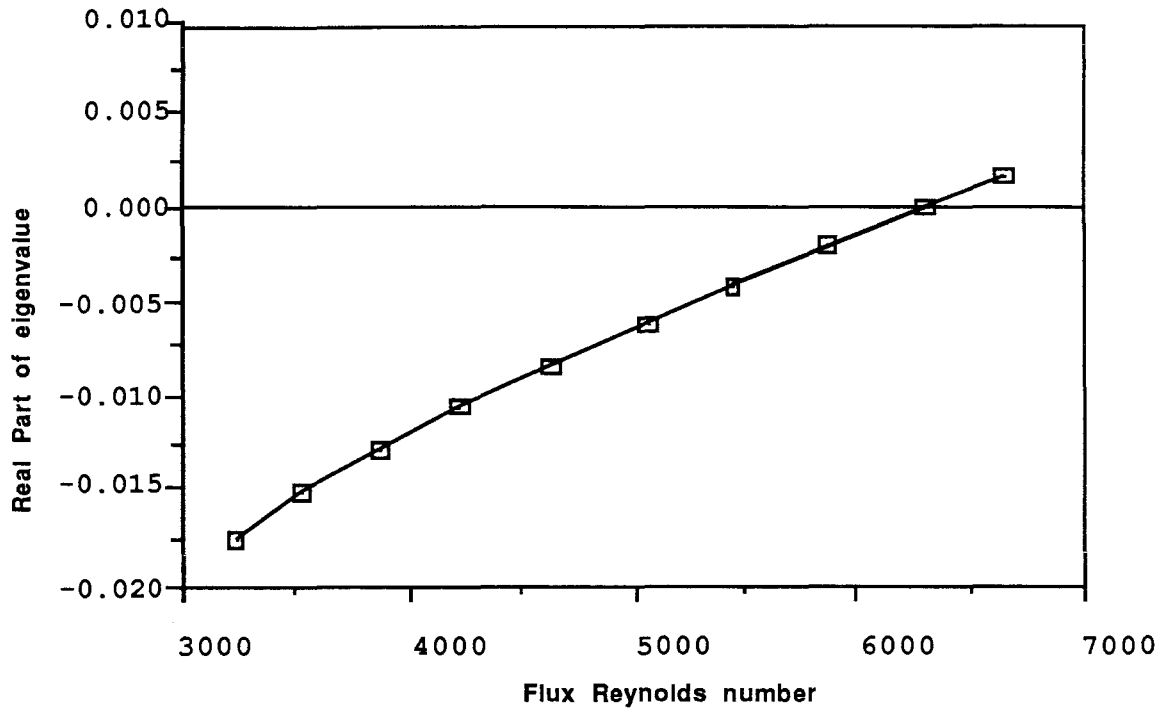Figure 3.2. Maximum growth rate for 2D flux disturbances, N=1.

Figure 3.3 Stability transition and Hopf bifurcation on upper branch.
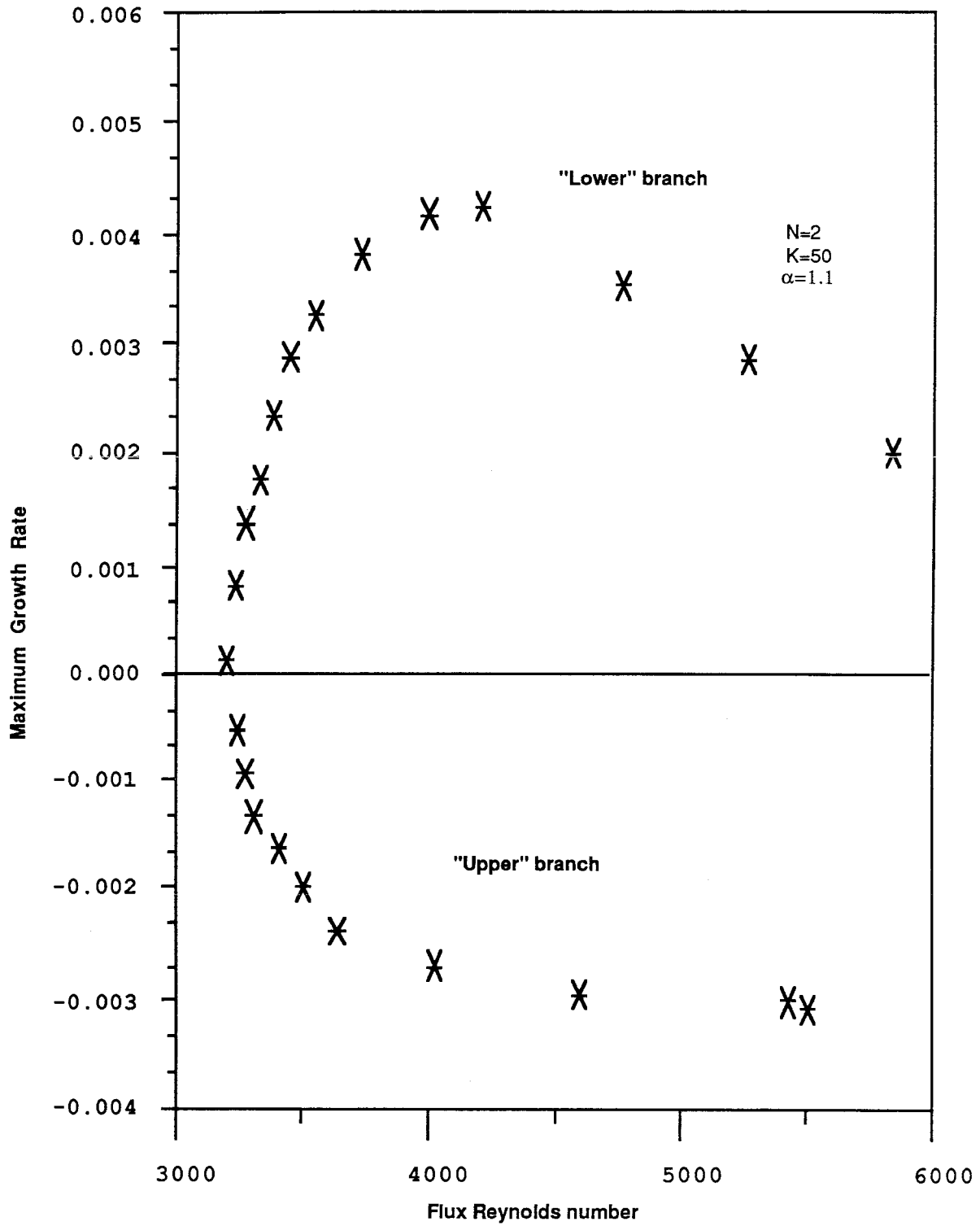
N=1, K=70, and wave number is 1.1.

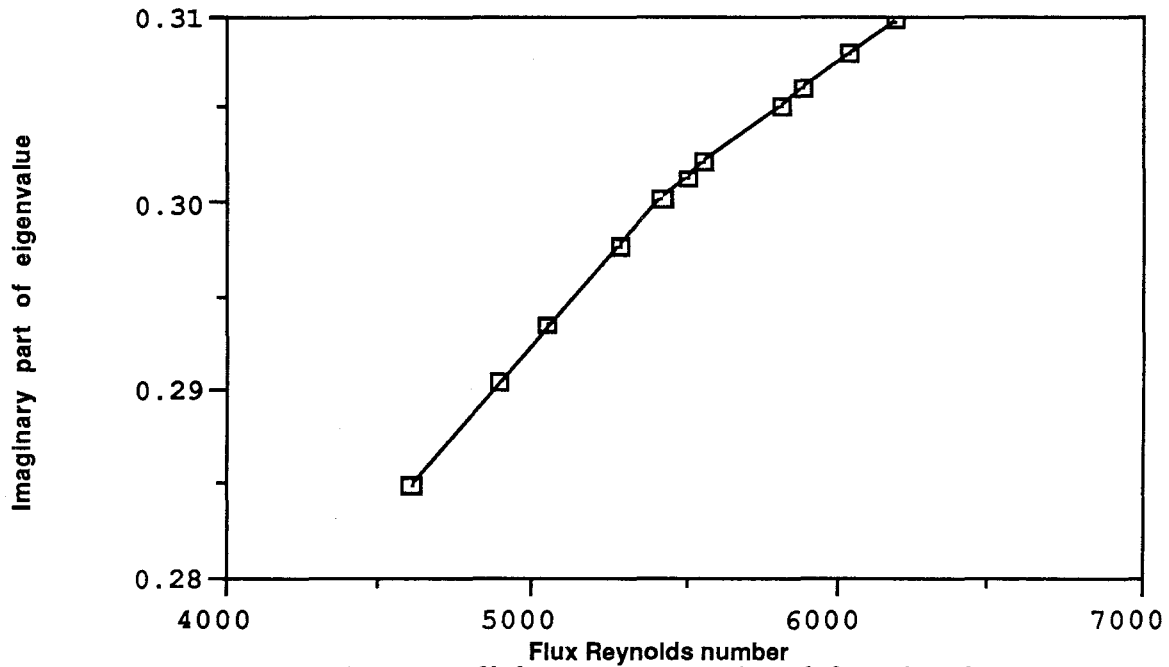Figure 3.4. Maximum growth rate for 2D flux disturbances, N=2.

Figure 3.5. First Hopf bifurcation on upper branch for Q disturbances, N=2.

N=2,K=70, and wave number is 1.1.

Figure 3.6. Second Hopf bifurcation on upper branch for Q disturbances, N=2.

N=2, K=70, and wave number is 1.1.

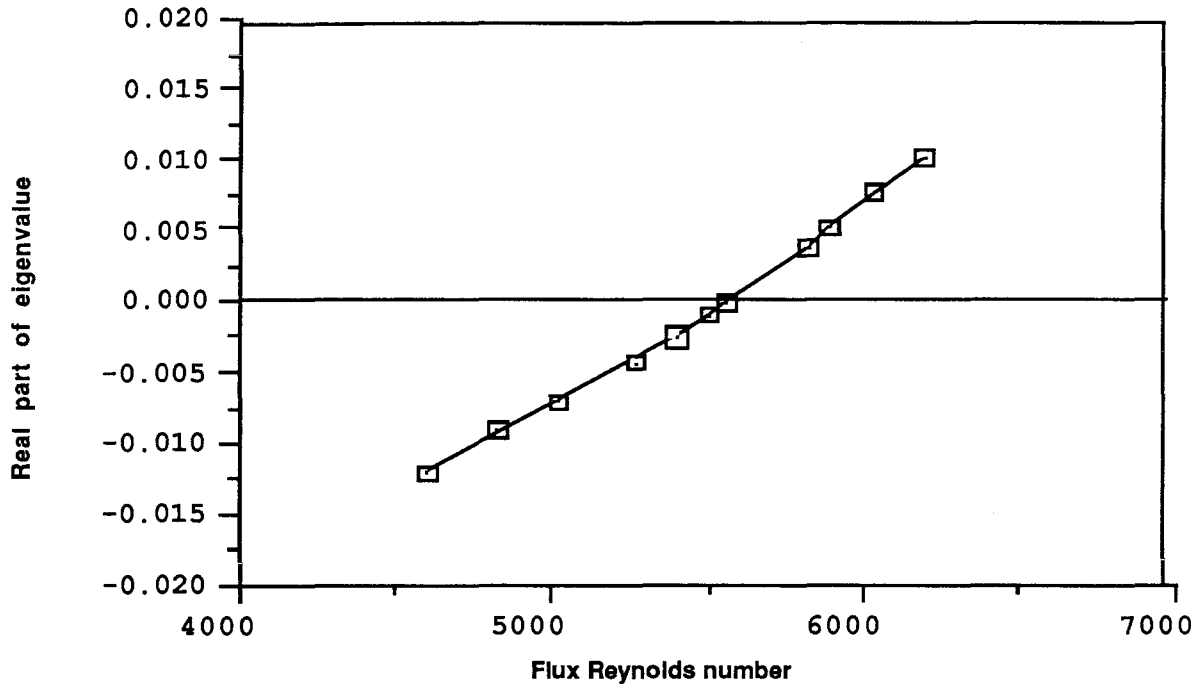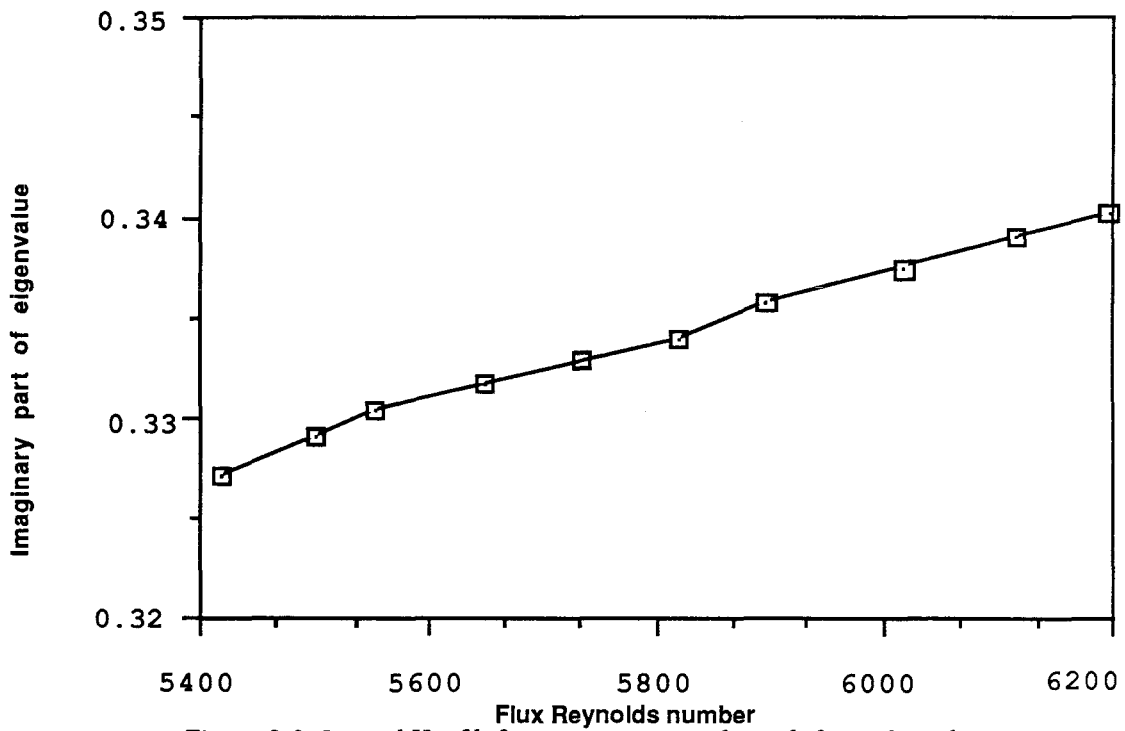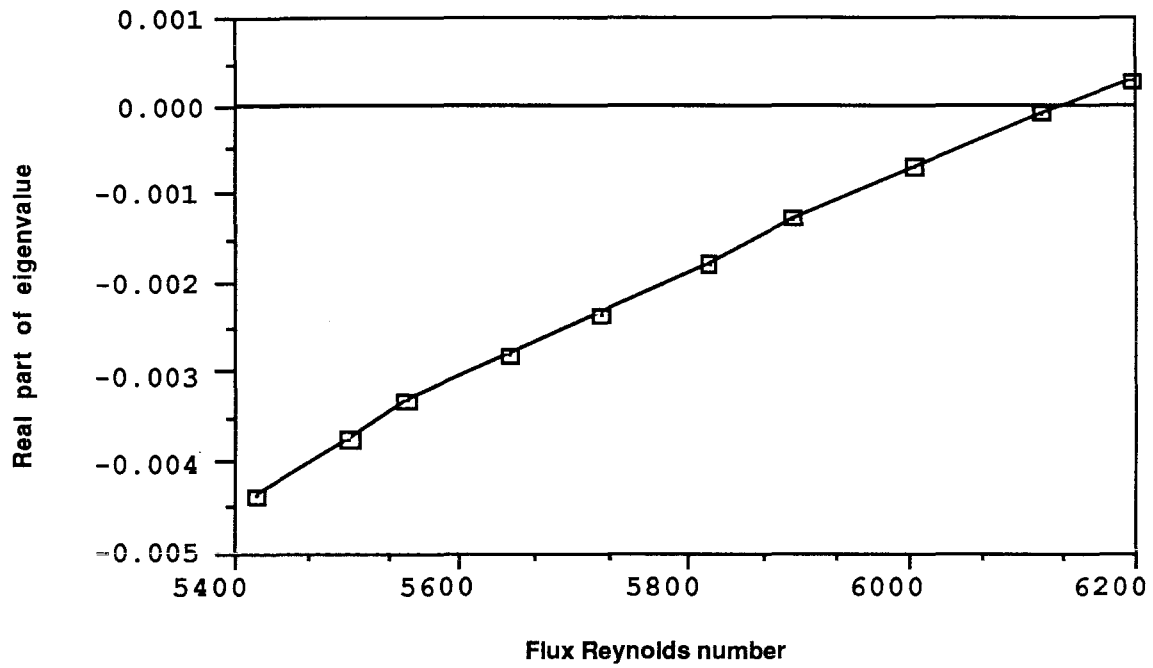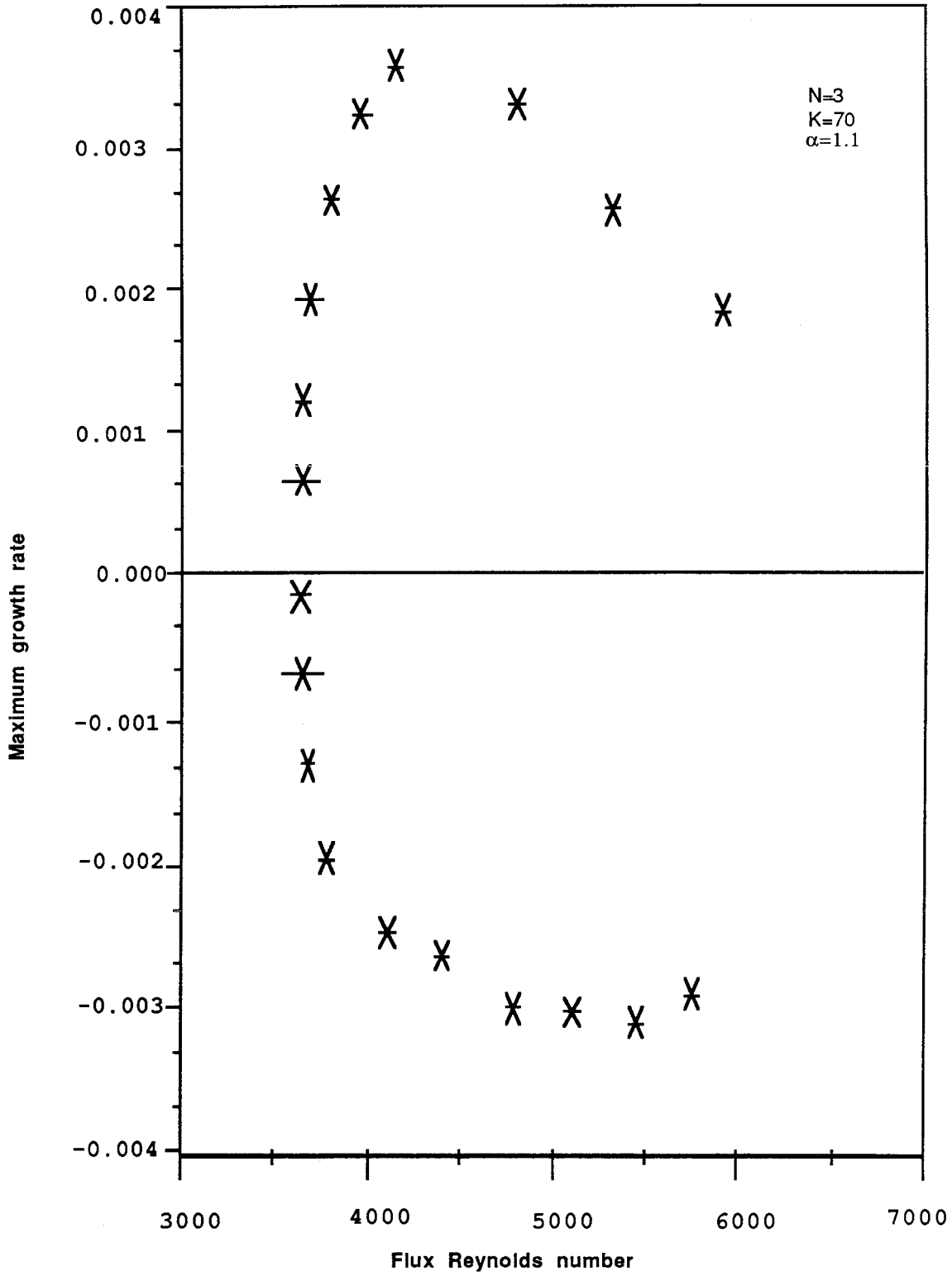Figure 3.7. Maximum growth rate for 2D flux disturbances, N=3.

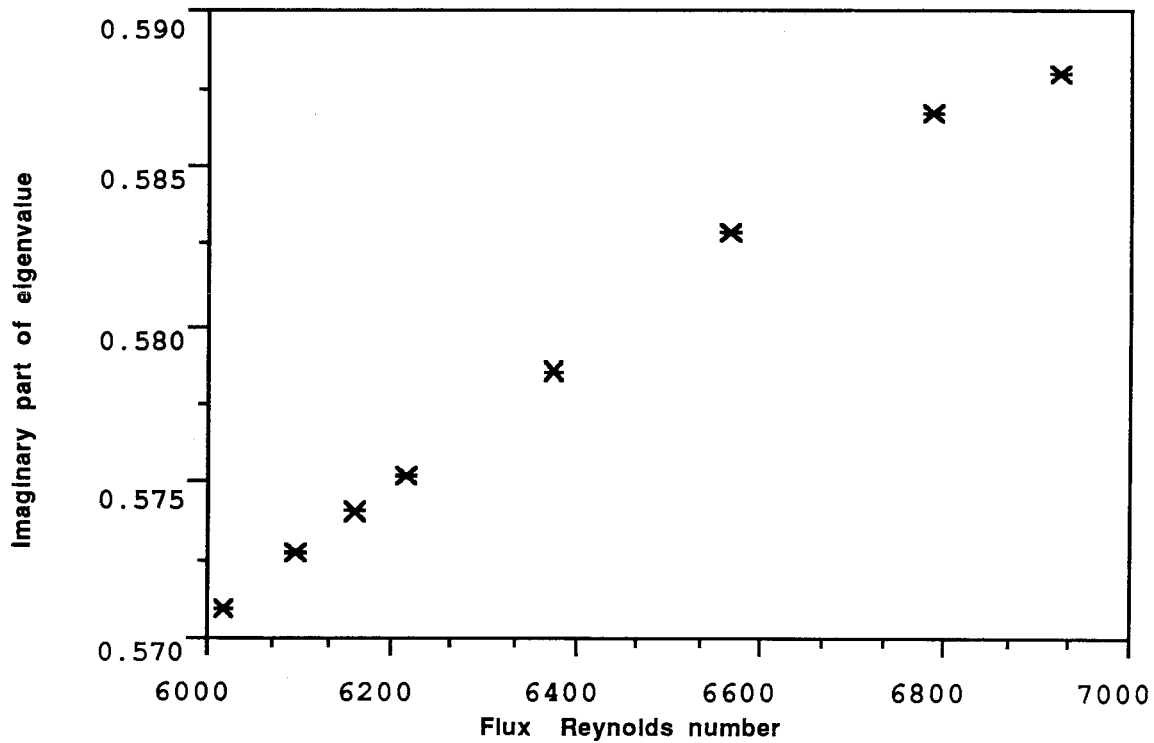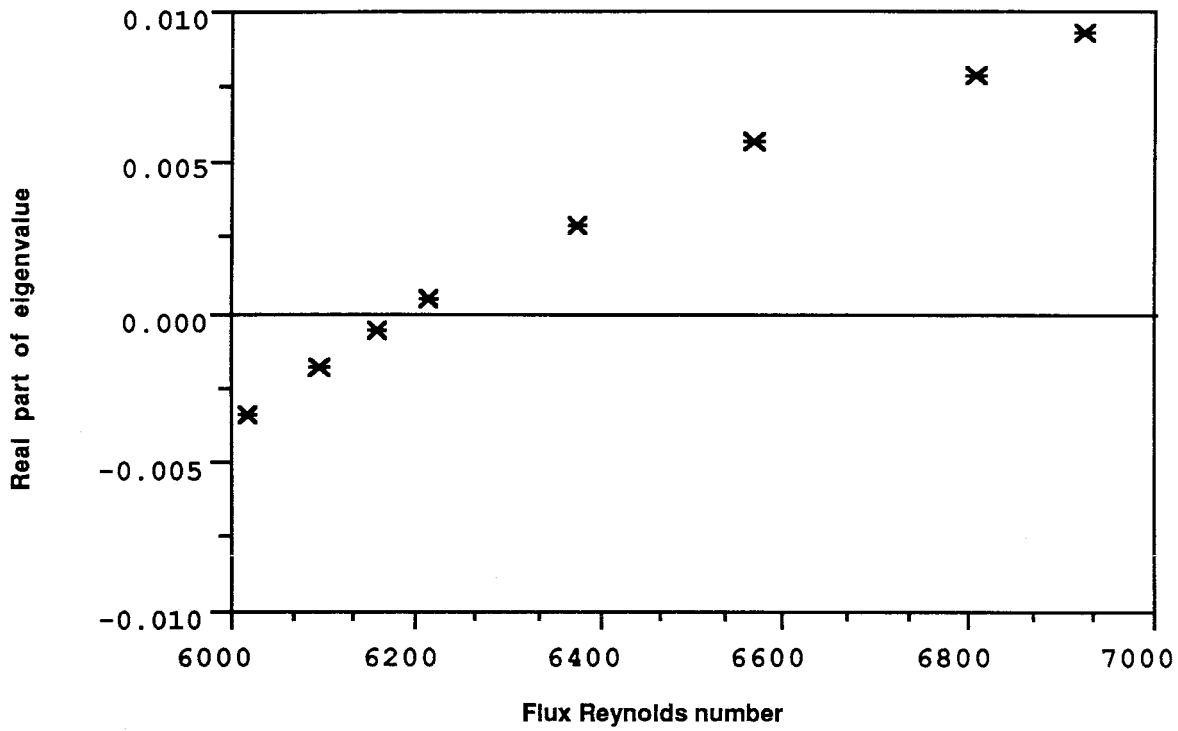Figure 3.8. First Hopf bifurcation on upper branch for Q disturbances, N=3.
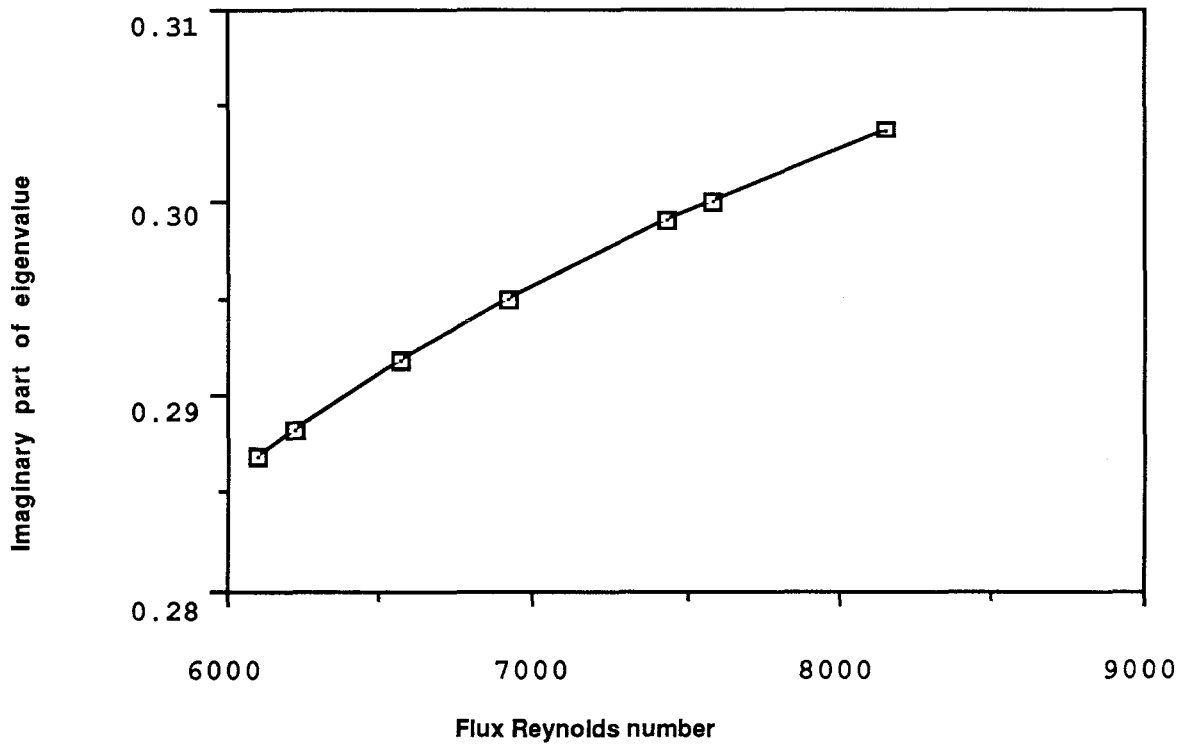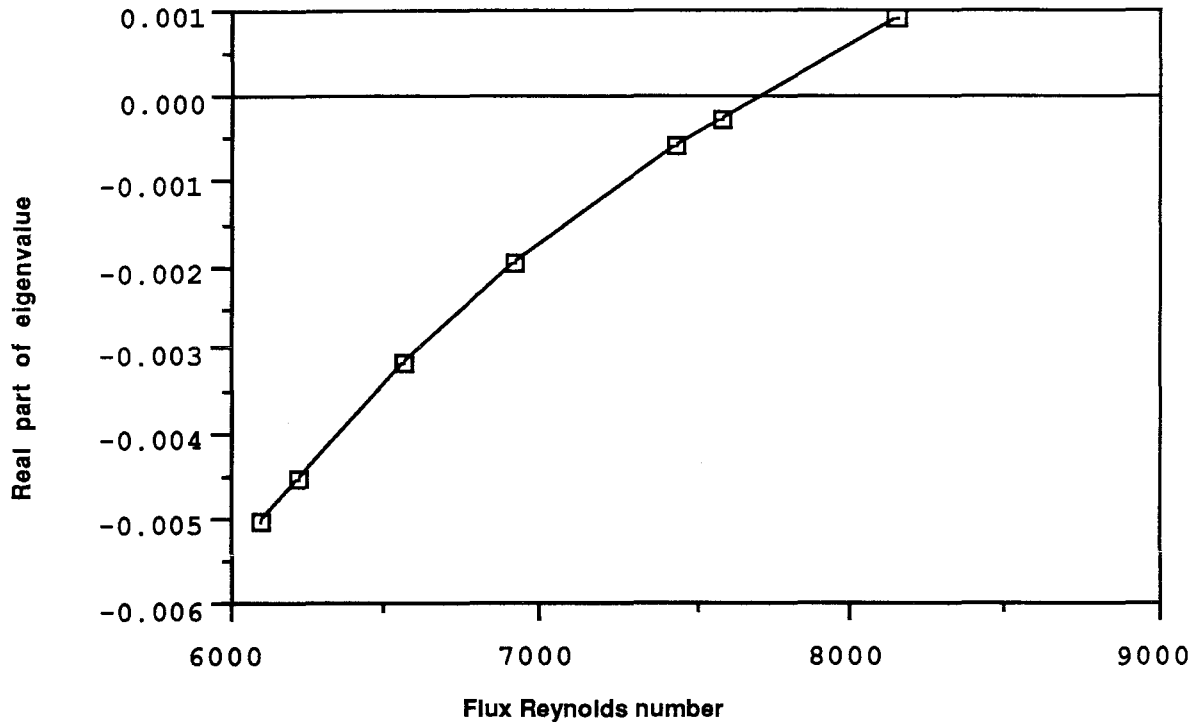
N=3,K=70 and wave number is 1.1.

Figure 3.9. Second Hopf bifurcation on upper branch for Q disturbances, N=3.
N=3,K=70 and wave number is 1.1.

In Tables 3.1–3.2, we show the period and Reynolds number of the two Hopf bifurcations for $N = 1$ to $N = 4$ modes. As can be seen from the Tables, we do not have quantitative convergence. Jimenez (1988) observed that the location of the first Hopf bifurcation did not settle down until $N = 7$. Although this resolution is not possible with our formulation, we do obtain qualitative convergence, i.e., the Hopf bifurcation does not disappear and the Reynolds number of the bifurcation lies between 5600 and 6300. We also obtain some of the quantitative features that Jimenez observed. In particular, the period of the first Hopf bifurcation is decreasing. Jimenez found that the period of the bifurcation decreased from ≈ 19.3 to ≈ 14.3 when increasing the resolution from $N = 1$ to $N = 7$ modes. For the second Hopf bifurcation, which Jimenez could not detect, there is less variation with increased resolution. In Chapter 4, we show that one can obtain qualitatively correct results, with low resolution, for the periodic orbits which emanate from these bifurcations. Specifically, we show that we obtain the correct behavior for the Reynolds number and period with increasing amplitude.

One sees a different stability picture for constant pressure disturbances. In Figure 3.10, we plot the maximum growth rate as a function of Reynolds number for $N = 1$ Fourier modes and $K = 70$ Chebyshev modes. As in the case of constant flux disturbances, the lower branch is unstable. A stability transition, however, does not occur at the nose. As shown in Figure 3.11, a different eigenvalue becomes neutrally stable at the nose and goes unstable on the upper branch. The two unstable eigenvalues merge on the upper branch and cross the imaginary axis transversely. Thus, we have detected a Hopf bifurcation not present for constant flux disturbances. In contrast to Pugh's results, we find that the upper branch does not remain stable. In Figure 3.12, we show that on the upper branch a complex eigenvalue goes unstable at a Reynolds number of 13500 with period 36. The point

of stability transition is a Hopf bifurcation and corresponds to the Hopf bifurcation detected in the N=1 calculation for constant flux disturbances. Pugh did not detect this bifurcation because he used the incorrect boundary condition (3.10) for constant pressure disturbances. As can be seen from (3.8) and (3.9), for large Reynolds number the constant flux and constant pressure boundary conditions are equivalent. In fact, at the Hopf bifurcation the constant pressure and constant flux Reynolds number are related by the scaling described in equation (2.32). The incorrect use of (3.10) also explains the quantitative difference between Pugh's results and our own. Pugh detected the first Hopf bifurcation, shown in Figure 3.11, at a Reynolds number of 3500 as compared to our value of 3136.

In Figures 3.13–3.15, we plot the results for the $N = 2$ Fourier modes and $K = 70$ Chebyshev modes calculation. The results are qualitatively similar to the $N = 1$ calculation except that we now detect three Hopf bifurcations on the upper branch. The first Hopf bifurcation corresponds to the stabilization of the unstable eigenvalues. The second Hopf bifurcation occurs at a Reynolds number of 9400 with period 35.5 and corresponds to the Hopf bifurcation detected in the N=1 calculation. The upper branch is unstable after this Hopf bifurcation. The third Hopf bifurcation is new and occurs at a Reynolds number of 13000 with period 34. This Hopf bifurcation represents another pair of eigenvalues destabilizing on the upper branch. The appearance of a new Hopf bifurcation with $N = 2$ Fourier modes corresponds to the results obtained for constant flux disturbances. This is to be expected as the constant flux and constant pressure boundary conditions are equivalent for large Reynolds number.

In Figure 3.16 we plot the maximum growth rate for the $N = 3$ Fourier modes and $K = 70$ Chebyshev modes calculation. Only a quantitative change is seen from the $N = 2$ calculation, and the three Hopf bifurcations persist. The calculations

were repeated for $N = 4$ Fourier modes and again only a quantitative change was seen.

In Tables 3.3–3.5, we show the period and Reynolds number for the three Hopf bifurcations on the upper branch. As in the case of constant flux disturbances, we do not obtain quantitative convergence for the second Hopf bifurcation. Jimenez did not do any calculations for constant pressure disturbances. The results, however, do correspond to the results observed for constant flux disturbances.

Table 3.1. Reynolds number and period of first Hopf bifurcation for constant flux disturbances.

Parameter	N=1	N=2	N=3	N=4
Re	6300	5600	6250	5875
T	17.5	20.6	12.5	13.4

Table 3.2. Reynolds number and period of second Hopf bifurcation for constant flux disturbances.

Parameter	N=1	N=2	N=3	N=4
Re		6125	7750	7500
T		18.6	20.73	19.75
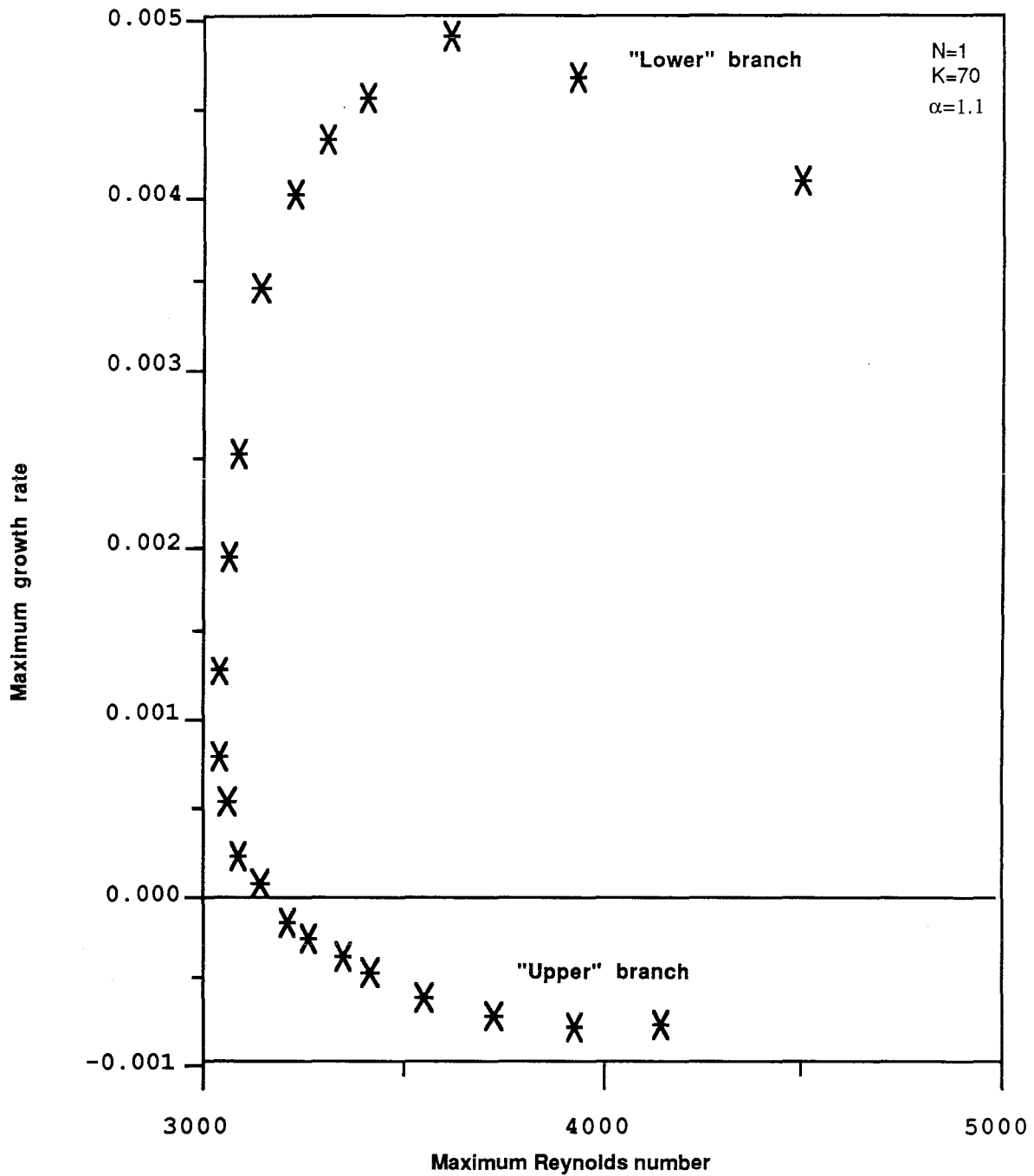
Figure 3.10. Maximum growth rate of 2D pressure disturbances, N=1.
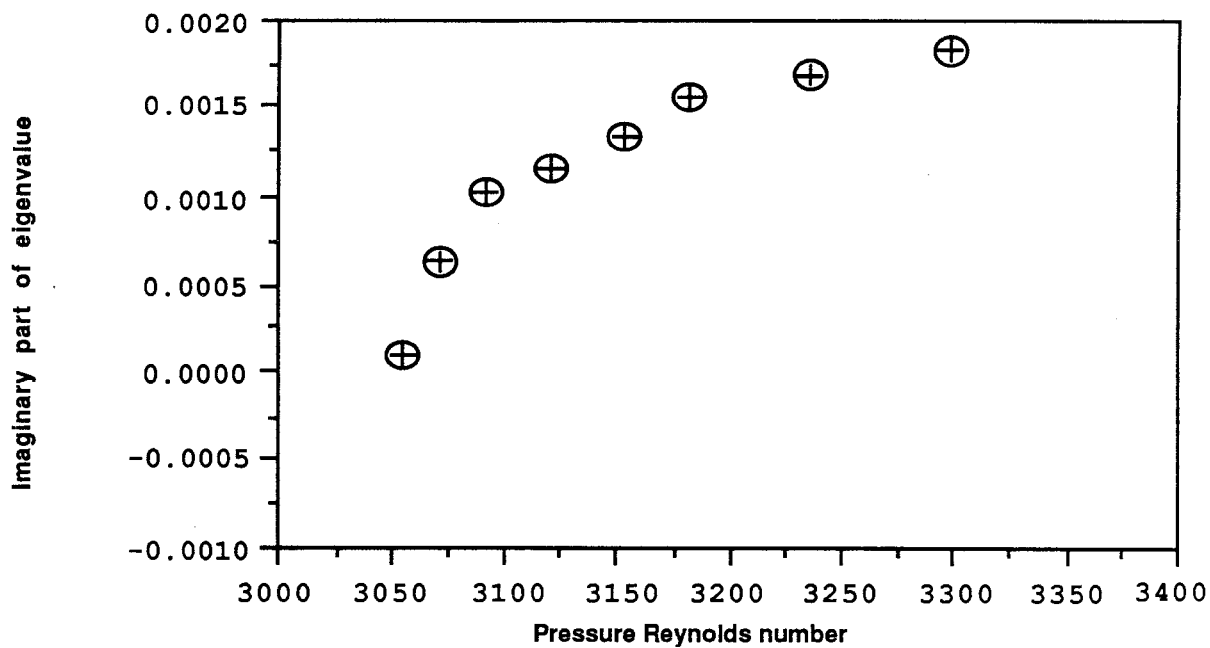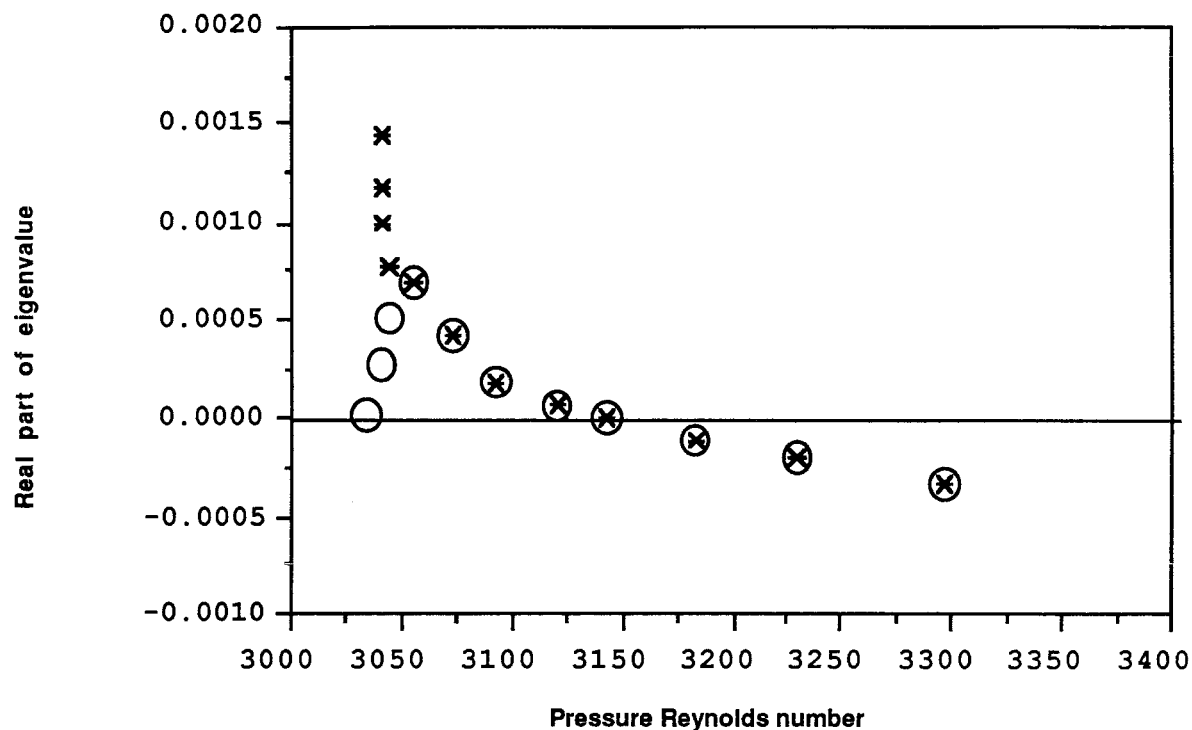
Figure 3.11. Merger of eigenvalues and subsequent Hopf Bifurcation
N=1,K=70 and wave number is 1.1.

Figure 3.12. Second Hopf bifurcation for P disturbances, N=1.

N=1,K=70 and wave number is 1.1.
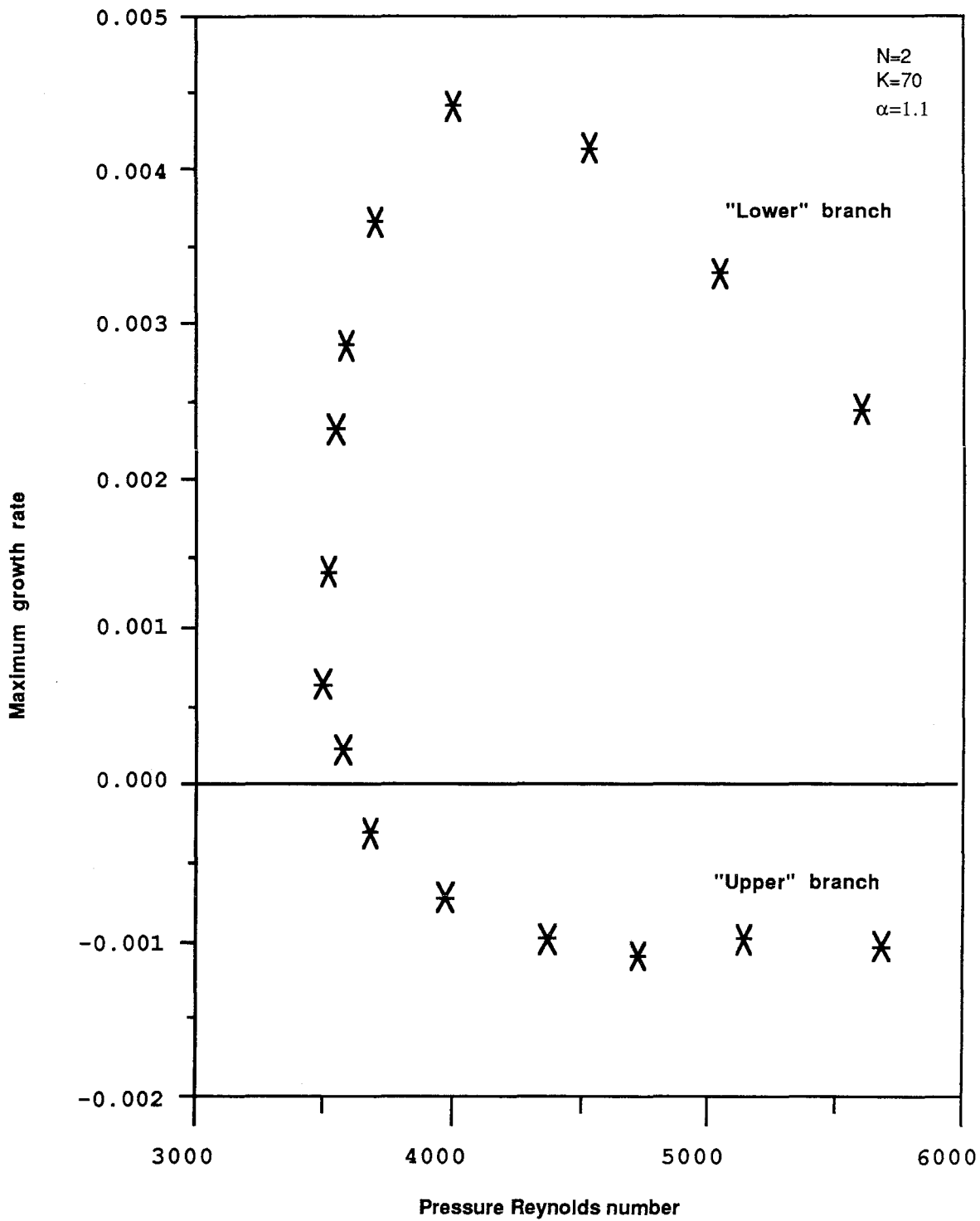
Figure 3.13. Maximum growth rate of of 2D pressure disturbances, N=2.
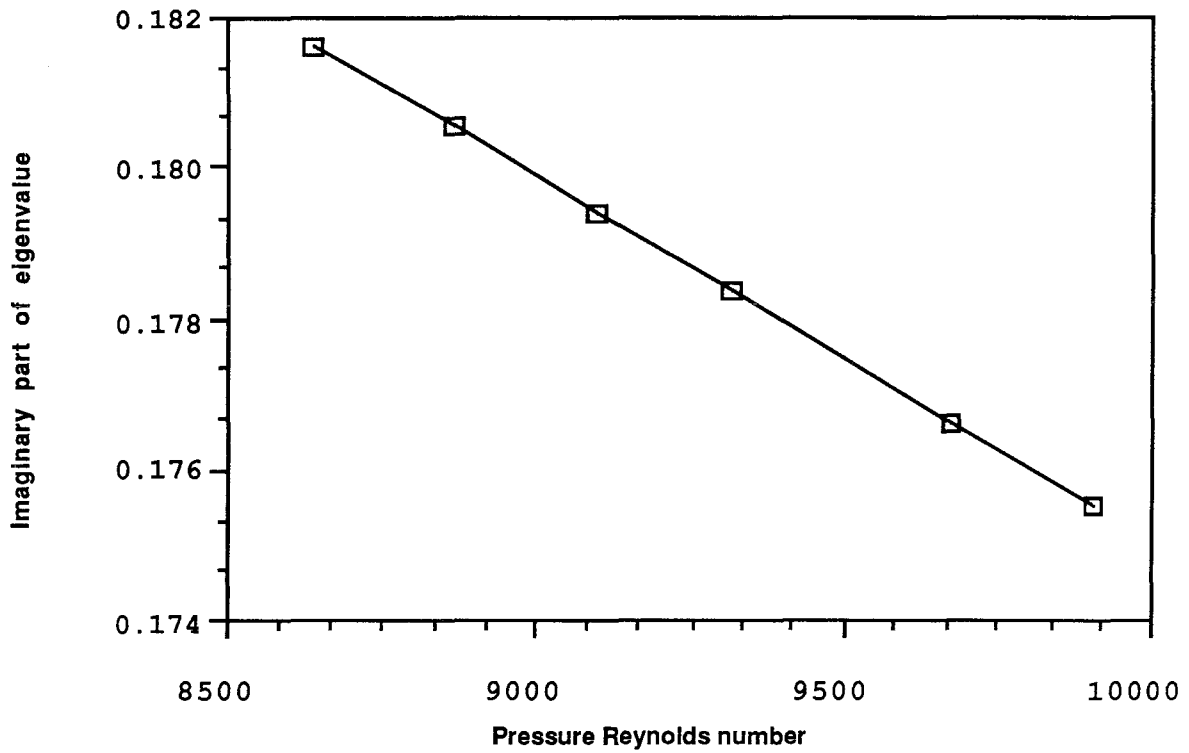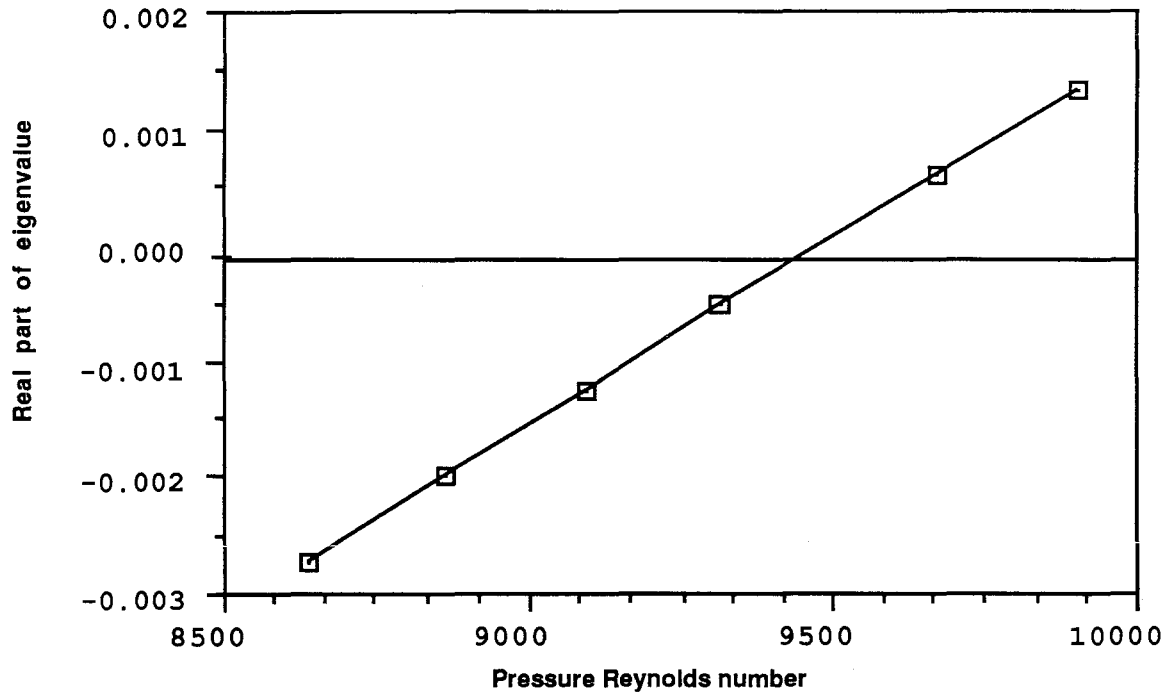
Figure 3.14. Second Hopf bifurcation for P disturbances, N=2.
N=2, K=70, and wave number is 1.1.
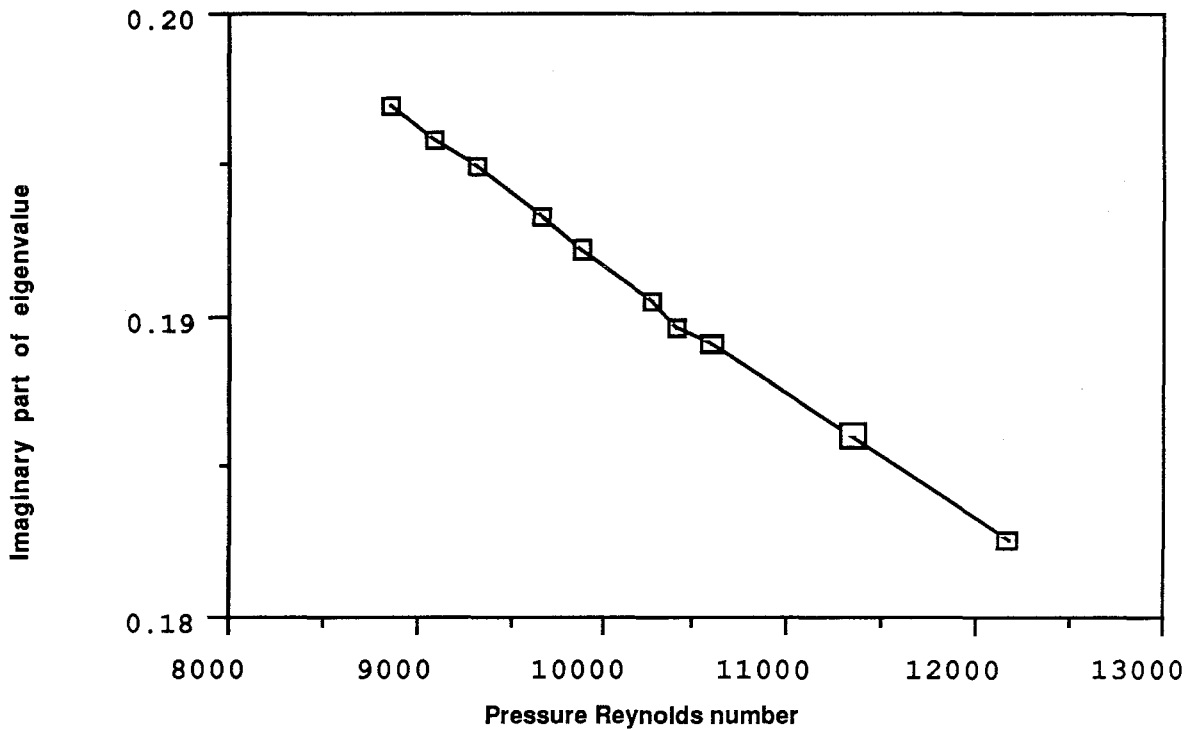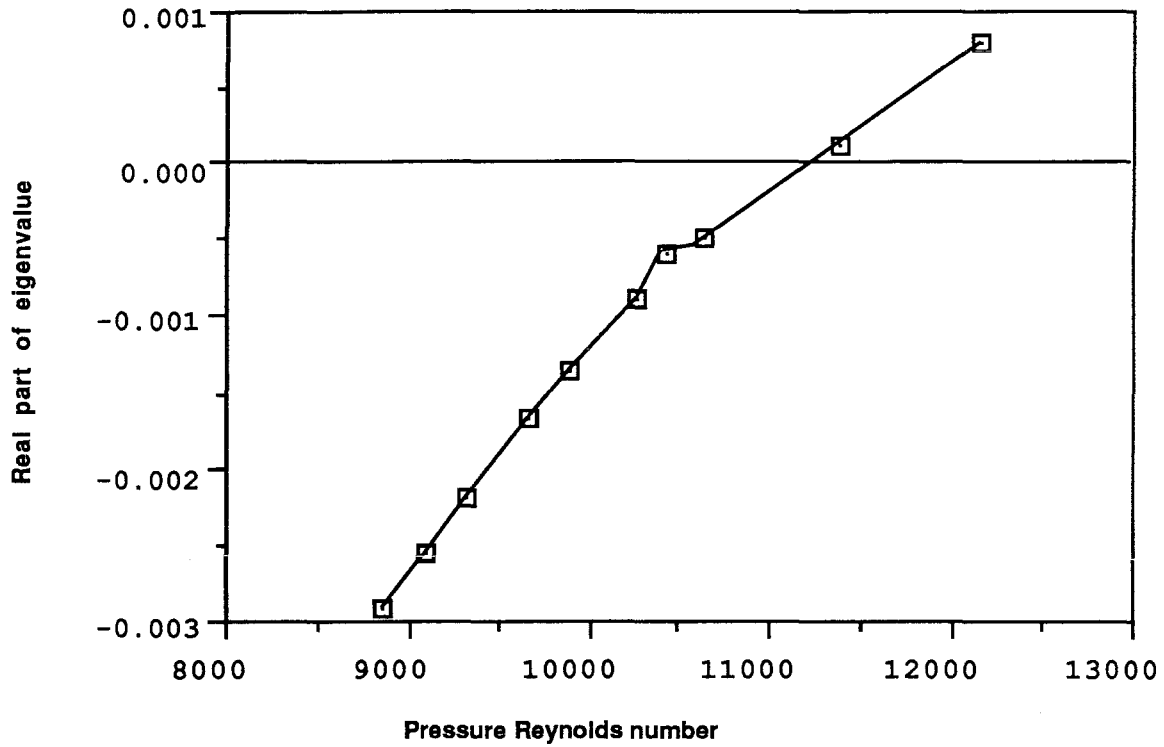
Figure 3.15. Third Hopf bifurcation for P disturbances, N=2.

N=2,K=70 and ,wave number is 1.1.
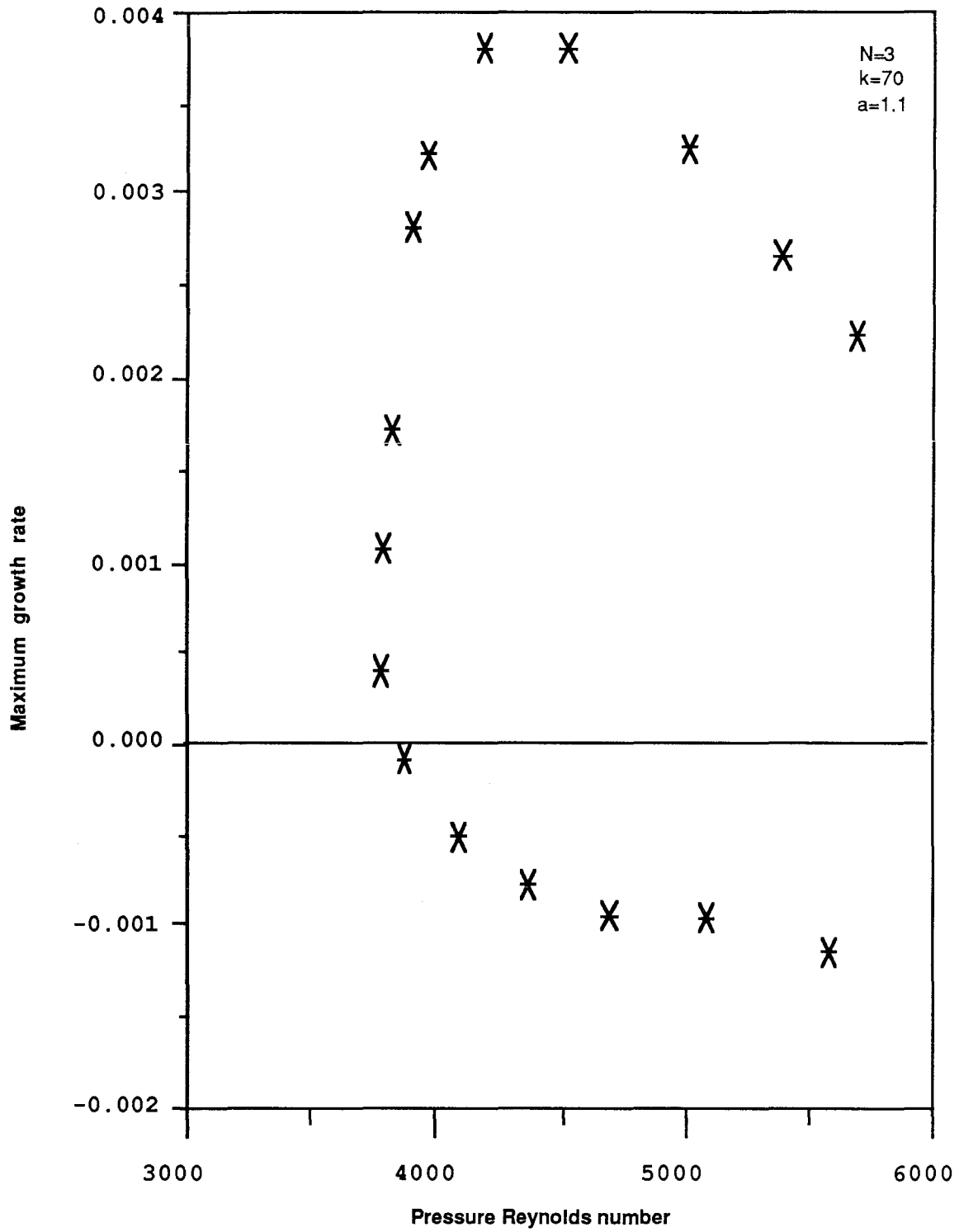
Figure 3.16. Maximum growth rate for 2D pressure disturbances, N=3.

Table 3.3. Reynolds number and period of first Hopf bifurcation for constant P disturbances.
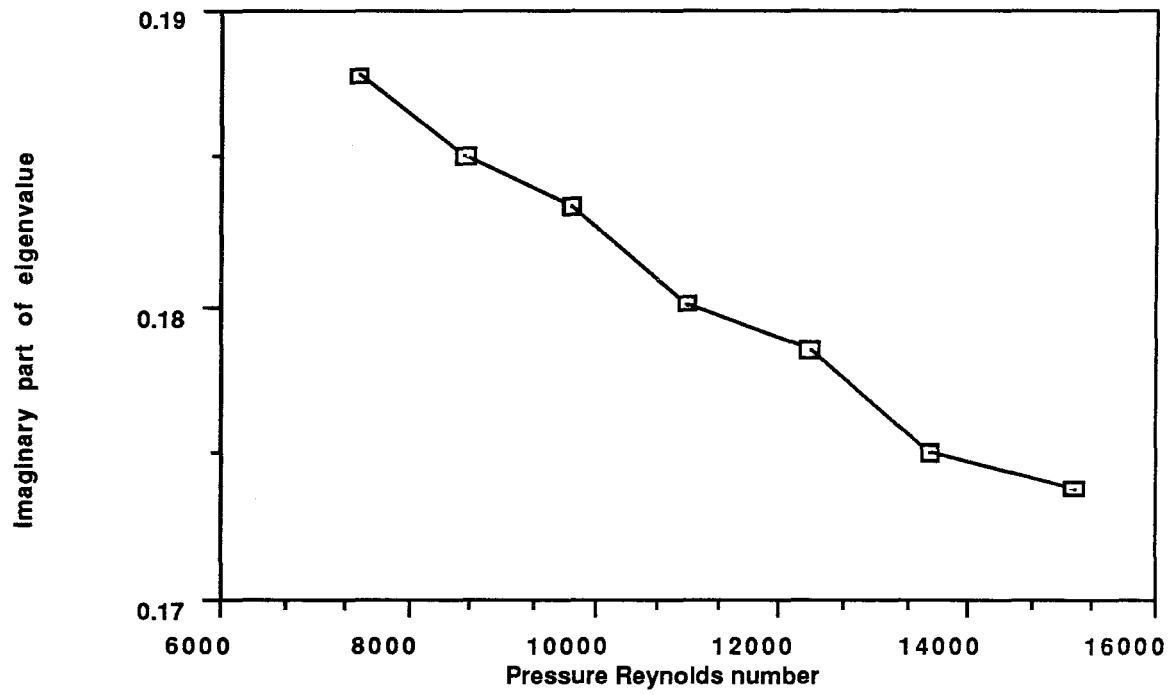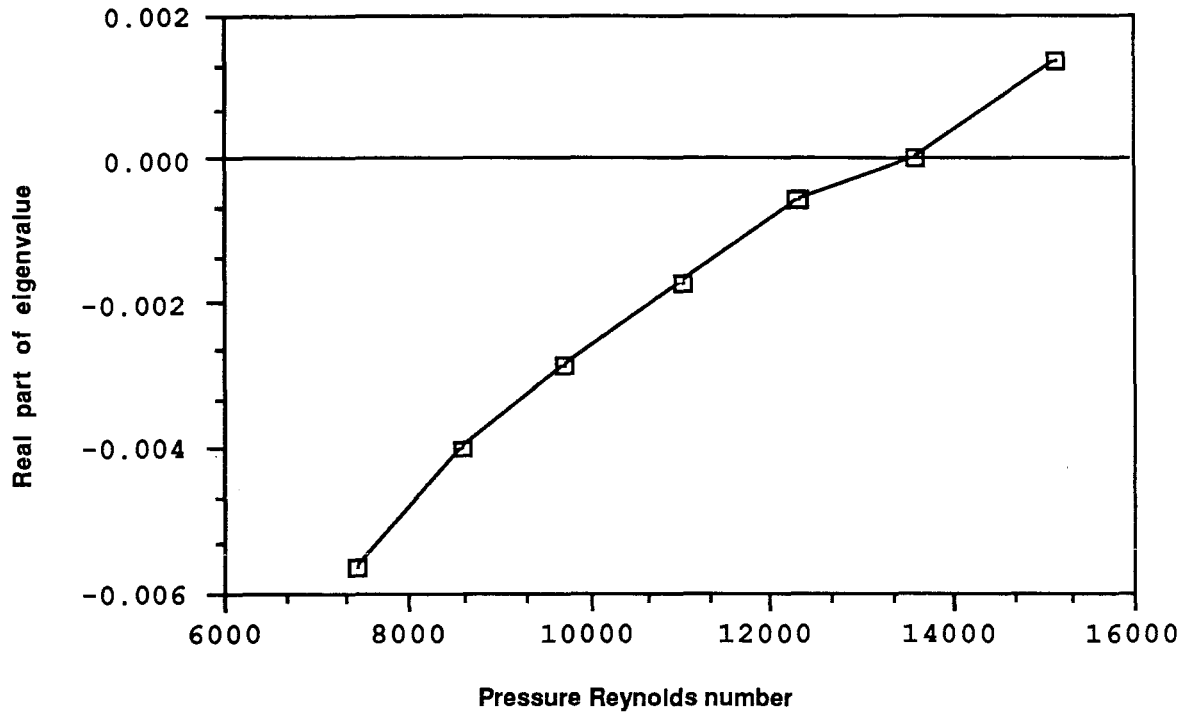
Parameter	N=1	N=2	N=3	N=4
Re	3136	3630	3800	3775
T	4833.22	4742.32	4935.43	4875.63

Table 3.4. Reynolds number and period of second Hopf bifurcation for constant P disturbances.

Parameter	N=1	N=2	N=3	N=4
Re	13500	9400	9675	9592
T	36	35.5	17.65	16.54

Table 3.5. Reynolds number and period of third Hopf bifurcation for constant P disturbances.

Parameter	N=1	N=2	N=3	N=4
Re		13000	12775	12960
T		34.0	33.76	33.85

3.5 Summary

In summary, we have calculated the 2D superharmonic stability of 2D waves for constant flux and constant pressure disturbances. For constant flux disturbances, the lower branch is unstable with a stability transition occurring at the turning point. In addition, there are two Hopf bifurcations occurring on the upper branch. These Hopf bifurcations correspond to two different pairs of eigenvalues destabilizing on the upper branch. For constant pressure disturbances the lower branch is unstable but a stability transition does not occur at the nose. Instead, another eigenvalue becomes neutrally stable at the nose and goes unstable on the upper branch. The two unstable eigenvalues merge and stabilize. The point of stabilization is a Hopf bifurcation. In addition there are two other Hopf bifurcations on the upper branch. As in the constant flux disturbances, these Hopf bifurcations correspond to two different pairs of eigenvalues destabilizing on the upper branch.

These results suggest that the 2D stability of 2D waves may depend on how the experiment is conducted. It is possible to build apparatuses that satisfy the constant pressure or constant flux requirement. In addition, we have found several bifurcations to quasi-periodic flows. In the next chapter, we calculate these flows and determine if they exist below a Reynolds number of 2600.

CHAPTER 4

QUASI-PERIODIC SOLUTIONS

4.1 Introduction

In this chapter, we study several branches of quasi-periodic solutions which bifurcate from the 2D travelling waves. Jimenez (1987) used a time dependent code to follow one of the branches that we will discuss. Our approach will be to look for quasi-periodic solutions by solving boundary value problems via continuation and Newton's method. This approach allows us to calculate both stable and unstable solution branches. Because we are studying the transition regime both stable and unstable solutions are of interest.

4.1 Problem Formulation

Consider the dimensionless form of the 2D Navier-Stokes equation in a moving frame of reference with speed c:

$$\frac{\partial}{\partial t}(\nabla^2 \Psi) - \frac{1}{Re}\nabla^4 \Psi + (\Psi_y - c)\nabla^2 \Psi_x - \Psi_x \nabla^2 \Psi_y = 0. \tag{4.1}$$

We look for solutions of the form

$$\psi(x, y, t) = \psi_b + \sum_{n=-\infty}^{\infty} \sum_{m=-\infty}^{\infty} e^{im\omega t} e^{in\alpha x} \hat{\psi}_{mn}(y), \tag{4.2}$$

where ω is the frequency introduced by the quasi-periodic flow and ψ_b is the streamfunction of the basic flow.

Substituting (4.2) into (4.1), we derive a modal equation for each $\hat{\psi}_{mn}$:

$$-\frac{1}{Re}(S_x^4 + 2S_x^2\frac{d^2}{dy^2} + \frac{d^4}{dy^4})\hat{\psi}_{mn} + (U-c)(S_x^2 + \frac{d^2}{dy^2})S_x\hat{\psi}_{mn} - U''S_x\hat{\psi}_{mn}$$

$$+\hat{\psi}_y * (S_x^2 + \frac{d^2}{dy^2})S_x\hat{\psi} - (S_x\hat{\psi}) * (S_x^2 + \frac{d^2}{dy^2})\frac{d\hat{\psi}}{dy} + im\omega(\frac{d^2}{dy^2} + S_x^2)\hat{\psi}_{mn} = 0, \quad (4.3)$$

where $S_x f_n = i\alpha n f_n$ and $f * g = \sum_{j=-\infty}^{\infty}\sum_{k=-\infty}^{\infty} f_{m-j,n-k}g_{jk}$ is the convolution of the two Fourier series. Because $\psi(x,y,t)$ is real, we require

$$\hat{\psi}_{m-n} = \hat{\psi}^*_{-mn}. \quad (4.4)$$

This implies we only need to solve for the modes $m \geq 0$ (for all n). The modal no slip boundary conditions are

$$\frac{d\hat{\psi}_{mn}}{dy} = 0 \quad \text{at} \quad y = \pm 1, \qquad m \geq 0 \quad \forall n$$

$$i\alpha n\hat{\psi}_{mn} = 0 \quad \text{at} \quad y = \pm 1, \qquad m \geq 0 \quad \forall n \neq 0. \quad (4.5)$$

For $n = 0$, $v_0 = (\frac{\partial\psi}{\partial x})_{n=0} = 0$ is identically satisfied, and we must specify $2(M+1)$ additional boundary conditions. As the streamfunction is arbitrary up to a function of time, we set

$$\psi(-1) = 0. \quad (4.6)$$

Applying (4.6) at every instant of time, we derive the $(M+1)$ boundary conditions

$$\hat{\psi}_{m0}(-1) = 0 \qquad m \geq 0. \quad (4.7)$$

The final $(M+1)$ boundary conditions are determined by fixing the parametrization of the problem. One possible parametrization is to disallow any perturbation to the spatially averaged flux. The spatially averaged flux (in dimensional variables) is

$$Q = \frac{\alpha}{2\pi}\int_0^{\frac{2\pi}{\alpha}}\int_{-h}^{+h} u \, dy \, dx. \quad (4.8)$$

Letting $u = \frac{\partial \Psi}{\partial y}$ and $\Psi = \Psi_b + \psi(x, y, t)$ we obtain

$$Q = [\Psi_b + \sum_{m=-\infty}^{\infty} \hat{\psi}_{m0} e^{im\omega t}]_{-h}^{+h}, \qquad (4.9)$$

where the streamfunction is in dimensional form. To disallow perturbations to Q, we set

$$[\sum_{m=-\infty}^{\infty} \hat{\psi}_{m0} e^{im\omega t}]_{-h}^{+h} = 0. \qquad (4.10)$$

Applying (4.10), together with (4.7), at every instant of time, we derive the $(M+1)$ additional boundary conditions

$$\hat{\psi}_{m0}(h) = 0 \qquad m \geq 0 \qquad (4.11a)$$

or in dimensionless form

$$\hat{\psi}_{m0}(1) = 0 \qquad m \geq 0. \qquad (4.11b)$$

Alternatively, one can disallow any perturbations to the spatially averaged pressure gradient. The spatially averaged pressure gradient (in dimensional variables) is

$$P = \frac{\nu}{2h}[\Psi_{b,yy} + \sum_{m=-\infty}^{\infty} \hat{\psi}_{m0,yy} e^{im\omega t}]_{-h}^{+h} - [\sum_{m=-\infty}^{\infty} im\omega \hat{\psi}_{m0} e^{im\omega t}]_{-h}^{+h}. \qquad (4.12)$$

To disallow perturbations to P, we set

$$\sum_{m=-\infty}^{\infty} e^{im\omega t}[\frac{\nu}{2h} \hat{\psi}_{m0,yy} - im\omega \hat{\psi}_{m0}]_{-h}^{+h} = 0. \qquad (4.13)$$

Applying (4.13) at every instant of time, we derive the $(M+1)$ additional boundary conditions

$$\frac{\nu}{2h}[\hat{\psi}_{m0,yy}]_{-h}^{+h} = im\omega[\hat{\psi}_{m0}]_{-h}^{+h} \qquad (4.14a)$$

or in dimensionless form

$$\frac{1}{Re}[\hat{\psi}_{m0,yy}]_{-1}^{+1} = im\omega[\hat{\psi}_{m0}]_{-1}^{+1}. \qquad (4.14b)$$

As in the case of 2D waves, a continuous range of boundary conditions can be obtained by taking linear combinations of (4.11) and (4.14). Also, the two boundary conditions define two different Reynolds numbers Re_P and Re_Q. These Reynolds numbers are defined by equations (2.20) and (2.22).

4.3 Numerical Method

To solve the system described by (4.3)-(4.7) with the additional boundary condition (4.11) or (4.14), we must impose two additional equations to eliminate the arbitrary phase shifts present in the problem. As in the case of 2D waves, we must eliminate the phase shift in x of the underlying secondary flow. In addition, the quasi-periodic flow introduces a phase shift in t. Specifically, if $\hat{\psi}_{mn}$ is a solution so is $\hat{\psi}_{mn} e^{im\delta\omega} e^{in\beta\alpha}$. To eliminate these phase shifts, we set

$$\frac{\Re(\hat{\psi}_{01}''(-1))}{\Im(\hat{\psi}_{01}''(-1))} = c1$$

and

$$\frac{\Re(\hat{\psi}_{11}''(-1))}{\Im(\hat{\psi}_{11}''(-1))} = c2 \tag{4.15}$$

where c1 and c2 are constants.

We also introduce an amplitude to continue into the nonlinear regime. We chose

$$A = (\sum_{m=-\infty}^{\infty} \sum_{n=-\infty}^{\infty} (\hat{\psi}_{mn})^2)^{\frac{1}{2}}. \tag{4.16}$$

Truncating (4.3) at a finite number of modes, it remains to solve a nonlinear system of ODE's with the additional equations (4.15)–(4.16) and the appropriate boundary conditions. We implemented the discretization method described in Chapter 2 to solve this system and used arclength continuation to compute the solution branches. An initial guess for these branches is provided by the eigenvectors found in the stability analysis described in Chapter 3.

4.4 Numerical Results

We first consider the Hopf bifurcations found in constant pressure disturbances. In Chapter three, we showed that a Hopf bifurcation occurs on the upper branch when a pair of complex conjugate eigenvalues stabilize (see Figure 3.11). In Figures (4.1)–(4.3) we plot amplitude versus Reynolds number for the quasi-periodic solutions which bifurcate from that Hopf bifurcation. The calculations shown were for $N = 1$ modes in x, $M = 1$ to $M = 3$ modes in time and $\alpha = 1.1$. As shown in Figure 4.1, for the $M = 1$ mode calculation the Reynolds number increases until reaching a limit point at 7400. The Reynolds number then decreases and the branch of quasi-periodic solutions terminates on the 2D wave branch at a Reynolds number of 3100. However, as can be seen from Figures 4.2 and 4.3, $M = 1$ modes yields ill resolved results. In Figure 4.2, we plot amplitude versus Reynolds number for $N = 1$ and $M = 2$ modes. For this calculation, the Reynolds number decreases and reaches a limit point at a Reynolds number of 3100. The same qualitative picture is seen in Figure 4.3 where we plot the results for $M = 3$ modes. We repeated these calculations for $N = 2$ and $M = 4$ modes and again no qualitative change was seen. In Figure 4.4, we show how c and ω vary on the branch. In Figures 4.5–4.8 we plot the appropriate graphs for $\alpha = 1.15$ and $\alpha = 1.21$.

In Figures 4.9(a) and 4.9(b) we plot constant vorticity lines for a Reynolds number of 3056 and $\alpha = 1.1$. The constant vorticity lines are for $y \in [-1, .78]$, $x \in [0, \frac{2\pi}{\alpha}]$, and $t \in [0, T]$ where $T = \frac{2\pi}{\omega}$. As can be seen from the plots, the effect of the modulation in time is to shift the high vorticity regions from left to right in x. The basic form of the flow appears unaffected. Because transition occurs on a convective time scale, it is highly unlikely that the modulation of the above flows would be observed in experiments. The period of the state shown in Figure 4.9 is 4932.

As the Reynolds number initially decreases with increasing amplitude, the periodic orbits emanating from the Hopf bifurcation are stable (Marsden and Mc-Cracken, 1976). One of the eigenvalues, however, will go through zero at the limit point of the periodic orbits. In addition, the branch may become unstable before the limit point. Because of the large memory requirements, we did not implement a Floquet analysis to determine when the branch becomes unstable.

Recently, Barkley (1988) has argued that the branch of quasi-periodic orbits could extend below the critical 2D wave Reynolds number only if certain events occured. For example, a secondary bifurcation would have to occur before the limit point of the 2D waves. Of course we know what occurs, the branch of quasi-periodic orbits reaches a limit point above the limit point of the 2D waves. This scenario has been shown by Barkley to be an acceptable picture in phase space.

It was hoped that this branch of quasi-periodic solutions would have flows existing below a Reynolds number of 2600 (based on constant flux). For all the wave numbers studied, however, no branches were found below a Reynolds number of 2600. The critical Reynolds number of the 2D waves is the envelope for the quasi-periodic solutions. As pointed out above, we did not implement a Floquet analysis of these orbits. The existence of a second Hopf bifurcation or a period doubling bifurcation can not be ruled out. Even if such bifurcations were found, however, the large amount of computer memory needed to calculate the solution branches makes such calculations impractical.

We now discuss the other Hopf bifurcations found in 2D waves. For both constant flux and constant pressure disturbances, two Hopf bifurcations were found on the upper branch (see Figures (3.5)–(3.6), and (3.14)–(3.15)). Our calculations showed that all the quasi-periodic solution branches which bifurcate from these Hopf bifurcations are qualitatively similar. Therefore we present a typical solution

branch which is representative of these results.

In Figure 4.10, we plot amplitude versus Reynolds number for the branch of quasi-periodic solutions which bifurcates from the Hopf bifurcation shown in Figure 3.5. The calculation shown was for $N = 2$ modes in x and $M = 2$ modes in time. This resolution was found to be adequate for these calculations. As shown in Figure 4.10, the Reynolds number increases with increasing amplitude. As the steady waves are stable before the Hopf bifurcation and unstable after, the branch of quasi-periodic solutions are locally stable to 2D disturbances. These results confirm the calculations by Jimenez (1987). Jimenez calculated the quasi-periodic solutions which bifurcate from the Hopf bifurcation shown in Figure 3.5. with a time dependent formulation. With our steady formulation, we obtain the same qualitative results which Jimenez found, i.e., the Reynolds number increases with increasing amplitude and the period of the orbits decreases with increasing amplitude. A quantitative comparison can not be made since Jimenez used many more modes. As in the case of 2D waves, however, we find that only a few modes are needed to give qualitative agreement.

We also calculated the branch of quasi-periodic solutions which bifurcate from the second Hopf bifurcation which occurs on the upper branch. In addition, we calculated the branch of quasi-periodic orbits which bifurcate from these two Hopf bifurcations for constant pressure disturbances. As discussed above, all of the branches are qualitatively similar, i.e. the Reynolds number increases with increasing amplitude.

In Figures 4.12(a) and 4.12(b), we plot constant vorticity lines for a Reynolds number of 5940 and $\alpha = 1.1$. The constant vorticity lines are for $y \in [-1, .78], t \in [0, T]$, and $x \in [0, \frac{2\pi}{\omega}]$. As can be seen from the Figures, the effect of the modulation in time is to oscillate vertically the regions of high vorticity. Jimenez (1987) used

a time-dependent code to calculate these flows and found similar results. He also noted that the vertical oscillation of vorticity is reminiscent of the "bursting" of vorticity seen in boundary layers. In addition, the time scale of these solutions and of the bursting is of the same order of the 3D flow. Thus, it is possible that these flows could coexist with the 3D flows and be a competing mechanism for the bursting of vorticity.

In summary, we have calculated the branches of quasi-periodic orbits which bifurcate from the 2D waves. For both constant pressure and constant flux disturbances, there are two branches of quasi-periodic solutions which bifurcate from the upper branch of the 2D waves. For these branches, we found that the Reynolds number increases with increasing amplitude. Thus the quasi-periodic orbits are stable to 2D disturbances. In addition, the time scale of these orbits are of the same order as 3D flows, and they exhibit phenomena which are reminiscent of "bursting".

We also calculated the branch of quasi-periodic orbits which only exists for constant pressure disturbances. For this branch, we found that the Reynolds number first decreases with increasing amplitude. A limit point, however, is reached above the critical Reynolds number of the 2D waves.
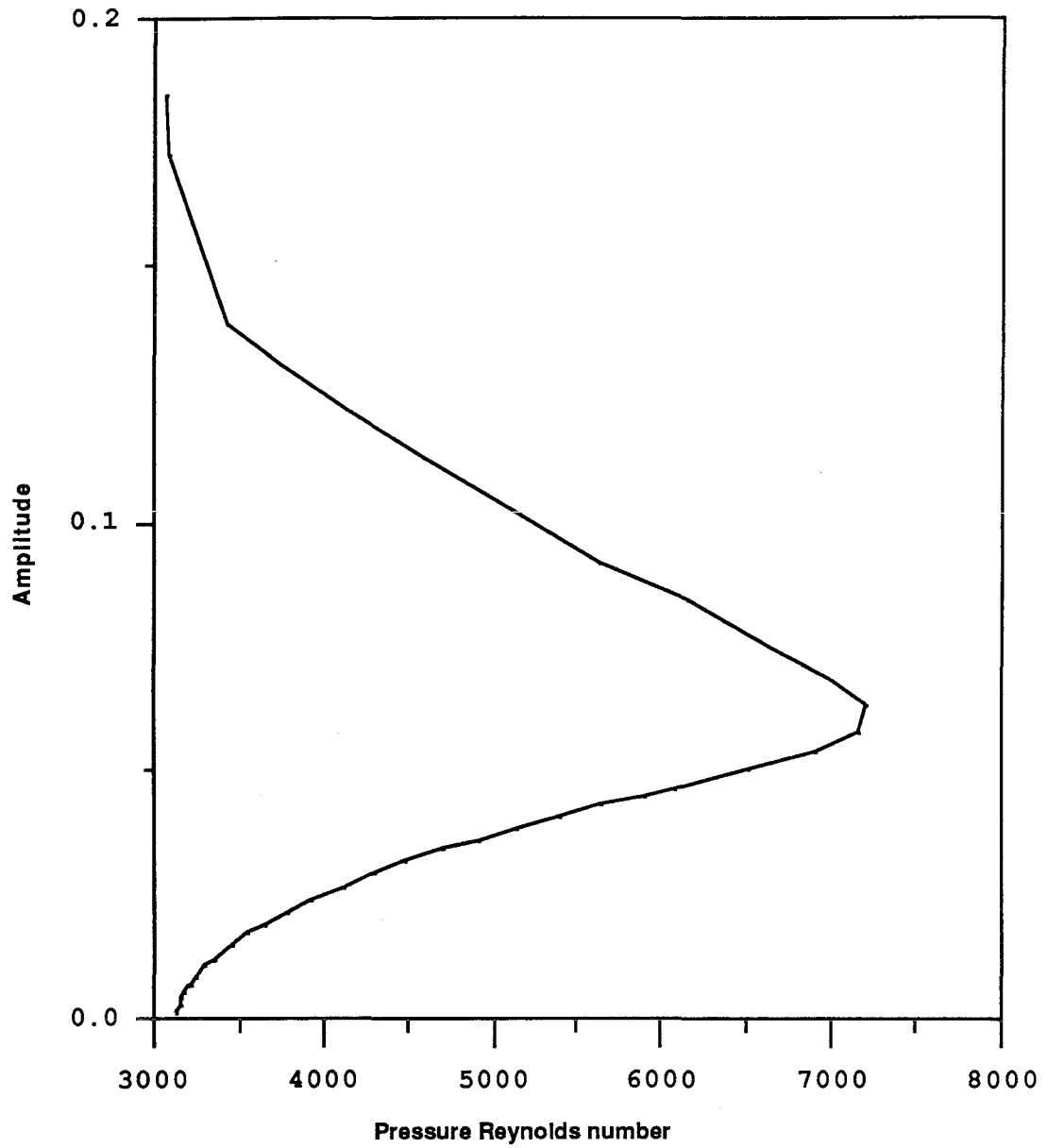
Figure 4.1. Amplitude as a function of Reynolds number for quasi-periodic solutions.
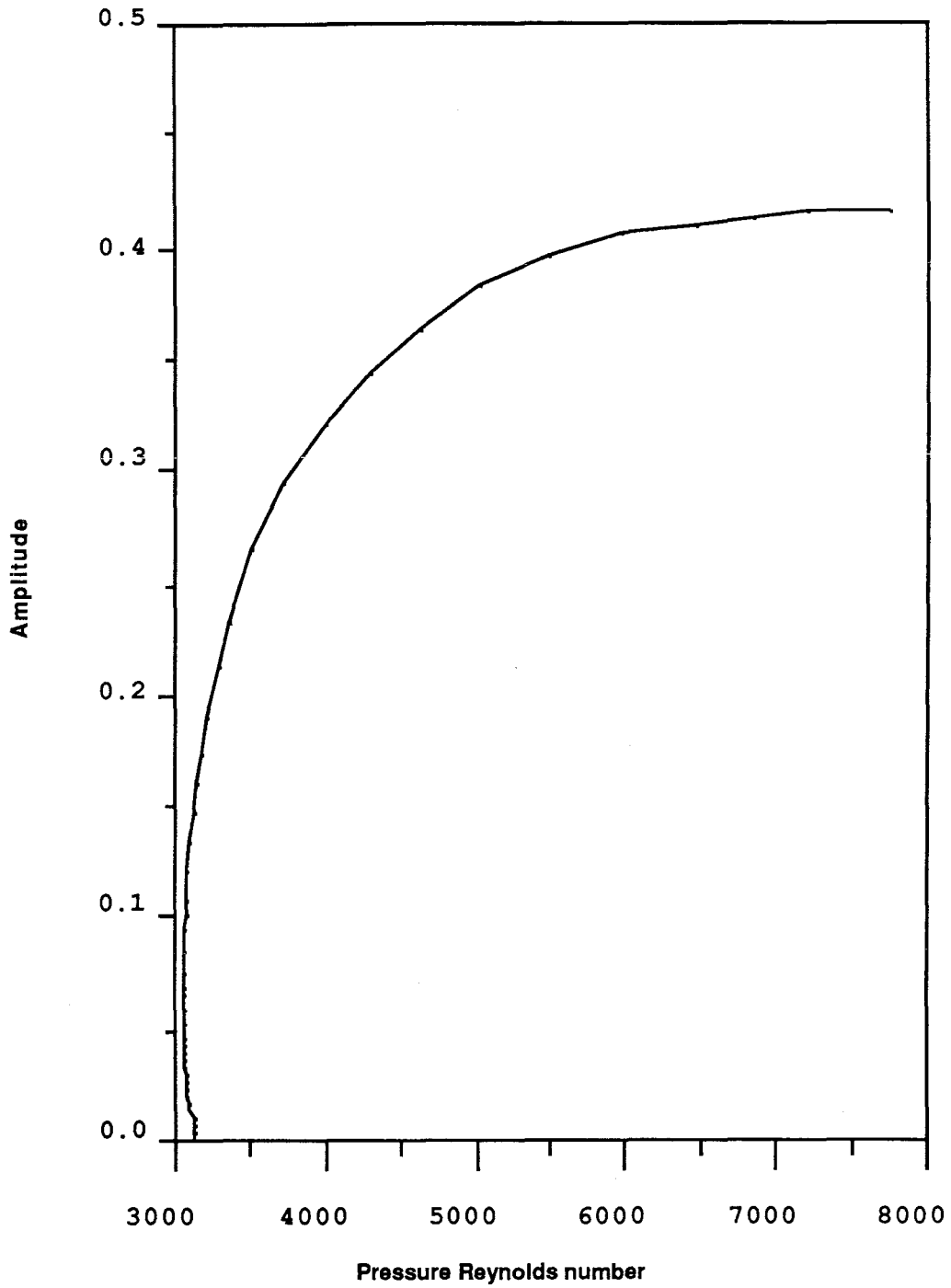N=1,M=1 and wavenumber is 1.1.

Figure 4.2. Amplitude as a function of Reynolds number for quasi-periodic solutions.
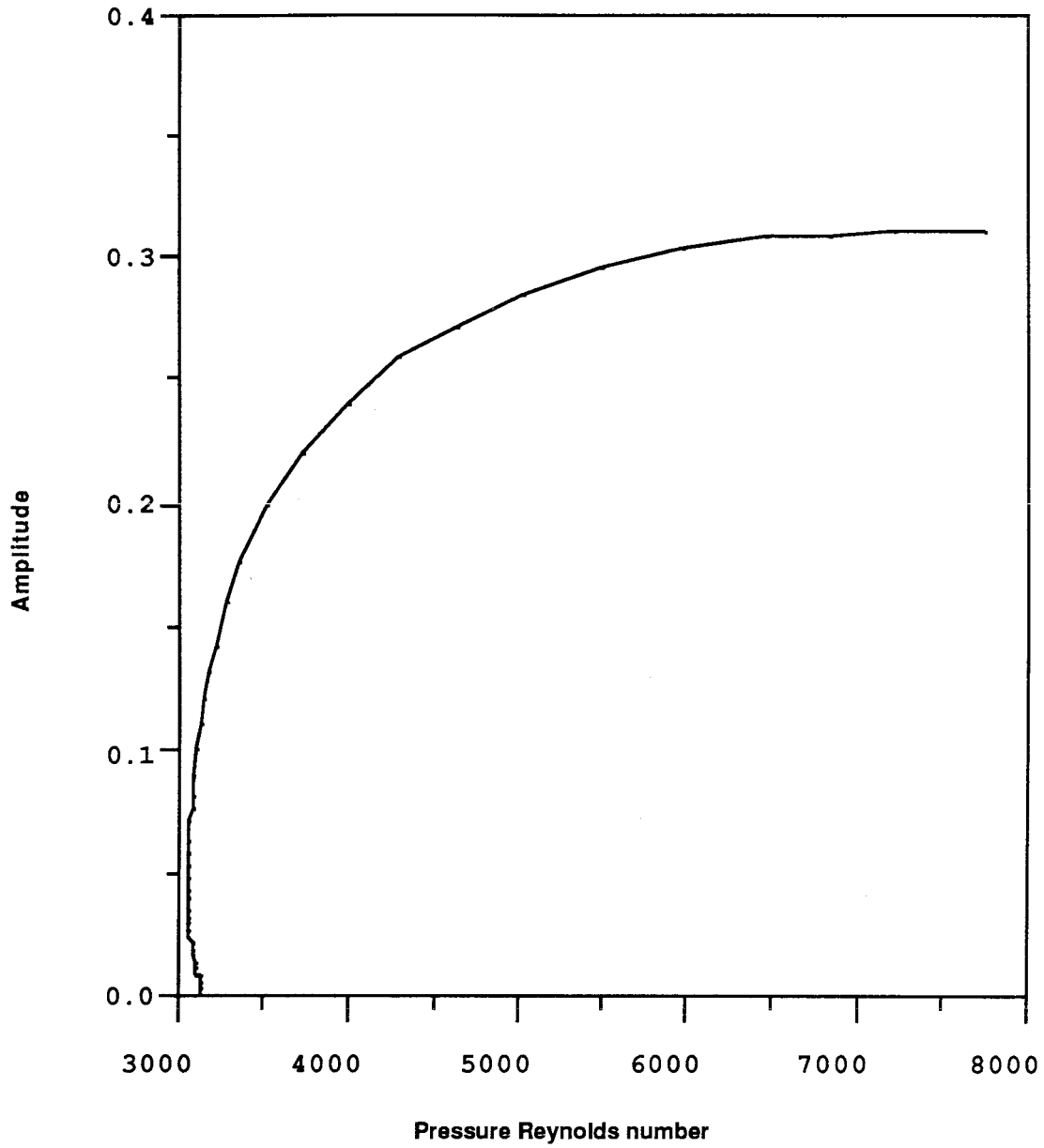N=1, M=2, and wave number is 1.1.

Figure 4.3. Amplitude as a function of Reynolds number for quasi-periodic solutions.
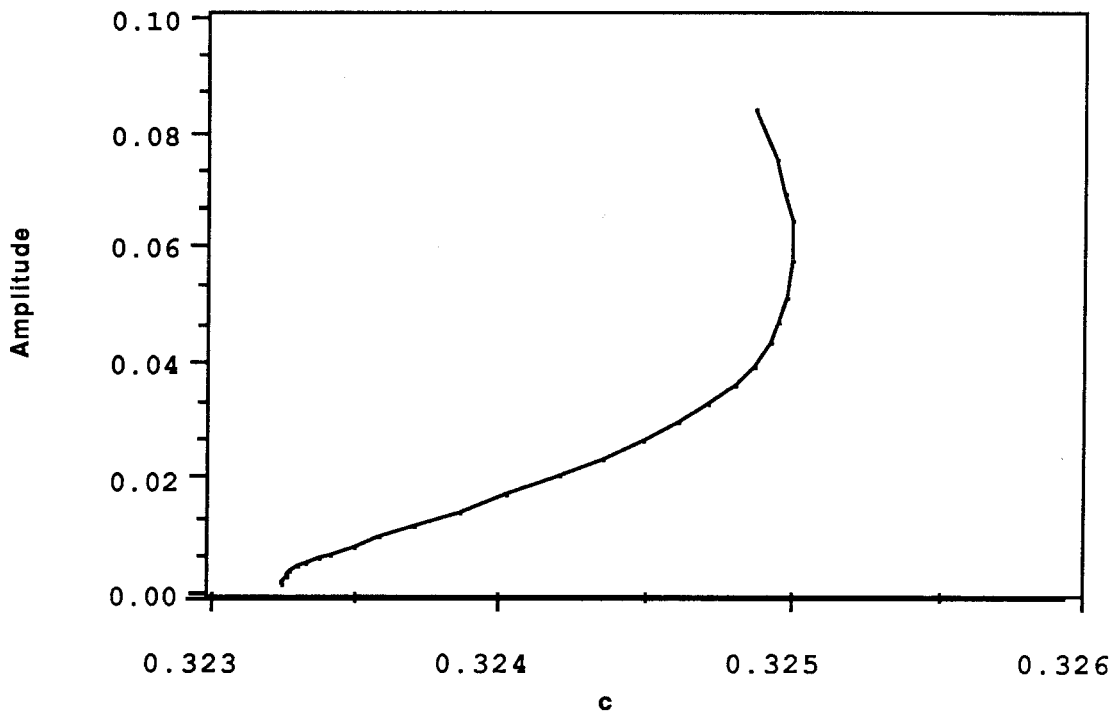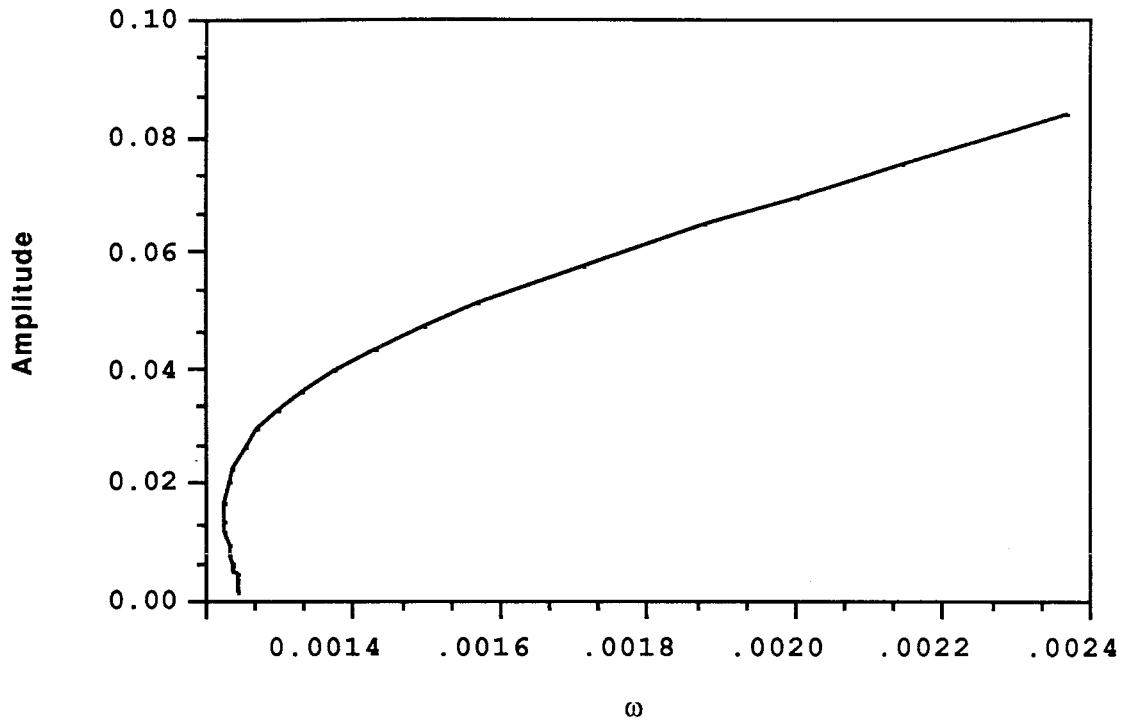
N=1,M=3 and wavenumber is 1.1.

Figure 4.4 Amplitude versus ω and c for quasi-periodic solutions.
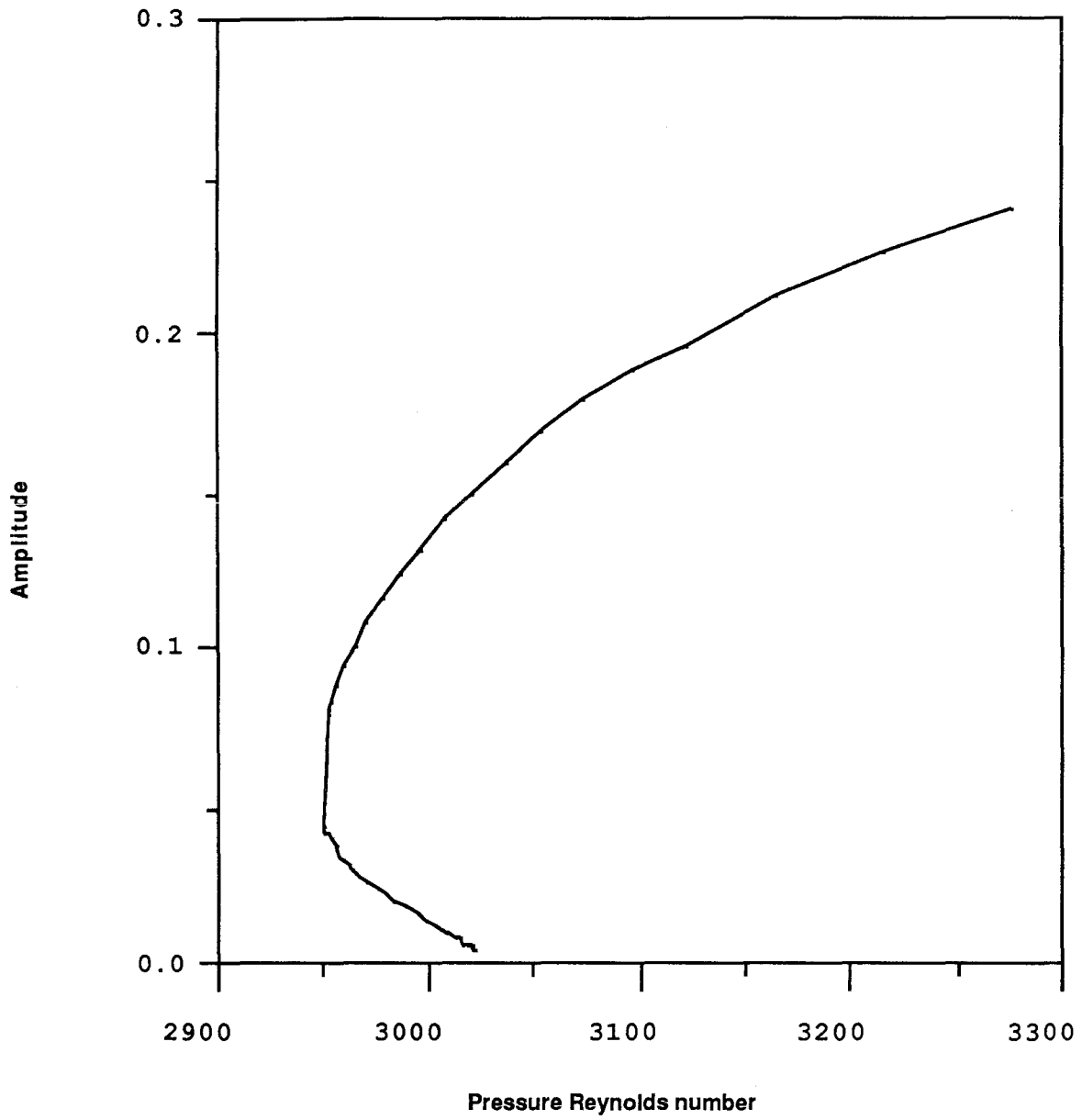N=1,M=2 and wave number is 1.1.

Figure 4.5. Amplitude versus Reynolds number for quasi-periodic solutions.

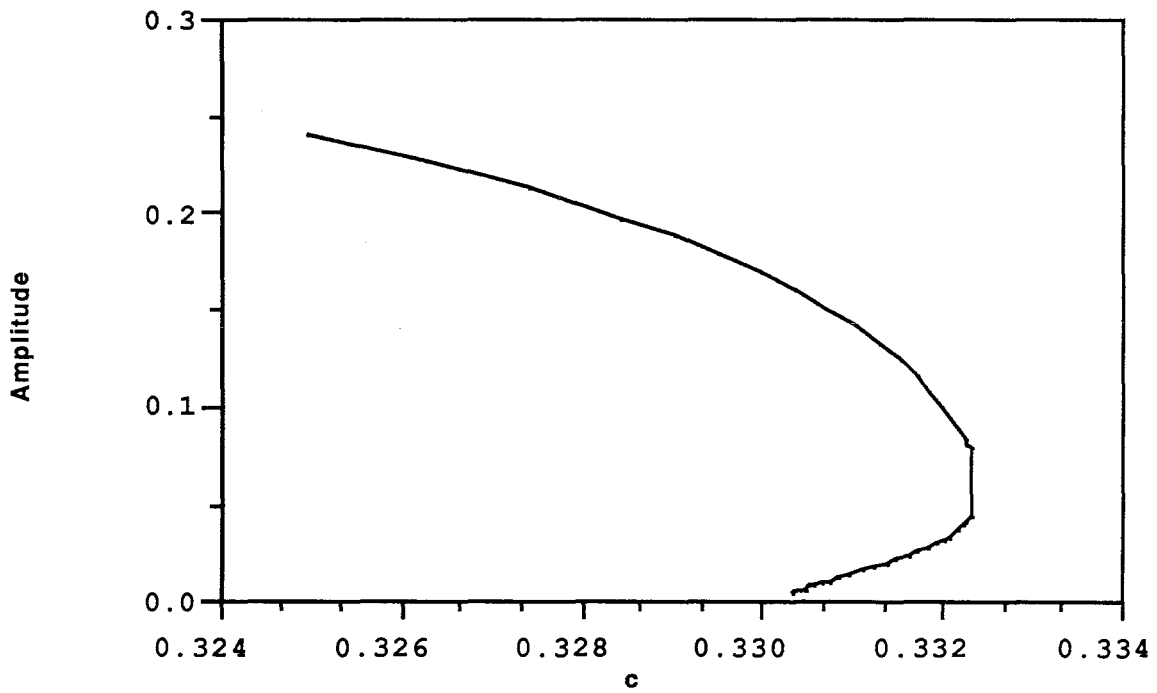N=1,M=2 and wavenumber is 1.15

Fig 4.6 Amplitude versus ω and c for quasi-periodic solutions.
N=1, M=2 and wavenumber is 1.15.

Figure 4.7. Amplitude versus Reynolds number for quasi-periodic solutions. N=1,M=2, and wave number is 1.21.

Figure 4.8. Amplitude versus ω and c for quasi-periodic solutions.
N=1,M=2 and wavenumber is 1.21.

Figure 4.9a. Constant vorticity lines. $y \in [-1, .78]$, $t = 0, \frac{1}{6}T, \frac{2}{6}T$ from top to bottom. $X \in [0, \frac{2\pi}{\alpha}]$, Reynolds number is 3056, and $\alpha = 1.1$

Figure 4.9b. Constant vorticity lines. $y \in [-1, .78]$, $t = \frac{3}{6}, \frac{4}{6}T, \frac{5}{6}T$ from top to bottom. $X \in [0, \frac{2\pi}{\alpha}]$, Reynolds number is 3056, and $\alpha = 1.1$
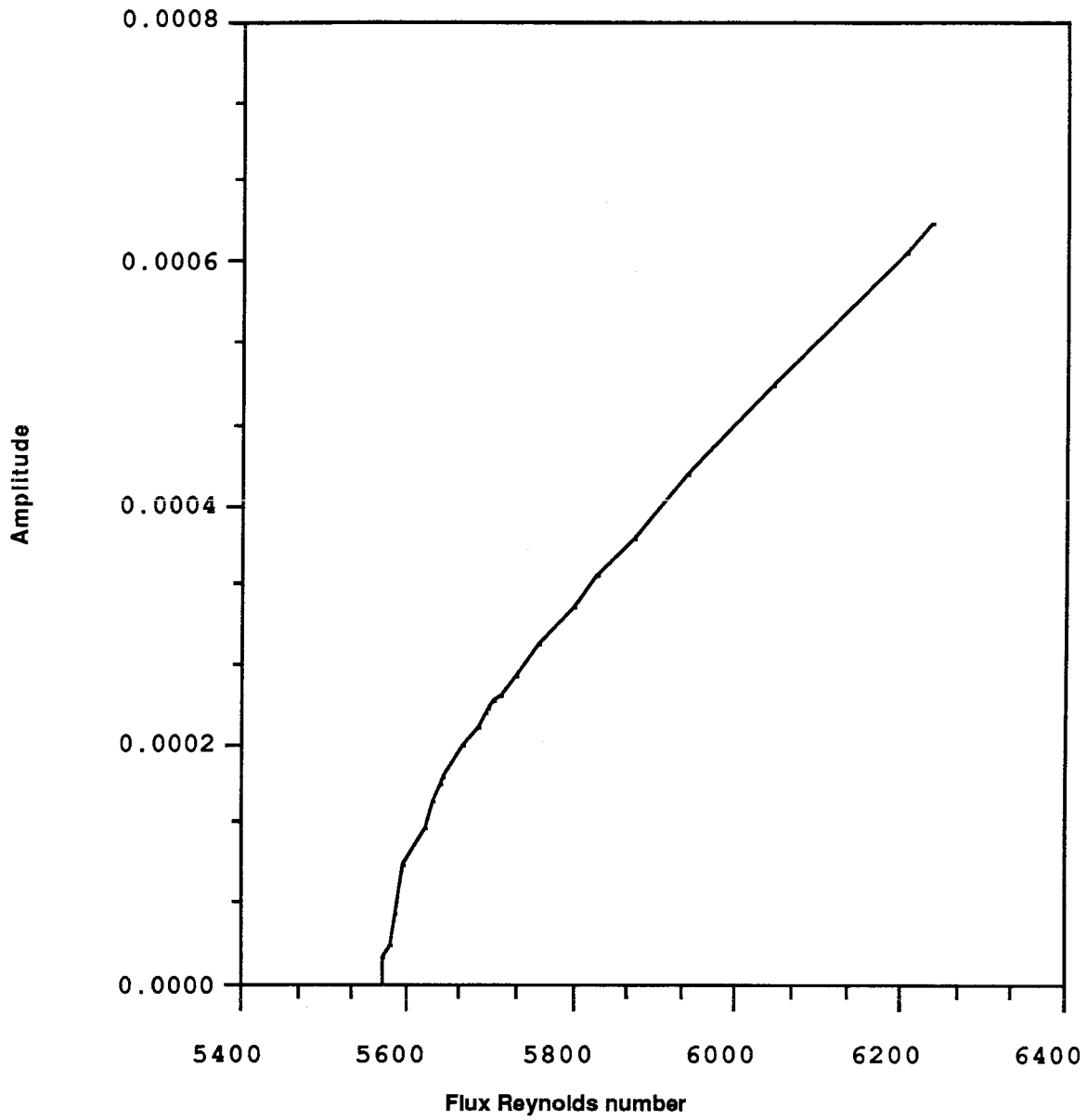
Figure 4.10. Amplitude versus Reynolds number for quasi-periodic solutions.
N=2,M=2 and wavenumber is 1.1
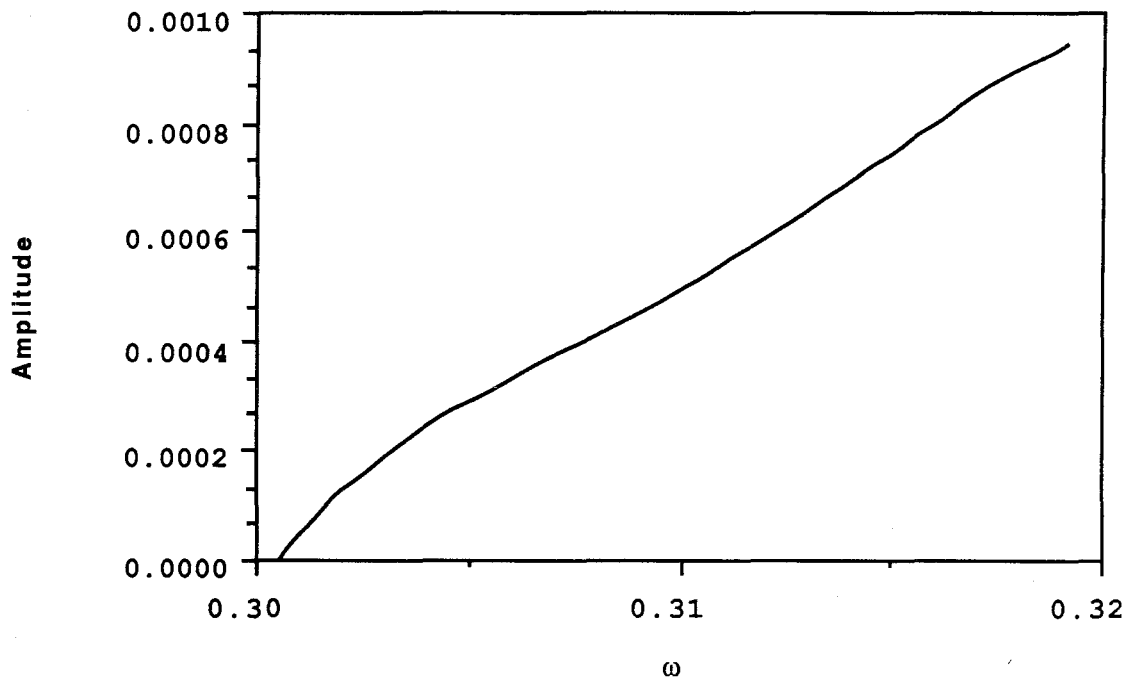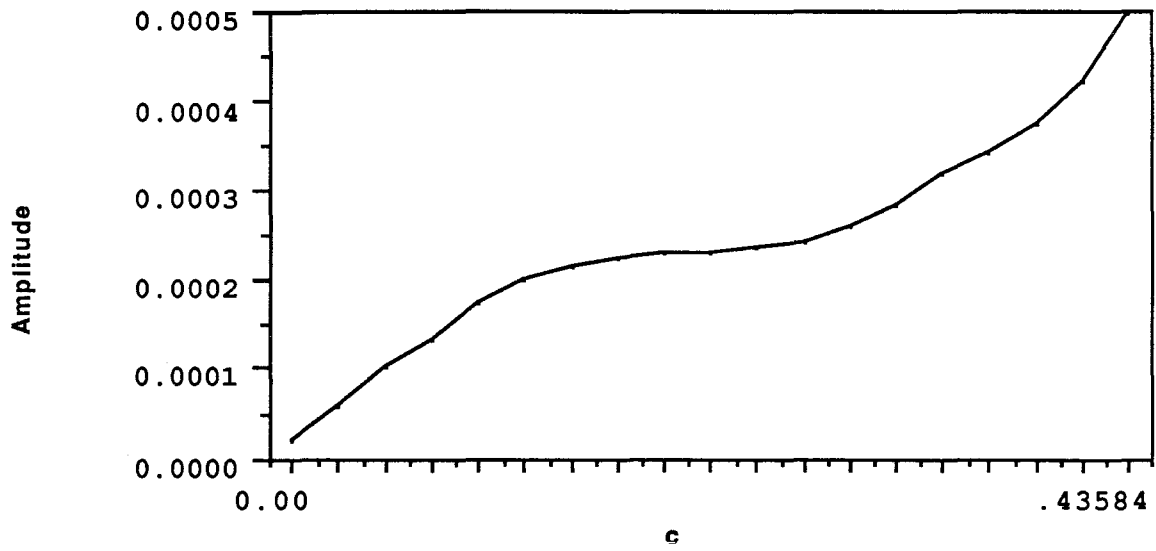
Figure 4.11. Amplitude versus c and ω for quasi-periodic solutions.
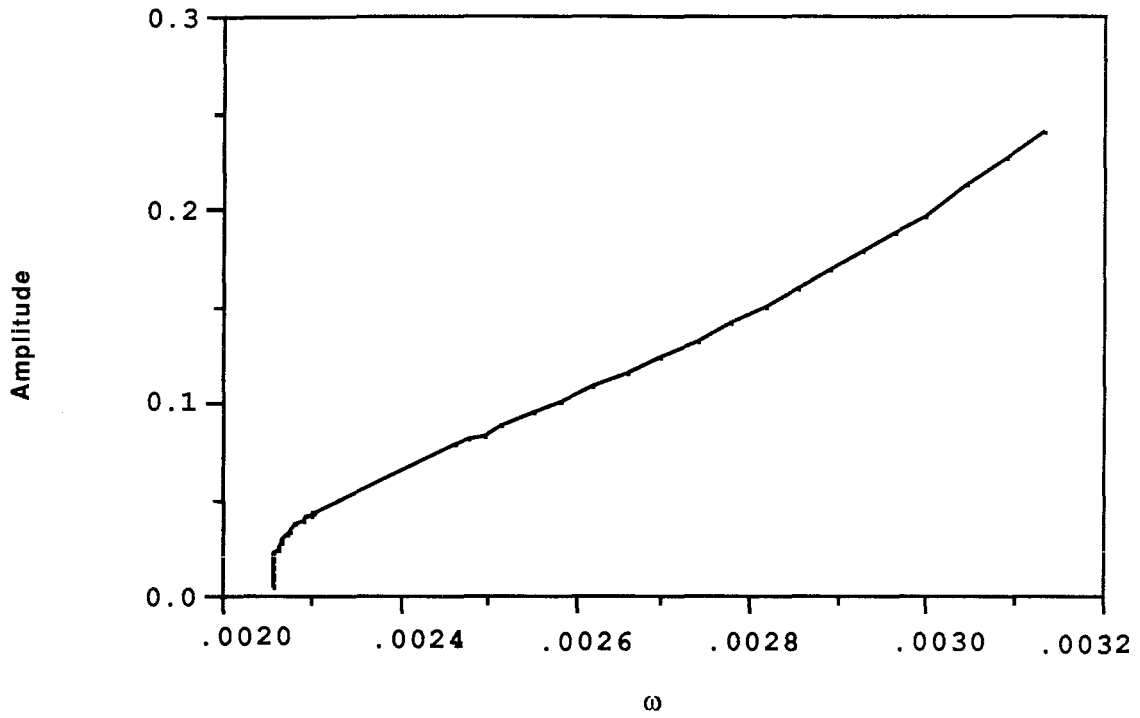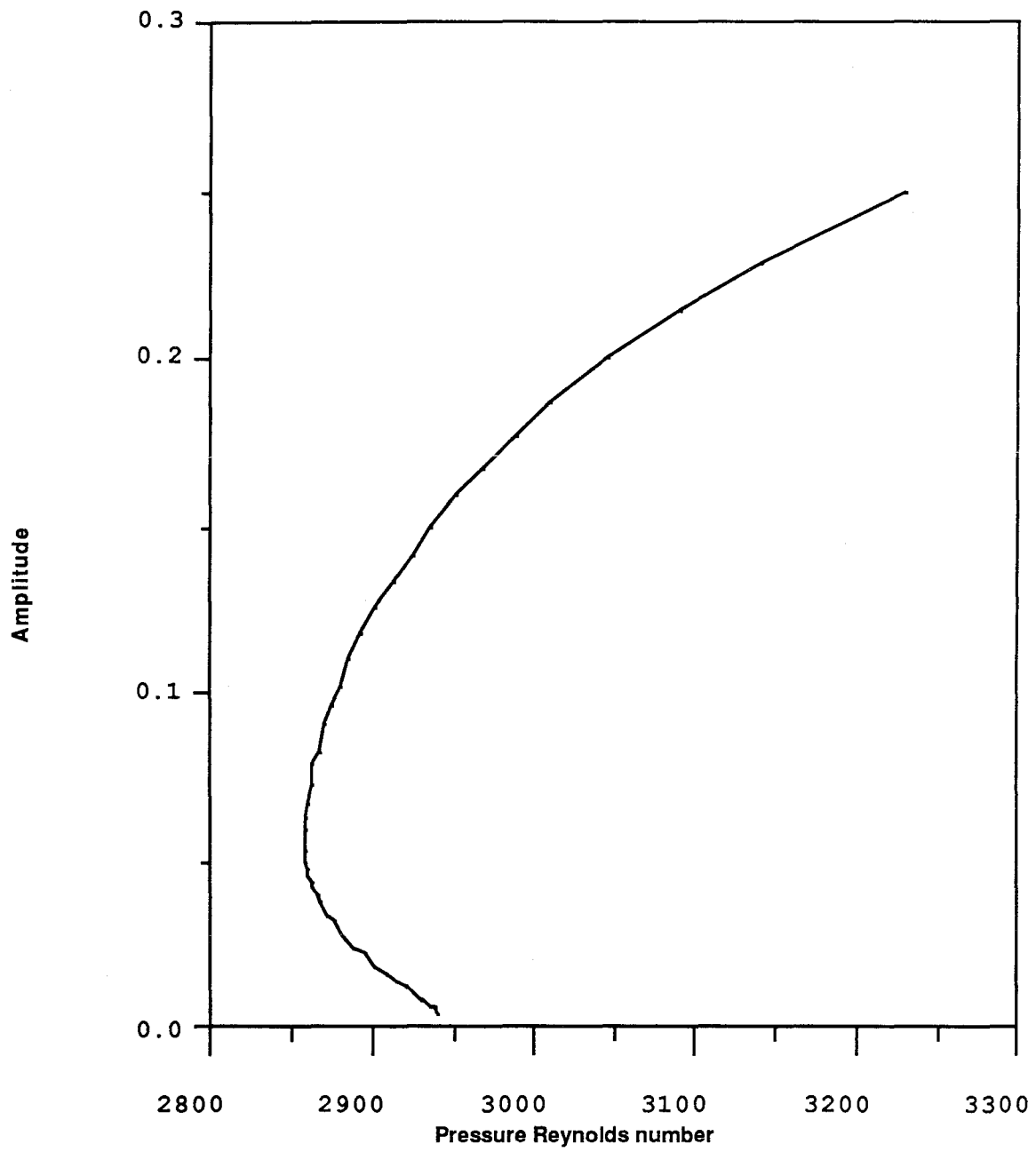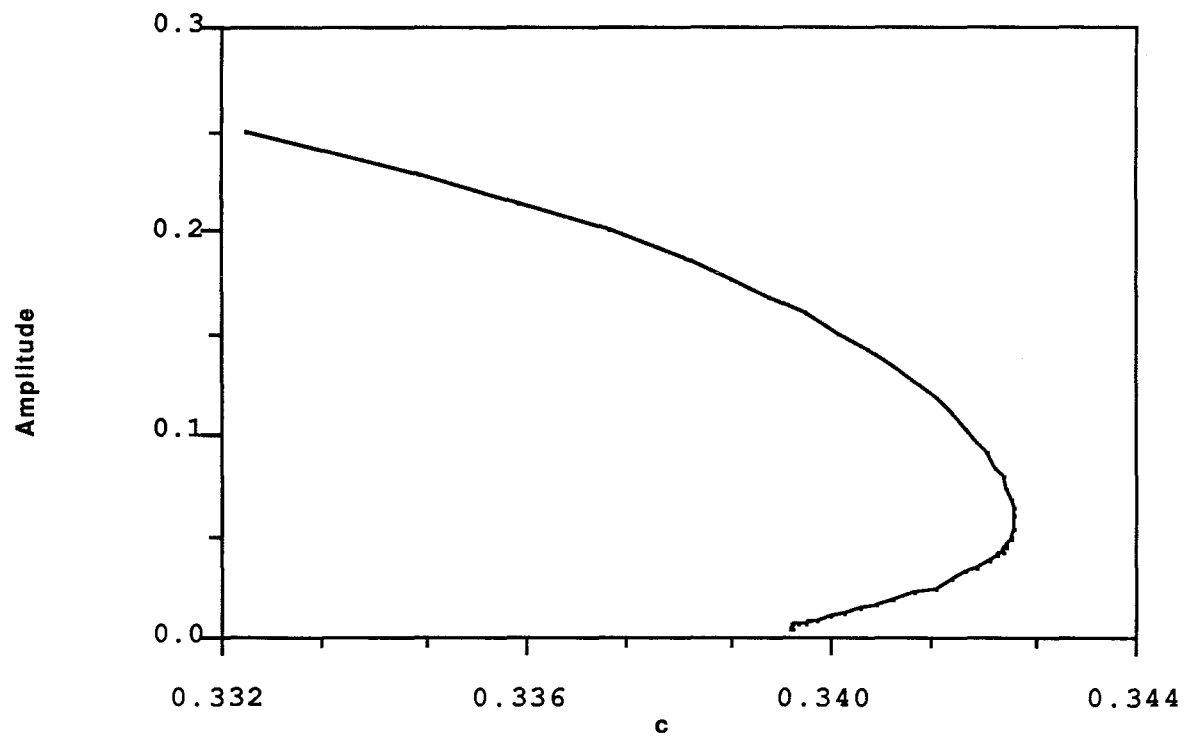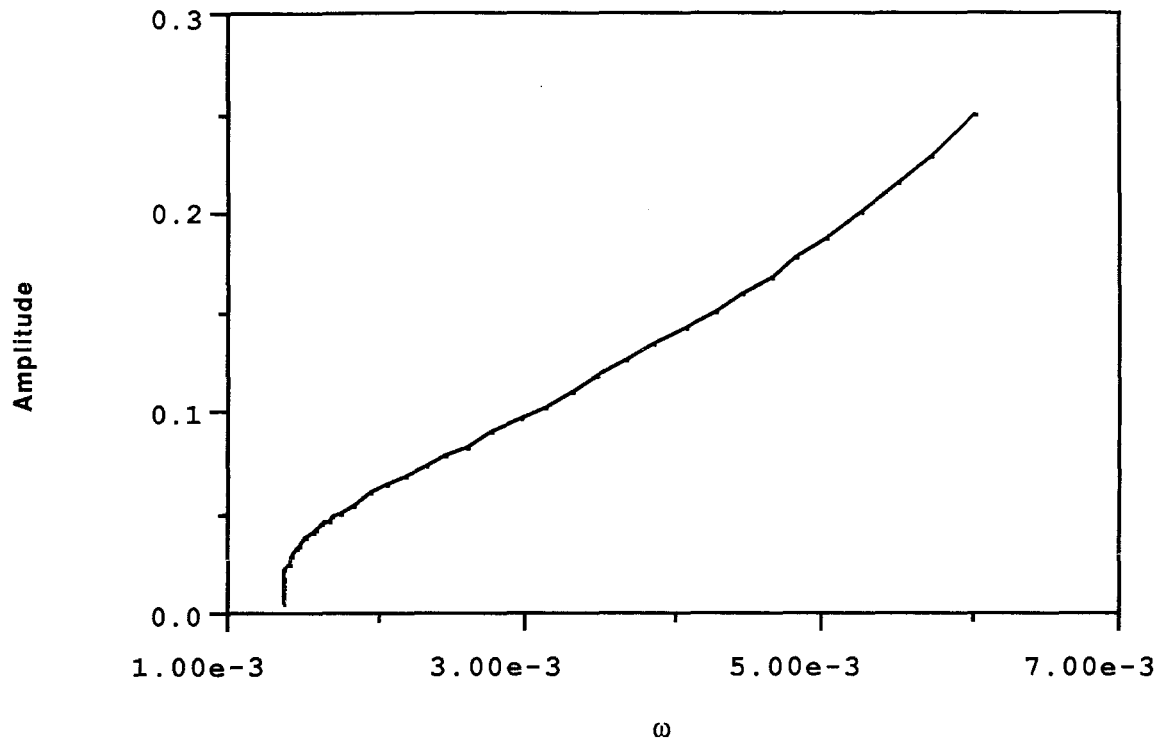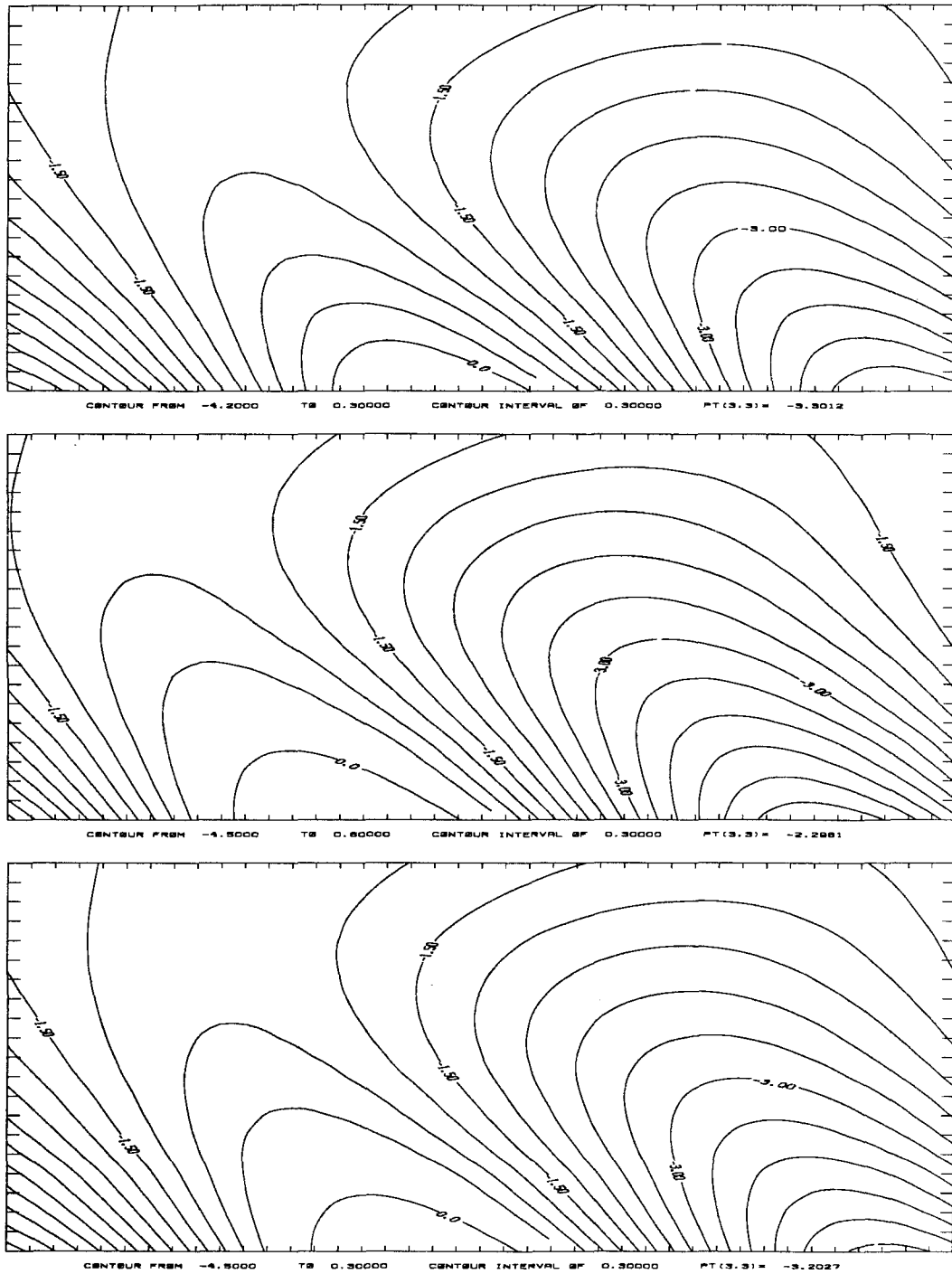N=2, M=2, and wavenumber is 1.1.
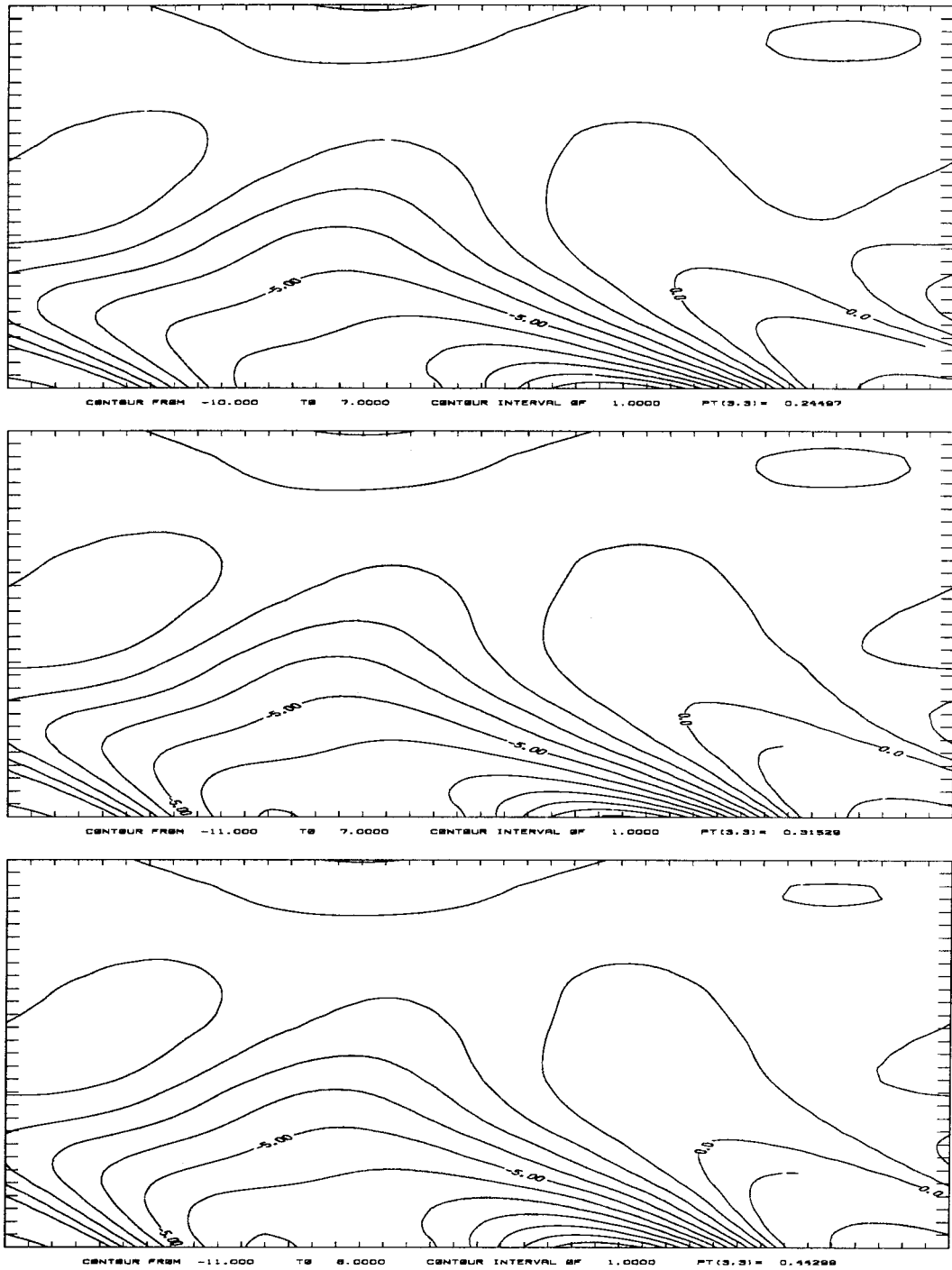
Figure 4.12a. Constant vorticitylines. $y \in [-1, .78]$, $t = 0, \frac{1}{6}T, \frac{2}{6}T$ from top to bottom. $X \in [0, \frac{2\pi}{\alpha}]$, Reynolds number is 5940, and $\alpha = 1.1$

CONTOUR FROM -12.000   TO 8.0000   CONTOUR INTERVAL OF 1.0000   PT(3.3)= 0.48744

CONTOUR FROM -11.000   TO 7.0000   CONTOUR INTERVAL OF 1.0000   PT(3.3)= 0.42467

CONTOUR FROM -11.000   TO 7.0000   CONTOUR INTERVAL OF 1.0000   PT(3.3)= 0.30879
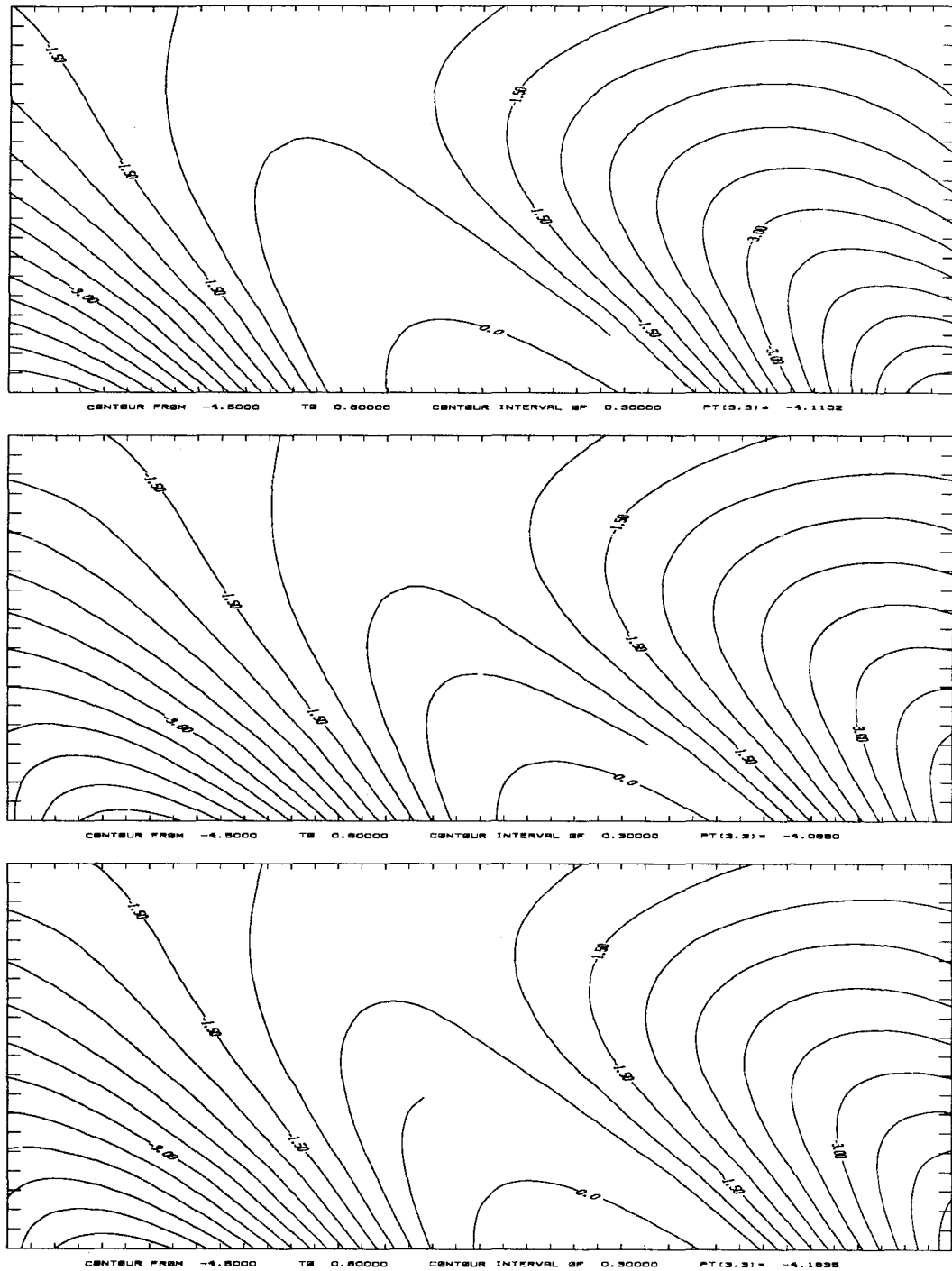
Figure 4.12b. Constant vorticity lines. $y \in [-1, .78]$, $t = \frac{3}{6}, \frac{4}{6}T, \frac{5}{6}T$ from top to bottom. $X \in [0, \frac{2\pi}{\alpha}]$, Reynolds number is 5940, and $\alpha = 1.1$

CHAPTER 5

STEADY THREE DIMENSIONAL WAVES

5.1 Introduction

In this chapter we study 3D steady waves. In particular we look at 3D waves which bifurcate from plane Poiseuille flow and from finite amplitude 2D waves. Bridges (1988) has shown that both 3D oblique waves and waves which are travelling in the streamwise direction and standing in the spanwise direction (STW) bifurcate from plane Poiseuille flow. We will study both STW and oblique waves. In addition, we study STW which bifurcate from finite amplitude 2D waves.

As in the previous chapters, we are looking for flows which exist at low Reynolds number. Rozhdestvensky and Simakin (1984) claimed to have found steady stable 3D flows at low Reynolds numbers for high spanwise wave numbers. In addition, Bridges (1988) observed from his local results that for high spanwise wave numbers it appeared pos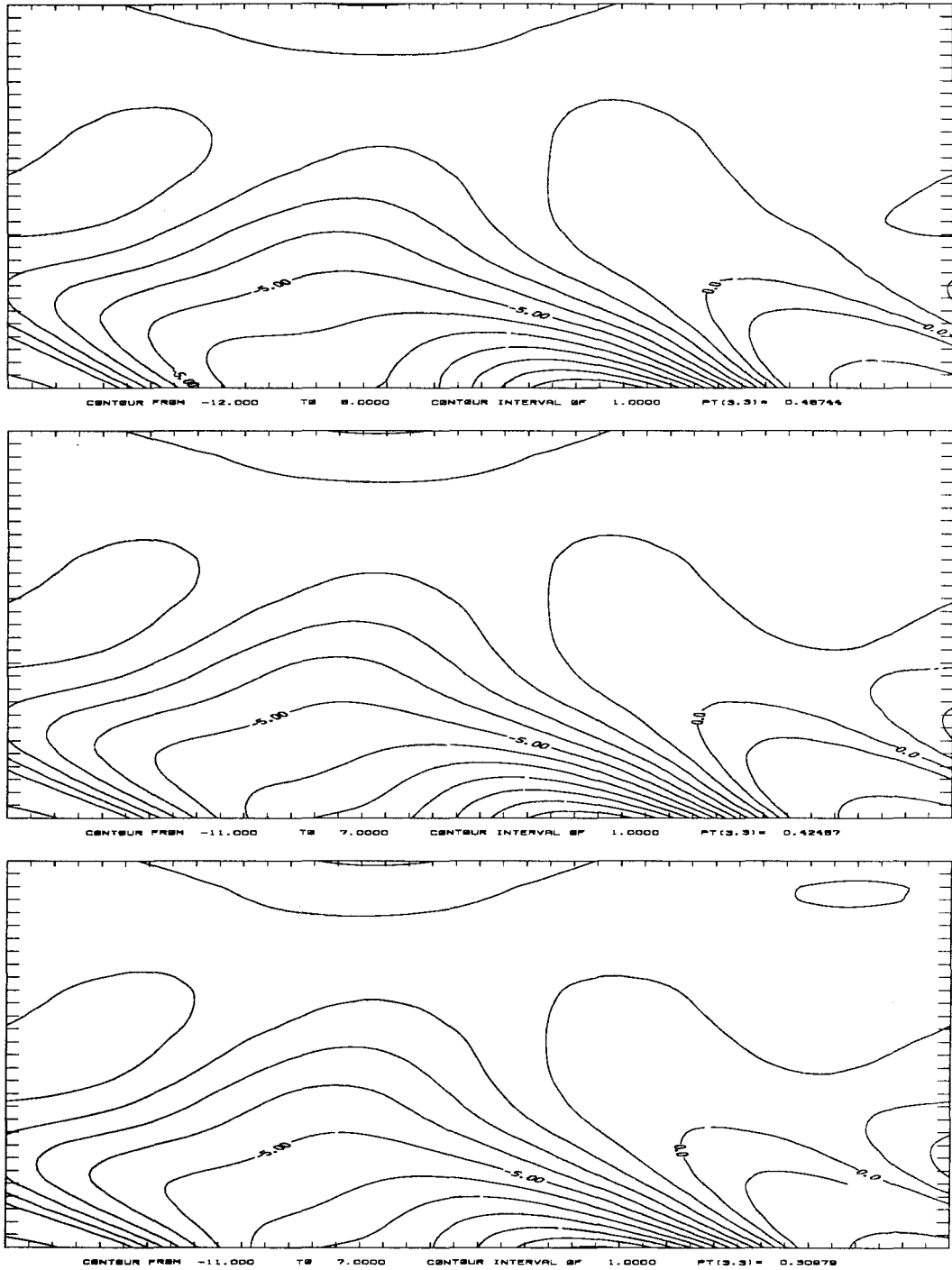sible that 3D flows would exist at low Reynolds numbers. We therefore concentrate our efforts by searching for bifurcations at high spanwise wave numbers.

5.2 Calculation of Bifurcation Points

We first consider bifurcations from plane Poiseuille flow to 3D waves. To calculate the bifurcation points to 3D waves, we study the 3D linear stability of plane Poiseuille flow (see Figure 5.1 which illustrates the configuration). Implementing a normal mode analysis, we perturb the basic flow with perturbations of the form:

$$[u, v, w, p]^T = [\hat{u}(y), \hat{v}(y), \hat{w}(y), \hat{p}(y)]^T \exp(i\alpha x + i\beta z - i\omega t), \qquad (5.1)$$

where α is the streamwise wave number, β is the spanwise wave number and ω is the frequency. Substituting (5.1) into the 3D Navier-Stokes equations and linearizing,
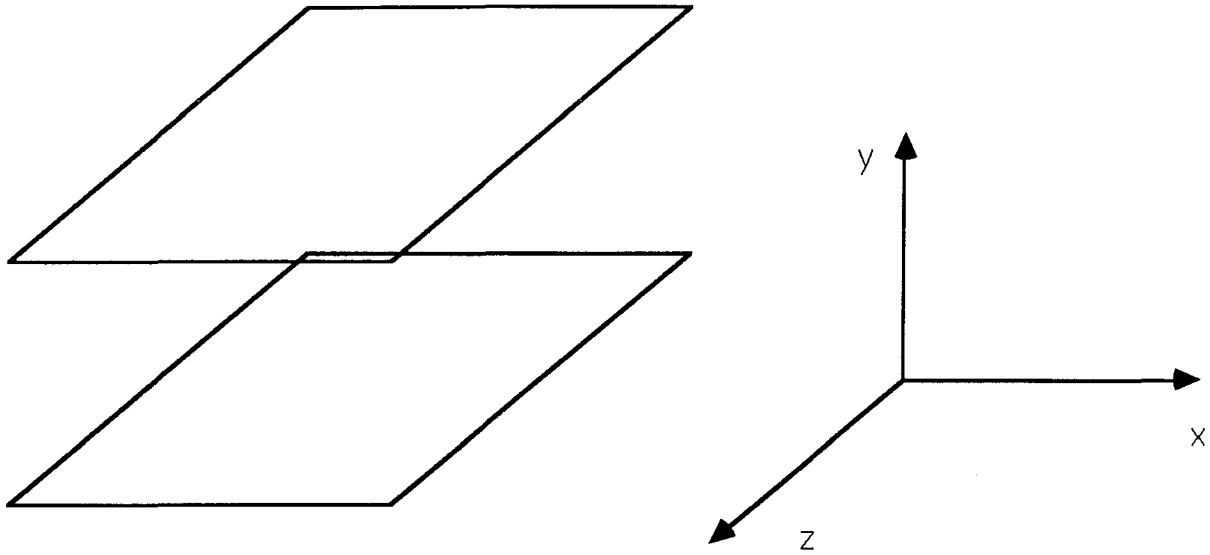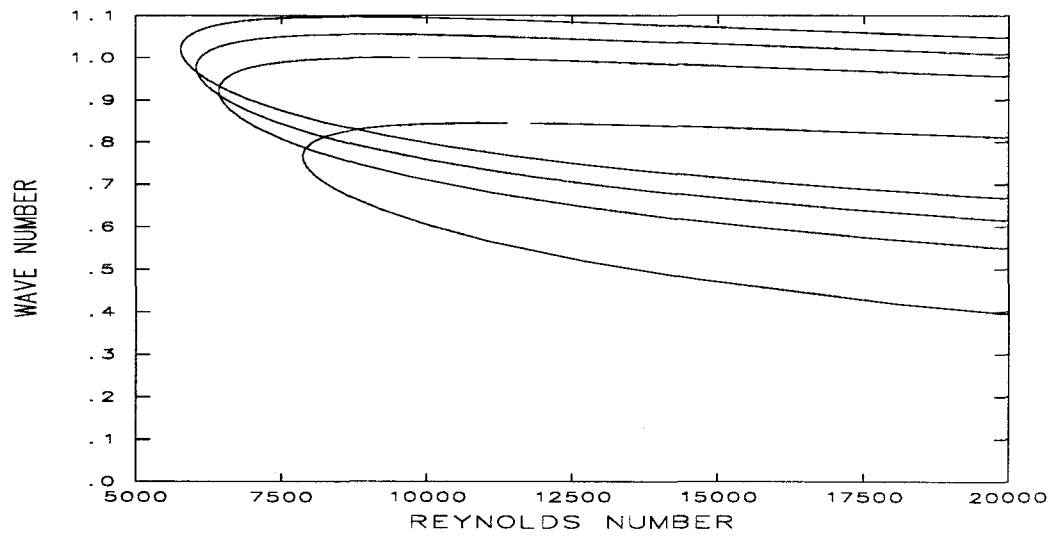
Figure 5.1. Flow Configuration.

Figure 5.2. Marginal stability curves for different values of β. $\beta = 0, .15., .45, .7$ from left to right.

we obtain

$$[D^2 - (\alpha^2 + \beta^2) - i\alpha Re(U - c)]u = ReDUv + i\alpha Rep$$

$$[D^2 - (\alpha^2 + \beta^2) - i\alpha Re(U - c)]v = ReDp$$

$$[D^2 - (\alpha^2 + \beta^2) - i\alpha Re(U - c)]w = i\beta Rep \tag{5.2}$$

$$i(\alpha u + \beta w) + Dv = 0,$$

where $D = \frac{d}{dy}$, $c \equiv \frac{\omega}{\alpha}$ and we have dropped the hats. The no slip boundary conditions are

$$u(\pm 1) = 0$$

$$v(\pm 1) = 0 \tag{5.3}$$

$$w(\pm 1) = 0.$$

By using Squire's transformation, the above problem can be reduced to an equivalent 2D problem (Drazin and Reid, 1981). Squire's transformation defines an equivalent 2D Reynolds number and wave number by

$$\tilde{\alpha} = (\alpha^2 + \beta^2)^{\frac{1}{2}} \qquad \tilde{\alpha}\tilde{Re} = \alpha Re. \tag{5.4}$$

From (5.4), we see that $\tilde{Re} < Re$ and therefore we need only to consider 2D disturbances to determine the critical Reynolds number. The above result is known as Squire's theorem.

In chapter 2, we solved the 2D stability problem and calculated the marginal stability curve. For each β, there is an equivalent marginal stability curve which can be determined by Squire's transformation. Several of these curves are shown in Figure 5.2. We also showed in chapter 2 that the points on the 2D marginal curve are bifurcation points to 2D travelling waves. For the 3D stability problem, the marginal stability curve is a curve of bifurcation points to 3D oblique waves and 3D STW (Bridges, 1988). As we have a marginal stability curve for each β, there is a surface of bifurcation points for 3D disturbances. Note that equation 5.1 is

the linear form for both oblique and STW. To determine the eigenvectors at these bifurcation points, we must solve the system of ODE's and boundary conditions described by (5.2)–(5.3).

We first apply the following transformation introduced by Hama (1987):

$$\tilde{\alpha}\tilde{u} = \alpha u + \beta w, \quad \tilde{\alpha}\tilde{w} = \alpha w - \beta u,$$

$$\tilde{\alpha}\tilde{U} = \alpha U, \quad \tilde{\alpha}\tilde{W} = -\beta U, \tag{5.5}$$

$$\tilde{\alpha}\tilde{x} = \alpha x + \beta z, \quad \tilde{\alpha}\tilde{z} = \alpha z - \beta x,$$

where $\tilde{\alpha} = (\alpha^2 + \beta^2)^{\frac{1}{2}}$. This is basically a transformation to a coordinate system in which the x direction is the direction of the wave vector and the z direction is the direction parallel to the wave front. With this transformation, (5.2) becomes

$$i(\tilde{\alpha}\tilde{U} - \omega)\tilde{u} + D\tilde{U}v = -i\tilde{\alpha}p + \frac{1}{Re}[D^2 - \tilde{\alpha}^2]\tilde{u} \tag{5.6a}$$

$$i(\tilde{\alpha}\tilde{U} - \omega)v = -Dp + \frac{1}{Re}[D^2 - \tilde{\alpha}^2]v \tag{5.6b}$$

$$i(\tilde{\alpha}\tilde{U} - \omega)\tilde{W} + D\tilde{W}v = \frac{1}{Re}[D^2 - \tilde{\alpha}^2]\tilde{w} \tag{5.6c}$$

$$i\tilde{\alpha}\tilde{u} + Dv = 0. \tag{5.6d}$$

Note that we are now using ω instead of c. Equations (5.6a), and (5.6b) together with (5.6d) are equivalent to the 2D stability problem solved in chapter 2. Specifically, the 2D stability equations are

$$i(\alpha U - \omega)u + DUv = -i\alpha p + \frac{1}{Re}[D^2 - \alpha^2]u$$

$$i(\alpha U - \omega)v = -Dp + \frac{1}{Re}[D^2 - \alpha^2]v$$

$$i\tilde{\alpha}\tilde{u} + Dv = 0.$$

Therefore, $\tilde{u}$, and $\tilde{v}$ are the same as those for the 2D problem with the transformed wave number $\tilde{\alpha}$. Note that this transformation does not change Re and ω. To solve the 3D stability problem, therefore, we use the vertical velocity computed from the

2D stability problem for the transformed wave number, and need only to solve for the spanwise velocity component. The streamwise velocity component can then be computed from the continuity equation.

In chapter 2, we described the discretization scheme used to solve the system given by (5.6a), and (5.6b) together with (5.6d). Given the vertical velocity component, v, we implement the same discretization scheme to solve for the spanwise velocity component, w. We show these velocity components for a typical α and β in Figure 5.3.

In summary, we have calculated 3D marginal stability curves via Squire's transformation. In addition, we have calculated the eigenvectors along these curves. These curves represent bifurcation points to both 3D oblique and STW, and the eigenvectors at these points provide the starting directions at these bifurcations.

We now consider bifurcations from finite amplitude 2D waves to 3D waves. To calculate the bifurcation points from finite amplitude 2D waves, we study the 3D linear stability of 2D waves. Thus, we consider perturbations of the form

$$\tilde{u}(x, y, z, t) = (U_{PPF} - c)i + \tilde{U}_{2D} + \epsilon e^{\sigma t}\tilde{u}_{3D}(x, y, z), \tag{5.7}$$

where we are in a frame of reference moving with speed c, $U_{PPF} = 1 - y^2$, and $\tilde{U}_{2D}$ is the velocity field of the 2D secondary flow. To study 3D disturbances, we use the vorticity formulation of the 3D Navier-Stokes equations:

$$\frac{\partial \tilde{\omega}}{\partial t} + (\tilde{u} \cdot \nabla)\tilde{\omega} - (\tilde{\omega} \cdot \nabla)\tilde{u} - \frac{1}{Re}\nabla^2\tilde{\omega} = 0, \tag{5.8}$$

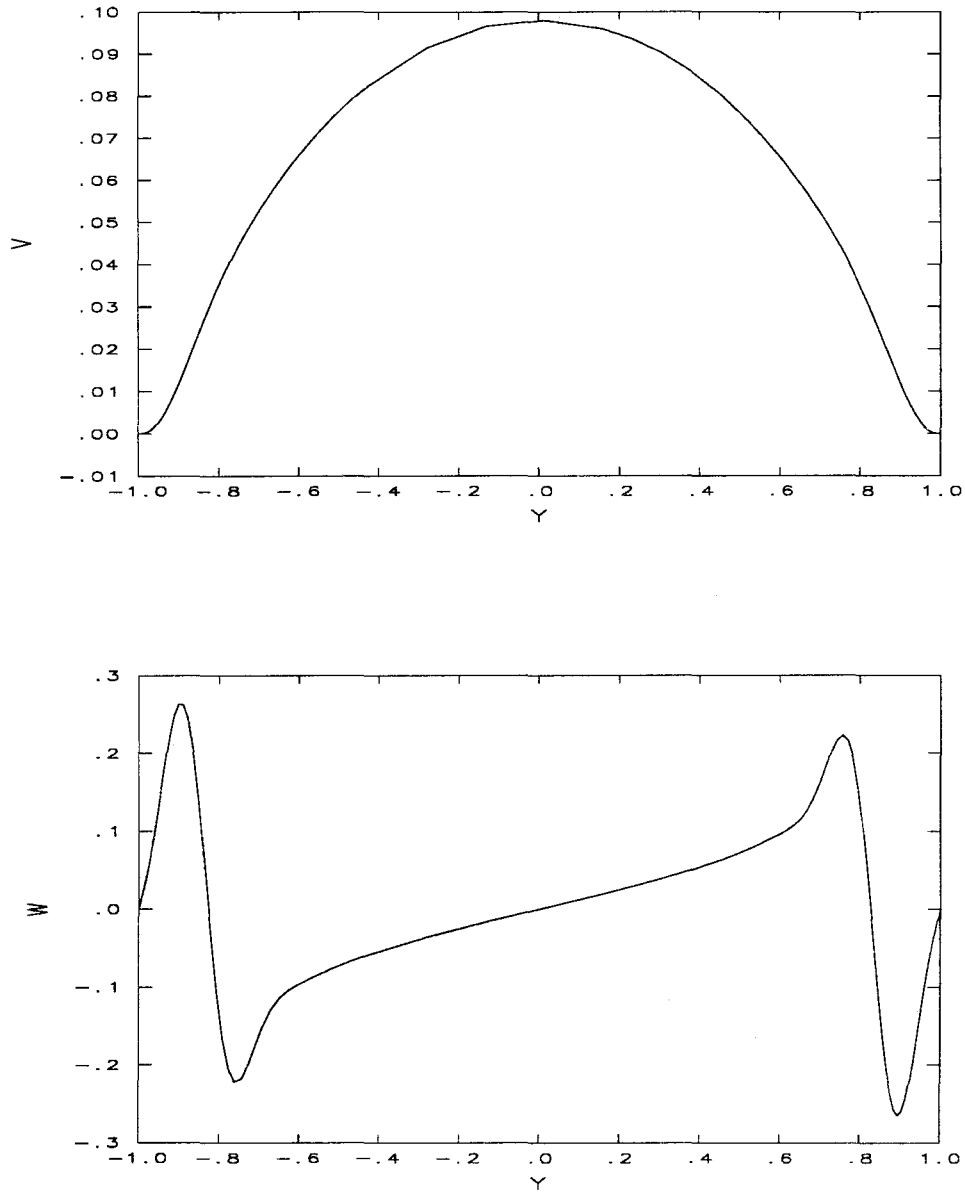where $\tilde{\omega} = \xi\mathbf{i} + \eta\mathbf{j} + \zeta\mathbf{k} = \nabla \times \tilde{u}$.

Figure 5.3. Vertical and spanwise velocity components from linear theory. $\beta = .01, \alpha = 1.02$.

Substituting (5.7) into (5.8) and linearizing, we obtain

$$\frac{1}{Re}\nabla^4 v - (\frac{\partial^2}{\partial x^2} + \frac{\partial^2}{\partial z^2})(Uv_x + uV_x + Vv_y + vV_y)$$

$$+\frac{\partial}{\partial x}((uU_y)_x + Uu_{xy} + Vu_{yy} + U_yv_y + vU_{yy})$$

$$+\frac{\partial}{\partial z}(U_yw_x + Uw_{xy} + V_yw_y + Vw_{yy}) = \sigma\nabla^2 v, \tag{5.9}$$

$$\frac{1}{Re}\nabla^2(u_z - w_x) + \frac{\partial}{\partial x}(Uw_x + Vw_y)$$

$$-\frac{\partial}{\partial z}(Uu_x + uU_x + Vu_y + vU_y) = \sigma(u_z - w_x), \tag{5.10}$$

$$u_x + v_y + w_z = 0, \tag{5.11}$$

where the x and z vorticity equations have been combined into (5.9), (5.10) is the equation for the y vorticity component, $U = U_{2D} + (U_{PPF} - c)$, V is the vertical velocity of the 2D secondary flow, and the Reynolds number is defined by the 2D secondary flow. The no slip boundary conditions are

$$u(\pm 1) = v(\pm 1) = w(\pm 1) = 0. \tag{5.12}$$

We reduce the system of PDE's to ODE's by implementing the following spectral representation for the velocity components:

$$[u, v, w] = e^{i\beta z}\sum_{n=-\infty}^{\infty}[\hat{u}_n, \hat{v}_n, \hat{w}_n]e^{i\alpha n x}. \tag{5.13}$$

Substituting (5.13) into (5.9)–(5.11), we obtain the modal stability equations

$$\frac{1}{Re}((S_x^2 + S_z^2)^2 + 2(S_x^2 + S_z^2)\frac{d^2}{dy^2} + \frac{d^4}{dy^4})v_n$$

$$-(S_x^2 + S_z^2)(U * v_x + u * V_x + V * v_y + v * V_y)$$

$$+S_x((u * U_y)_x + U * u_{xy} + V * u_{yy} + U_y * v_y + v * U_{yy})$$

$$+S_z(U_y * w_x + U * w_{xy} + V_y * w_y + V * w_{yy}) = \sigma(S_x^2 + S_z^2 + \frac{d^2}{dy^2})v_n, \qquad (5.14)$$

$$\frac{1}{Re}(S_x^2 + S_z^2 + \frac{d^2}{dy^2})(S_z u_n - S_x w_n) + S_x(U * w_x + V * w_y)$$

$$-S_z(U * u_x + u * U_x + V * u_y + v * U_y) = \sigma(S_z u_n - S_x w_n), \qquad (5.15)$$

$$S_x u_n + v_{n,y} + S_x w_n = 0, \qquad (5.16)$$

where the hats have been dropped, $S_x = i\alpha n$, $S_z = i\beta$, and $f * g$ is the convolution of the two Fourier series. Note that we are using the spectral representation for the velocity field of the 2D secondary flow. The modal boundary conditions are

$$u_n(\pm 1) = v_n(\pm 1) = w_n(\pm 1) = 0. \qquad (5.17)$$

By use of the continuity equation, w_n can be eliminated from equations (5.14)–(5.15) and it only remains to solve a fourth-order equation for v_n and second-order equation for u_n.

We solve the system of ODE's and boundary conditions by the method of spectral collocation. We set

$$u_n(y) = \sum_{k=0}^{K} a_{nk}\tilde{T}_k(y) \qquad (5.18a)$$

and

$$v_n(y) = \sum_{k=0}^{K} a_{nk}\hat{T}_k(y) \qquad (5.18b)$$

where $\tilde{T}_k(y)$ and $\hat{T}_k(y)$ are modified Chebyshev polynomial. The polynomials are modified to satisfy the boundary conditions identically. For v_n,

$$\tilde{T}_k(y) = (1 - y^2)^2 T_k(y), \tag{5.19}$$

and for u_n

$$\hat{T}_k(y) = (1 - y^2) T_k(y), \tag{5.20}$$

where $T_k(y)$ is the kth Chebyshev polynomial. We evaluate the resulting equations at the maxima of the Kth Chebyshev polynomial and are left to solve a generalized eigenvalue problem of the form

$$G\tilde{a} = \sigma B \tilde{a} \tag{5.21}$$

for the complex eigenvector σ and the complex eigenvector $\tilde{a}$. If one uses the exponential form of the Fourier series, equation (5.13), then the matrices G and B are in general complex. Because the 2D flow is real, a real formulation can be derived by using the triginometric form of the Fourier series. The real formulation reduces the memory requirements of the computation drastically. Because the use of standard generalized eigenvalue solvers led to numerical errors, we inverted the matrix B and solved the regular eigenvalue problem

$$Cx = \sigma x \quad \text{where} \quad C = B^{-1}A. \tag{5.22}$$

The need for inverting the matrix B motivated the modification of the Chebyshev polynomials described by (5.19)–(5.20). The enforcement of the time independent boundary conditions (5.17) on the system would introduce rows of zeros in B and prevent its inversion.

As a check on our formulation, in Table 5.1 we compare our values to those of Herbert and Pugh at a Reynolds number of 5000, $\alpha = 1.12$, and $\beta = 2$. As can be seen from the Table our results are in good agreement with those of Herbert and Pugh.

Table 5.1. Comparison of stability results to Herbert and Pugh.

Eigenvalue	Herbert	Pugh	Present
σ_s	.0487	.0489	.0489
σ_a	.0462	.0462	.0462

The notation of σ_s and σ_a represent symmetric and antisymmetric eigenfunctions. By symmetric and antisymmetric, we mean

$$u_n(-y) = (-1)^n u_n(y) \quad \text{(symmetric)}$$

$$u_n(-y) = (-1)^{n+1} u_n(y) \quad \text{(antisymmetric)}.$$

The 3D stability of 2D waves has been studied extensively by Herbert and Pugh. We limited our calculations to find a very specific result. Rozhdestventsky and Simakin, in a time dependent calculation, found stable steady states by perturbing 2D waves with a small 3D perturbation. In particular, they perturbed the velocity field given by the 2D secondary flow at a Re_P of 5000 and $\alpha = 1.25$. The 3D perturbation had a spanwise wave number, β, of 2. With these initial conditions, they found that the flow reached a steady state. The constant flux Reynolds number for the 3D state corresponding to this point is $Re_Q = 2100$. By perturbing the 3D steady states, they were able to find other steady states down to a constant flux Reynolds number of 1313. In hope of confirming their results, we searched for bifurcations from the

2D states at $\alpha = 1.25$ and $\beta = 2$. We found such a bifurcation on the upper branch at $Re_P = 6000$. In section 5.5, we will show that the nonlinear 3D solution branch which emanates from that bifurcation does not extend below the critical 2D wave Reynolds number.

In summary, we have calculated the bifurcation points from 3D Orr-Sommerfeld curves to both oblique and STW 3D waves. In addition, we have found a bifurcation corresponding to the data given by Rozhdestvensky and Simakin. In the next section, we formulate the method used to calculate the solution branches which emanate from these bifurcations.

5.3 Problem Formulation for 3D Oblique and STW

Consider the vorticity formulation for the 3D incompressible Navier-Stokes equations:

$$\frac{\partial \tilde{\omega}}{\partial t} + (\tilde{u} \cdot \nabla)\tilde{\omega} = (\tilde{\omega} \cdot \nabla)\tilde{u} + \nu \nabla^2 \tilde{\omega} \tag{5.23}$$

$$\nabla \cdot \tilde{u} = 0, \tag{5.24}$$

where $\omega = \nabla \times \tilde{u} = \xi \mathbf{i} + \eta \mathbf{j} + \zeta \mathbf{k}$. Looking for steady travelling waves, we set $\tilde{u}(x, y, z, t) = \tilde{u}(x - ct, y, z)$. Letting $x = x - ct$ and nondimensionalizing by the centerline velocity U_0 and the channel half width h, (5.23)–(5.24) become

$$-c\frac{\partial \tilde{\omega}}{\partial x} + (\tilde{u} \cdot \nabla)\tilde{\omega} = (\tilde{\omega} \cdot \nabla)\tilde{u} + \frac{1}{Re}\nabla^2 \tilde{\omega}. \tag{5.25}$$

If we let $\tilde{u}(x, y, z) = U + \tilde{u}_{3D}(x, y, z)$, equation (5.25) becomes

$$-\frac{1}{Re}\nabla^2 \tilde{\omega} + \{(U - c)\frac{\partial}{\partial x} + (\tilde{u} \cdot \nabla)\}(\Omega k + \tilde{\omega})$$

$$-((\tilde{\omega} \cdot \nabla) + \Omega\frac{\partial}{\partial z})((U - c)\mathbf{i} + \tilde{u}) = 0, \tag{5.26}$$

where the $3D$ subscript has been dropped and $\Omega = -\frac{dU}{dy}$ is the z vorticity component of the plane Poiseuille flow. Expanding (5.26) and subtracting the x derivative of the z vorticity equation from the z derivative of the x equation gives

$$\frac{1}{Re}\nabla^4 v - (U-c)\frac{\partial}{\partial x}\nabla^2 v - \frac{d\Omega}{dy}\frac{\partial v}{\partial x}$$

$$+\frac{\partial}{\partial z}((\tilde{u}\cdot\nabla)\xi - (\tilde{\omega}\cdot\nabla)u) - \frac{\partial}{\partial x}((\tilde{u}\cdot\nabla)\zeta - (\tilde{\omega}\cdot\nabla)w) = 0 \qquad (5.27)$$

$$-\frac{1}{Re}\nabla^2\eta + (U-c)\frac{\partial\eta}{\partial x} - \Omega\frac{\partial v}{\partial x} + (\tilde{u}\cdot\nabla)\eta - (\tilde{\omega}\cdot\nabla)v = 0 \qquad (5.28)$$

$$\nabla\cdot\tilde{u} = 0. \qquad (5.29)$$

To search for waves which are periodic in an oblique direction, we let

$$u(x,y,z) = \sum_{n=-\infty}^{\infty} \hat{u}_n(y)e^{in(\alpha x+\beta z)}. \qquad (5.30)$$

Substituting (5.30) into (5.27)–(5.29), we derive the following modal equations for each n:

$$\frac{1}{Re}\{(i\alpha n)^2 + (i\beta n)^2 + 2((i\alpha n)^2 + (i\beta n)^2)\frac{d^2}{dy^2} + \frac{d^4}{dy^4}\}v_n$$

$$-(U-c)i\alpha n((i\alpha n)^2 + (i\beta n)^2 + \frac{d^2}{dy^2})v_n - \frac{d\Omega}{dy}(i\alpha n)v_n$$

$$+i\beta n\{(u*\xi_x + v*\frac{d\xi}{dy} + w*\xi_z) - (\xi*u_x + \eta*\frac{du}{dy} + \zeta*u_z)\}$$

$$-i\alpha n\{(u*\zeta_x + v*\frac{d\zeta}{dy} + w*\zeta_z) - (\xi*w_x + \eta*\frac{dw}{dy} + \zeta*w_z)\} = 0 \qquad (5.31)$$

$$-\frac{1}{Re}((i\alpha n)^2 + (i\beta n)^2 + \frac{d^2}{dy^2})\eta_n + (U-c)i\alpha n\eta_n - \Omega(i\beta n)v_n$$

$$+(u*\eta_x + v*\frac{d\eta}{dy} + w*\eta_z) - (\xi*v_x + \eta*\frac{dv}{dy} + \zeta*v_z) = 0 \qquad (5.32)$$

$$i\alpha n u_n + \frac{dv_n}{dy} + i\beta n w_n = 0, \qquad (5.33)$$

where we have dropped the hats and $f * g$ is the convolution of the two Fourier series.

Applying the no slip boundary conditions at the walls, we have

$$u_n(\pm 1) = 0$$

$$v_n(\pm 1) = 0 \tag{5.34}$$

$$w_n(\pm 1) = 0.$$

In addition, the following reality condition can be imposed:

$$u_{-n} = u_n^*. \tag{5.35}$$

This relation implies that we need only solve for the modes $n \geq 0$.

For $n = 0$, (5.33) implies that $\frac{dv_0}{dy}$ is identically zero. As v_0 is zero at $y = \pm 1$, v_0 is identically zero. In addition, (5.31) and (5.32) are trivially true, and we must return to the z and x vorticity equations. The $n = 0$ component of the x and z vorticity equations are

$$\frac{1}{Re} \frac{d^3 u_0}{dy^3} + \left(u * \zeta_x + v * \frac{d\zeta}{dy} + w * \zeta_z \right) - \left(\xi * w_x + \eta * \frac{dw}{dy} + \zeta * w_z \right) = 0 \tag{5.36}$$

$$\frac{1}{Re} \frac{d^3 w_0}{dy^3} - \left(u * \xi_x + v * \frac{d\xi}{dy} + w * \xi_z \right) + \left(\xi * u_x + \eta * \frac{du}{dy} + \zeta * u_z \right) = 0. \tag{5.37}$$

The corresponding boundary conditions are

$$u_0(\pm 1) = 0$$

$$w_0(\pm 1) = 0. \tag{5.38}$$

Two additional boundary conditions must be provided for (5.36)–(5.37). As in the case of 2D waves, the missing boundary conditions can be obtained by fixing the parametrization of the problem. One possible parametrization is to define the

centerline velocity U_0 such that the average flux in the oblique direction is constant. To take the average flux in the oblique direction, we use the transformation (5.5) introduced earlier. Then the average flux Q (in dimensional variables) in the oblique direction is

$$\frac{\tilde{\alpha}}{2\pi} \int_0^{\frac{2\pi}{\tilde{\alpha}}} \int_{-h}^{+h} (U + \tilde{u}_0) \, dy \, d\tilde{x}. \tag{5.39}$$

We exclude perturbations to the flux by requiring

$$\int_{-h}^{+h} \tilde{u}_0 \, dy = 0. \tag{5.40}$$

Nondimensionalizing (5.40) and converting to regular coordinates, we arrive at

$$\alpha \int_{-1}^{+1} u_0 \, dy = \beta \int_{-1}^{+1} w_0 \, dy. \tag{5.41}$$

Equation (5.41) gives the two missing boundary conditions for (5.36) and (5.37).

Alternatively, as in the case of 2D waves, one could define U_0 by specifying that the average pressure gradient in the oblique direction is constant. As discussed in the previous chapters, the two different parametrizations define two different Reynolds numbers.

To search for waves which are travelling in the streamwise direction and standing in the spanwise direction we let

$$u(x, y, z) = \sum_{m=-\infty}^{+\infty} \sum_{n=-\infty}^{+\infty} \hat{u}_{mn} e^{i\alpha n x} e^{i\beta m z}. \tag{5.42}$$

Substituting (5.42) into (5.27)–(5.29), we derive the following modal equations for each mn:

$$\frac{1}{Re}\{(i\alpha n)^2 + (i\beta m)^2 + 2((i\alpha n)^2 + (i\beta m)^2)\frac{d^2}{dy^2} + \frac{d^4}{dy^4}\}v_{mn}$$

$$-(U-c)i\alpha n((i\alpha n)^2 + (i\beta m)^2 + \frac{d^2}{dy^2})v_{mn} - \frac{d\Omega}{dy}(i\alpha n)v_{mn}$$

$$+i\beta m\{(u * \xi_x + v * \frac{d\xi}{dy} + w * \xi_z) - (\xi * u_x + \eta * \frac{du}{dy} + \zeta * u_z)\}$$

$$-i\alpha n\{(u * \zeta_x + v * \frac{d\zeta}{dy} + w * \zeta_z) - (\xi * w_x + \eta * \frac{dw}{dy} + \zeta * w_z)\} = 0 \qquad (5.43)$$

$$-\frac{1}{Re}((i\alpha n)^2 + (i\beta m)^2 + \frac{d^2}{dy^2})\eta_{mn} + (U-c)i\alpha n\eta_n - \Omega(i\beta m)v_{mn}$$

$$+(u * \eta_x + v * \frac{d\eta}{dy} + w * \eta_z) - (\xi * v_x + \eta * \frac{dv}{dy} + \zeta * v_z) = 0 \qquad (5.44)$$

$$i\alpha n u_{mn} + \frac{dv_{mn}}{dy} + i\beta m w_{mn} = 0, \qquad (5.45)$$

where we have dropped the hats and $f * g$ is the convolution of the two Fourier series. Applying the no slip boundary conditions at the walls, we have

$$u_{mn}(\pm 1) = 0$$

$$v_{mn}(\pm 1) = 0 \qquad (5.46)$$

$$w_{mn}(\pm 1) = 0.$$

In addition, the following reality condition can be imposed:

$$u_{-mn} = u_{mn}^*. \qquad (5.47)$$

This relation implies that we need only solve for the modes $m \geq 0$ for all n.

In addition, we restrict our study to solutions with the reflectional symmetry

$$(u(-z), v(-z), w(-z)) = (u(z), v(z), -w(z))$$

which corresponds to the modal relations

$$(u_{-mn}, v_{-mn}, w_{-mn}) = (u_{mn}, v_{mn}, -w_{mn}). \tag{5.48}$$

This reflectional symmetry is consistent with the experimental observations by Nishioka (1978) of counter rotating longitudinal vortices.

The reality condition together with (5.48) imply that we need only solve for the modes $m \geq 0, n \geq 0$.

For $m = 0, n \geq 0$, (5.48) implies that w_{0n} is identically zero. Therefore we need only solve for v_{0n} and use the continuity equation to compute u_{0n}. If $m = n = 0$, the continuity equation implies that v_{00} is identically zero. In addition, equations (5.43)–(5.44) are identically zero and we must solve the z vorticity equation. The z vorticity equation in modal form is

$$\frac{1}{Re}\frac{d^3 u_0}{dy^3} + (u * \zeta_x + v * \frac{d\zeta}{dy} + w * \zeta_z) - (\xi * w_x + \eta * \frac{dw}{dy} + \zeta * w_z) = 0, \tag{5.49}$$

with boundary conditions

$$u_{00}(\pm 1) = 0. \tag{5.50}$$

One additional boundary condition must be given. Once again, the additional boundary condition is needed to fix the parametrization of the Reynolds number. We chose to define the Reynolds number so that the average flux is constant. This boundary condition is

$$\int_{-1}^{+1} u_{00} \, dy = 0. \tag{5.51}$$

5.4 Numerical Method

To solve the system of ODE's and boundary conditions for the oblique waves and the STW, we first introduce the following additional equations.

As in the case of the 2D waves, there is an arbitrary phase shift in the x direction for the STW. In general, there would also be an arbitrary phase shift

in the z direction. However, we have ruled out this phase shift by imposing the reflectional symmetry described by (5.48). To eliminate the phase shift in the x direction, we set

$$\frac{\Im(u_{11}(-1))}{\Re(u_{11}(-1))} = \text{constant}. \tag{5.52}$$

For the oblique waves, there is an arbitrary phase shift in the oblique direction. We eliminated this phase shift by setting

$$\frac{\Im(u_1(-1))}{\Re(u_1(-1))} = \text{constant}. \tag{5.53}$$

To continue into the nonlinear regime, it is convenient to define a nonlinear amplitude. We chose to define an amplitude based on the disturbance energy. For oblique waves, we set

$$A_E^2 = \frac{15}{16} \sum_{n=-N}^{n=+N'} \int_{-1}^{+1} |u_n(y)|^2 + |v_n(y)|^2 + |w_n(y)|^2 \, dy, \tag{5.54}$$

where the prime denotes that the zero mode is not included and the $\frac{15}{16}$ is chosen so that the energy of the basic flow is normalized to one. For STW, we set

$$A_E^2 = \frac{15}{16} \sum_{m=-M}^{m=+M'} \sum_{n=-N}^{n=+N} \int_{-1}^{+1} |u_{mn}(y)|^2 + |v_{mn}(y)|^2 + |w_{mn}(y)|^2 \, dy. \tag{5.55}$$

To solve the system of ODE's with appropriate boundary conditions and auxiliary equations, we implement the same discretization method that was used for the 2D waves and quasi-periodic solutions. This discretization results in a nonlinear algebraic system which was solved locally by Newton's method and continued by pseudo-arclength continuation.

5.5 Results

We first consider bifurcations from plane Poiseuille flow. In Figures 5.4–5.7, we plot amplitude versus Reynolds number for STW. The curves plotted correspond to

$\alpha = 1.02$ and $\alpha = 1.09$ on the Orr-Sommerfeld curve for different values of β. The calculations shown were computed with $N = 1$ modes in x and $M = 2$ modes in z. This resolution was found to be sufficient for qualitatively correct results. All the branches shown were computed with a Reynolds number based on constant flux.

For small amplitudes, we compared our results to Bridges (1988) to ensure correct criticality of the bifurcation. We determined that one mode in z is insufficient to obtain correct results. This is to be expected since the first nonlinear interaction involves a correction to the mean flow and the generation of a second harmonic. However, this is in contrast to 2D waves where one mode in x gives qualitatively correct results.

As can be seen from the Figures, we found that no branch extended below the critical Reynolds number of the 2D waves. In particular, we examined the branches that Bridges suggests may extend to low Reynolds number, $\beta > .365$. As shown in Figures 5.6 and 5.7, for $\beta > .365$ the Reynolds number reaches a limit point above the 2D wave critical Reynolds number of 2600.

For each value of β we found a neutral surface that is qualitatively similar to the 2D wave neutral surface. As in the case of the 2D waves, solution branches exist at higher streamwise wave numbers than on the marginal stability curve. There are also marginal stability surfaces at higher spanwise wave numbers than can be obtained from Squire's transformation. However, the major result is valid for all these marginal stability surfaces, i.e., the critical Reynolds number does not extend below the critical Reynolds number of the 2D waves.

In Figures 5.8–5.11, we present typical branches of oblique waves at the parameter values mentioned above. In contrast to the STW, one mode is sufficient to obtain qualitatively correct results. The Figures shown were for $N = 2$ modes. As in the STW, no low Reynolds number solutions were found. In contrast, the

influence of the spanwise wave number is to stabilize the flow. Bridges conjectured, based on local results, that the solution branches of STW for $\beta > .365$ extend to lower Reynolds number than the oblique waves. However, as can be seen from Figures 5.6 and 5.10, we found the opposite to be true. The nonlinear neutral surfaces are qualitatively similar to the surfaces found in the STW.

Our next calculations were implemented in an attempt to confirm the results found by Rozhdestvensky and Simakin. In Figure 5.12, we show the nonlinear branches which bifurcate from 2D waves for $\beta = 2.0$ and $\alpha = 1.25, 1.26$ and $\alpha = 1.28$. For these branches, as shown in the Figures, the Reynolds number first decreases, passes through a limit point, and then increases. We searched by continuation at various values of spanwise and streamwise wave numbers and found no low Reynolds number solutions.

Although we can not rule out the existence of isolated branches, we can state that there are no 3D branches which bifurcate from 2D waves and extend to low Reynolds number at the wave numbers examined.
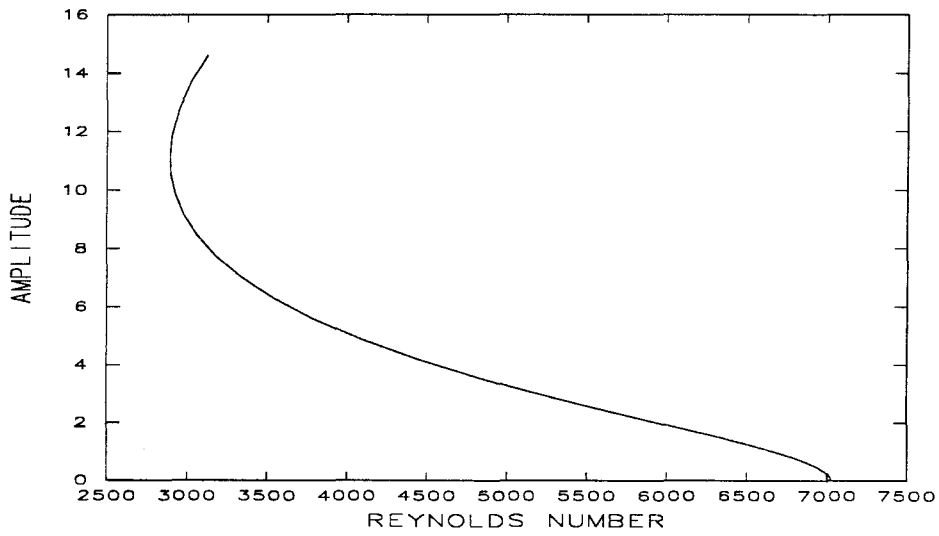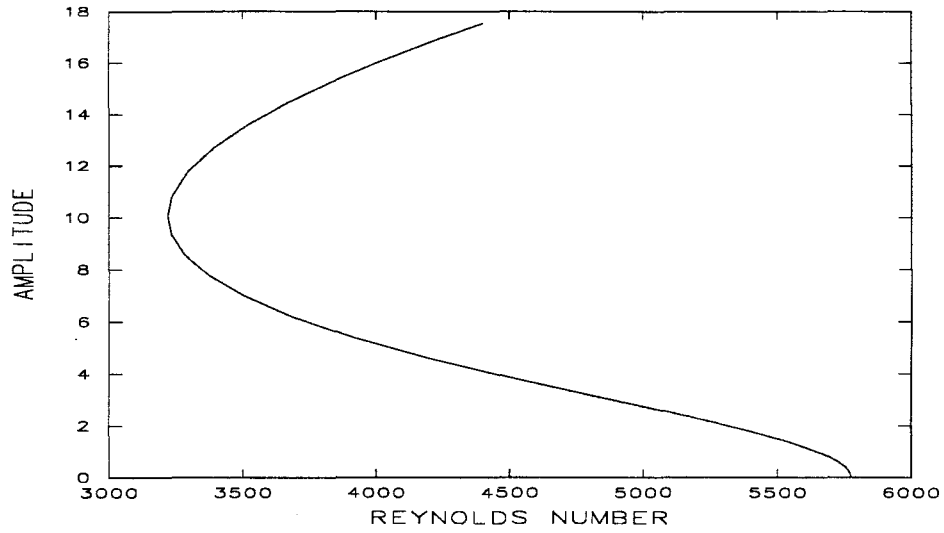
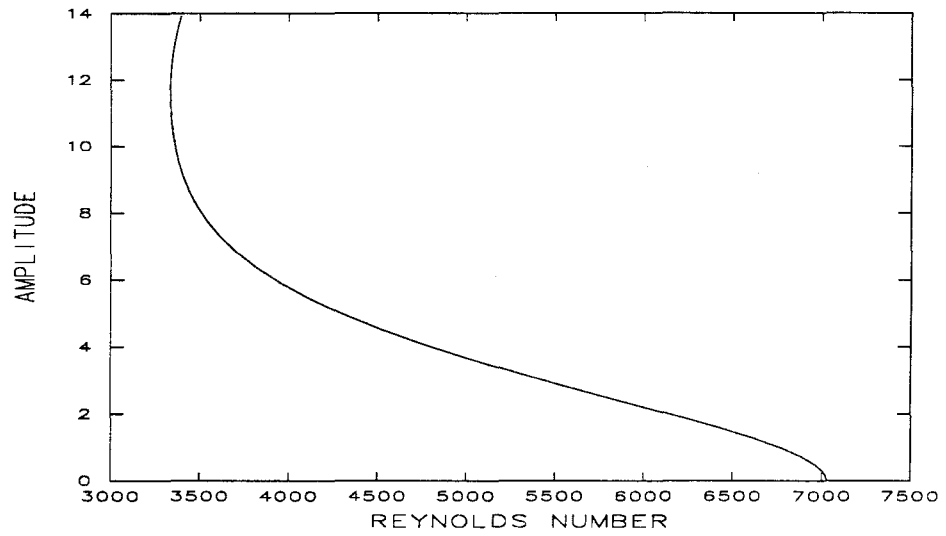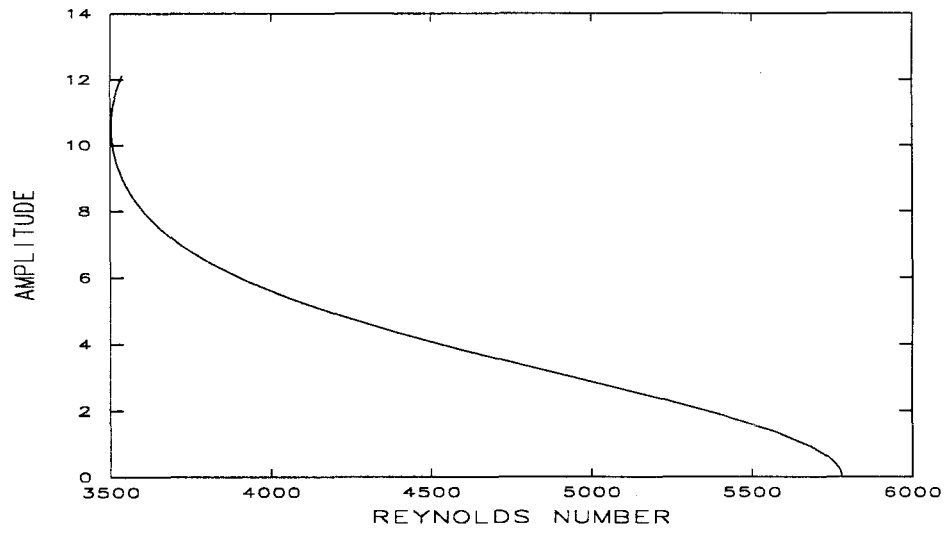Figure 5.4. Bifurcation diagrams for STW. $\beta = .01, \alpha = 1.02$ (top), $\alpha = 1.09$ (bottom).

Figure 5.5. Bifurcation diagrams for STW. $\beta = .05, \alpha = 1.01$ (top), $\alpha = 1.08$ (bottom).
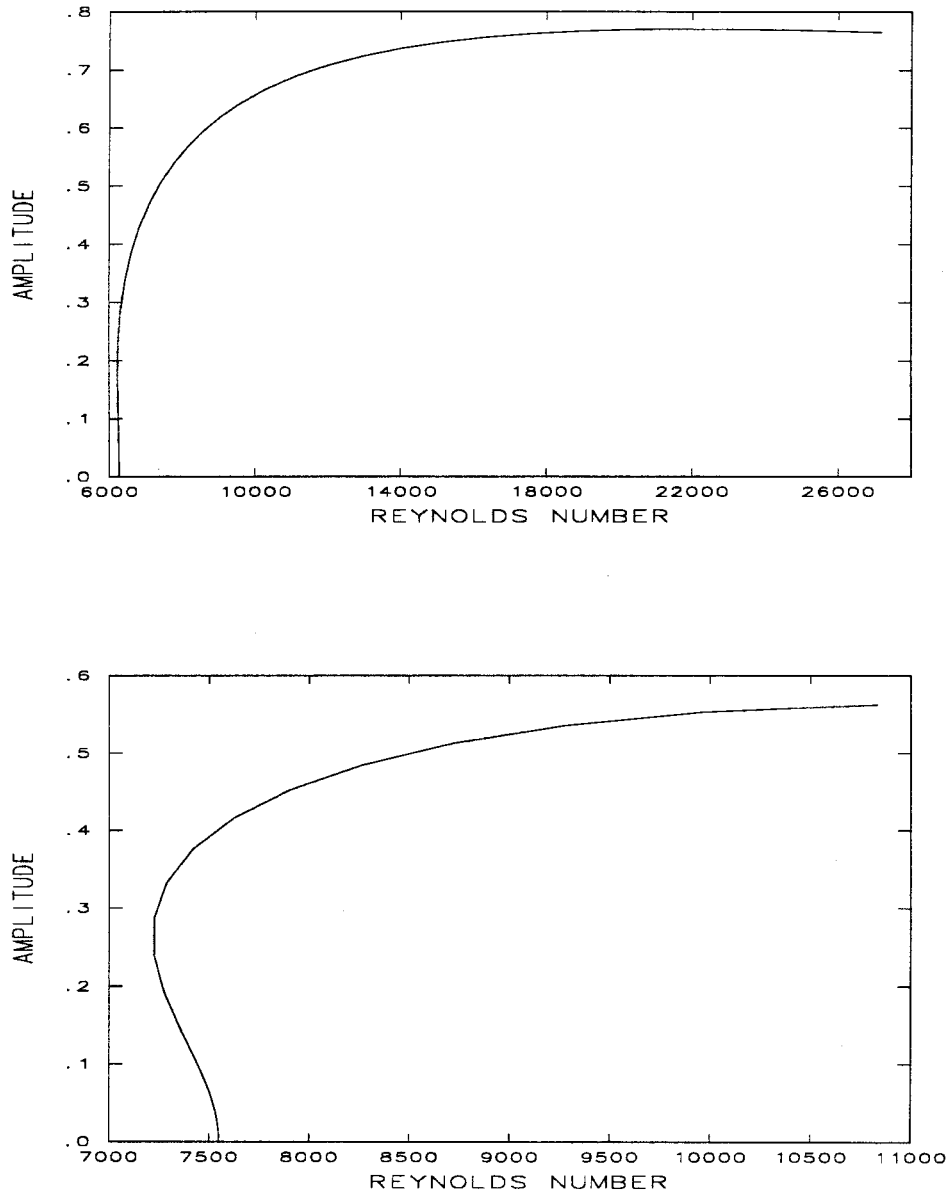
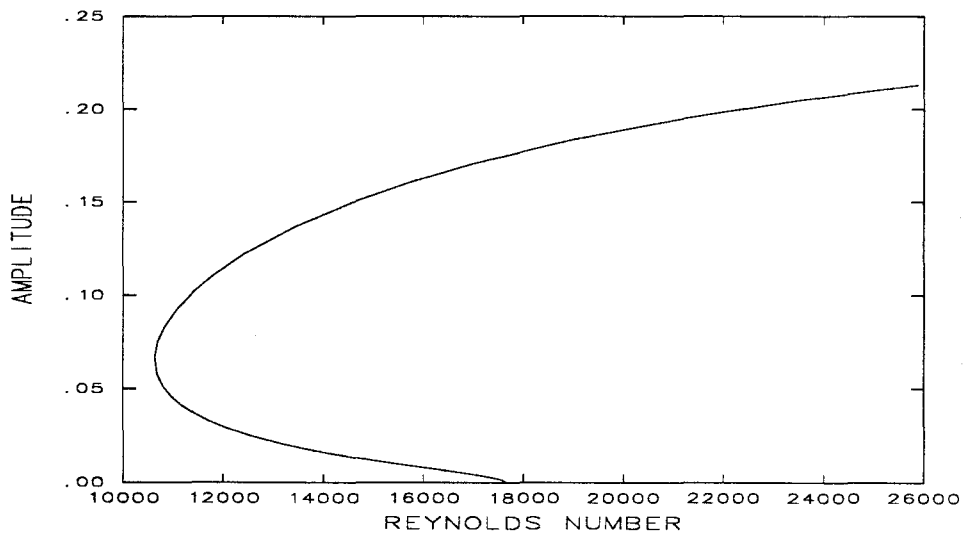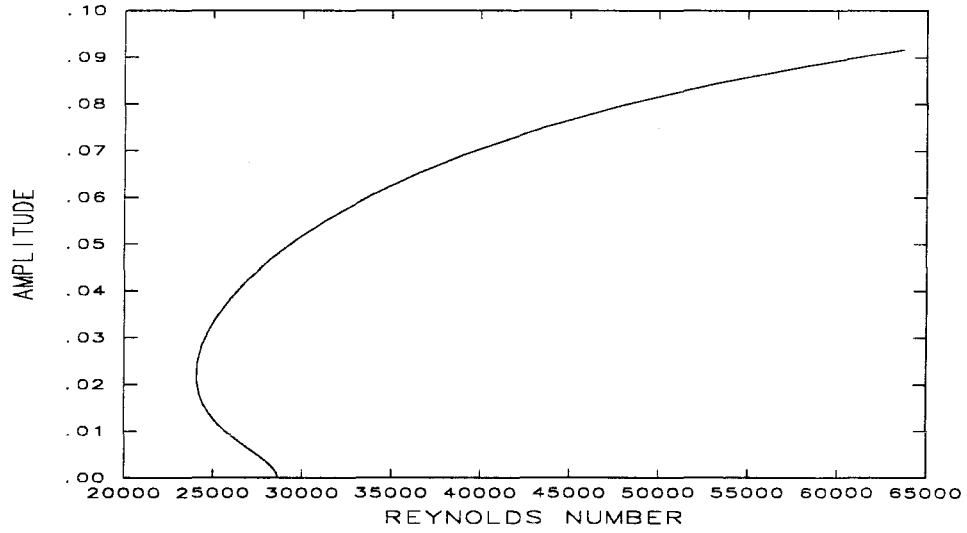Figure 5.6. Bifurcation diagrams for STW. $\beta = .4, \alpha = .938$ (top), $\alpha = 1.014$ (bottom).

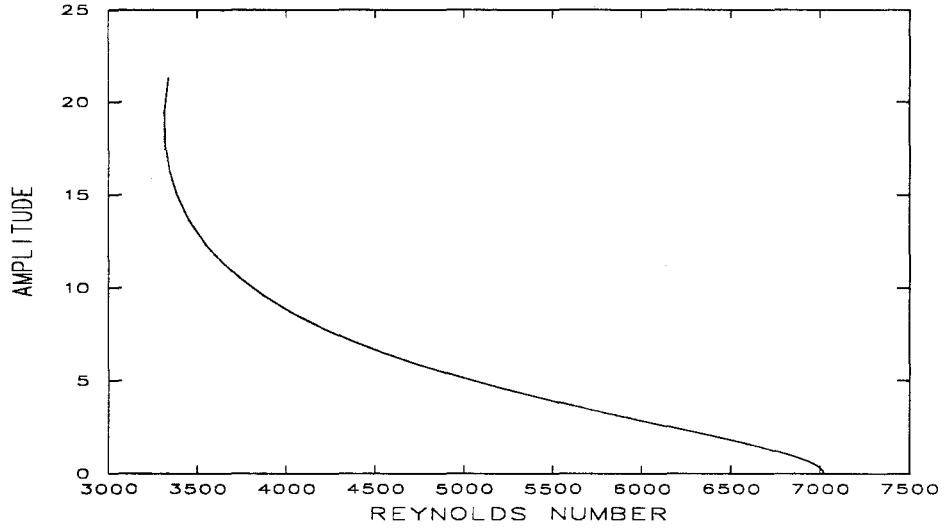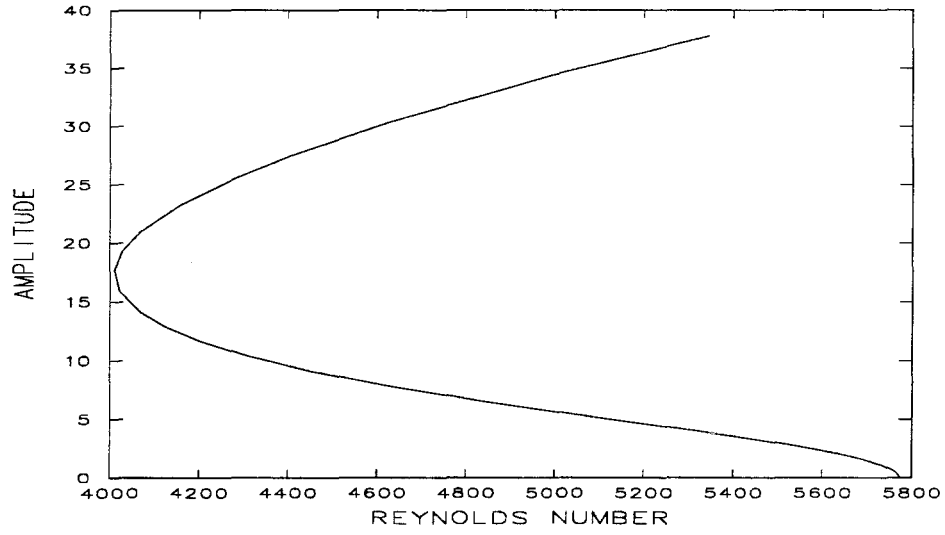Figure 5.7. Bifurcation diagrams for STW. $\beta = 1., \alpha = .216$ (top), $\alpha = .434$ (bottom).

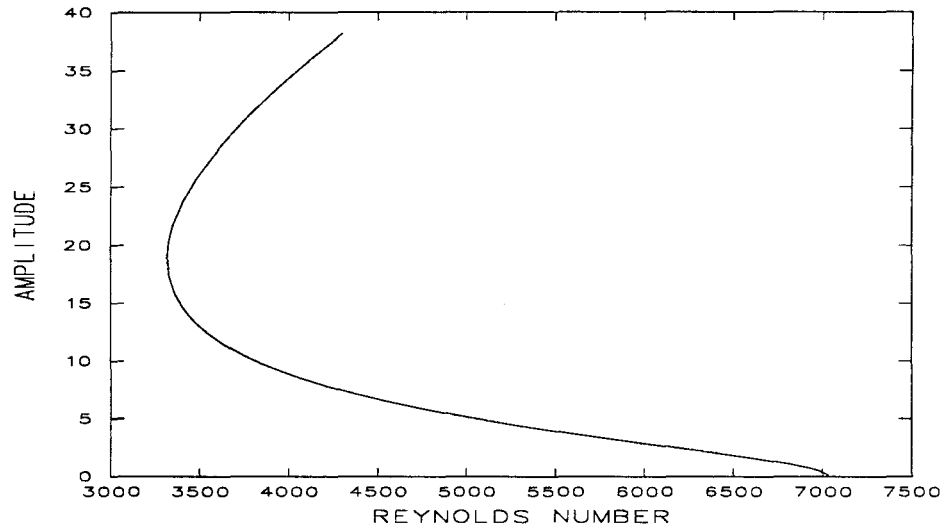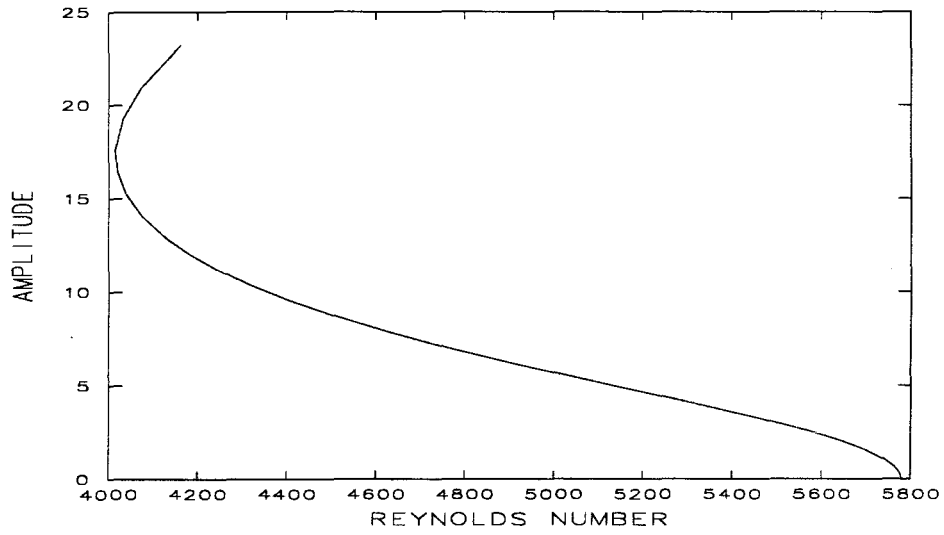Figure 5.8. Bifurcation diagrams for oblique waves. $\beta = .01, \alpha = 1.02$ (top), $\alpha = 1.09$ (bottom).

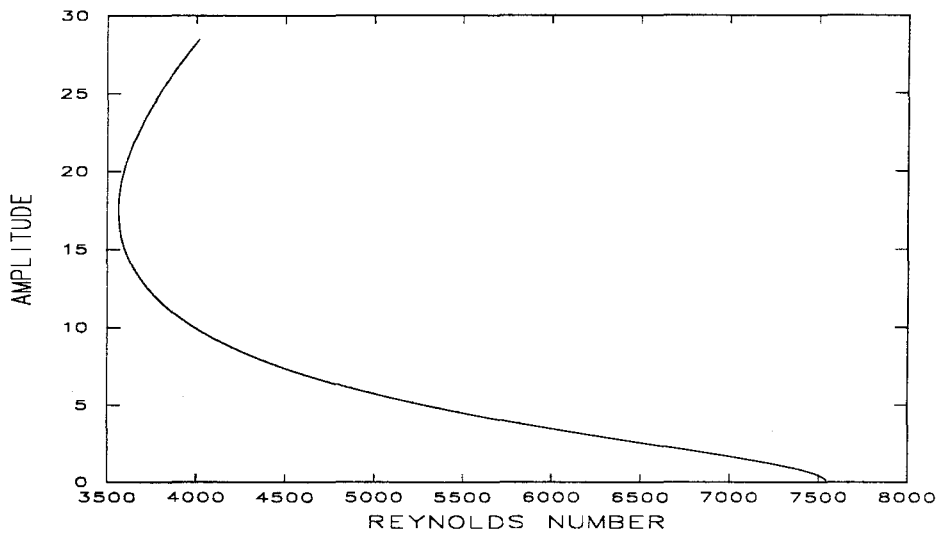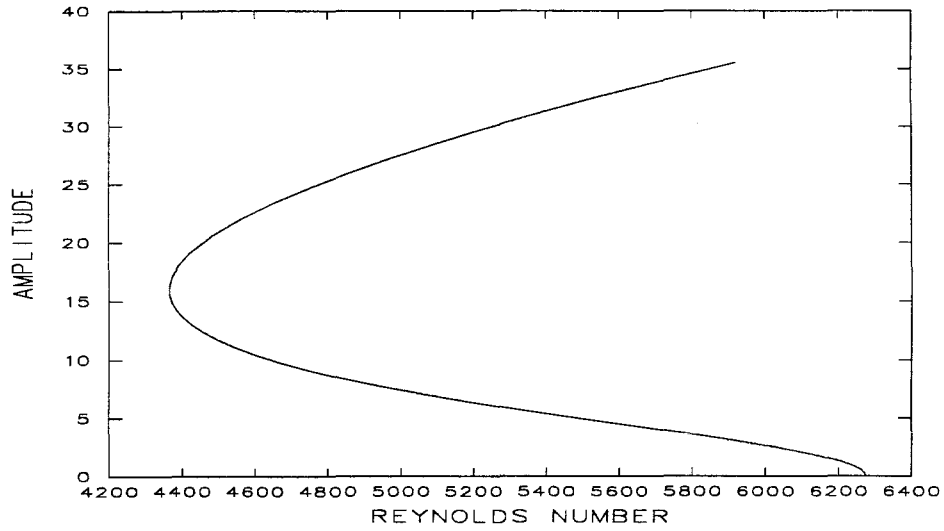Figure 5.9. Bifurcation diagrams for oblique waves. $\beta = .05, \alpha = 1.01$ (top), $\alpha = 1.08$ (bottom).

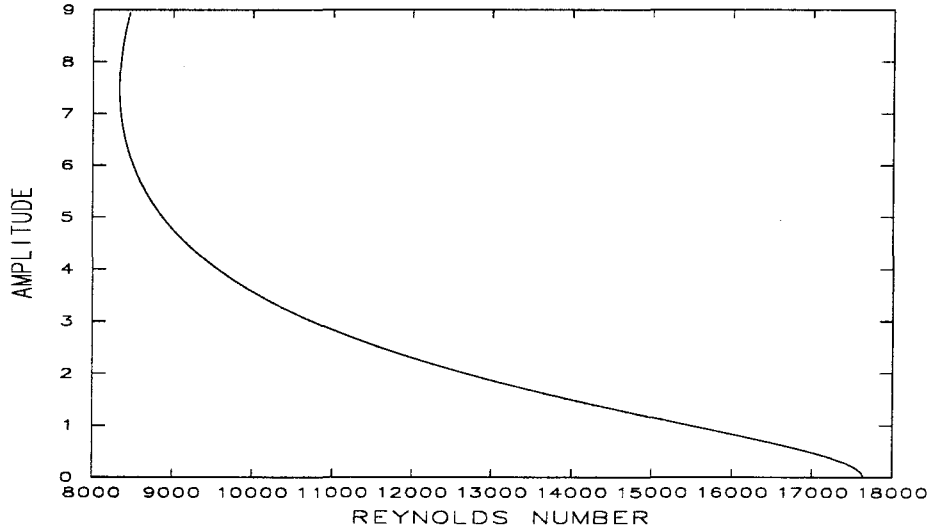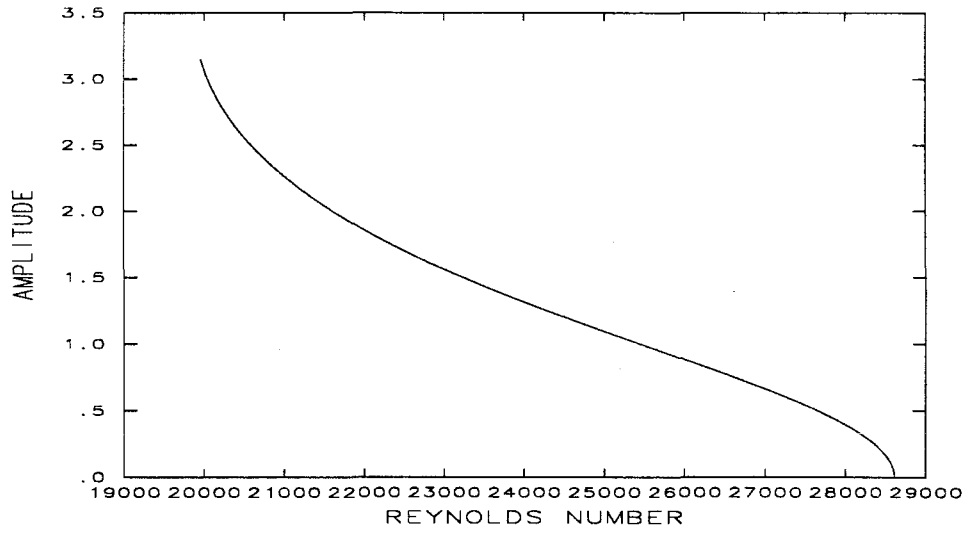Figure 5.10. Bifurcation diagrams for oblique waves. $\beta = .4, \alpha = .938$ (top), $\alpha = 1.014$ (bottom).

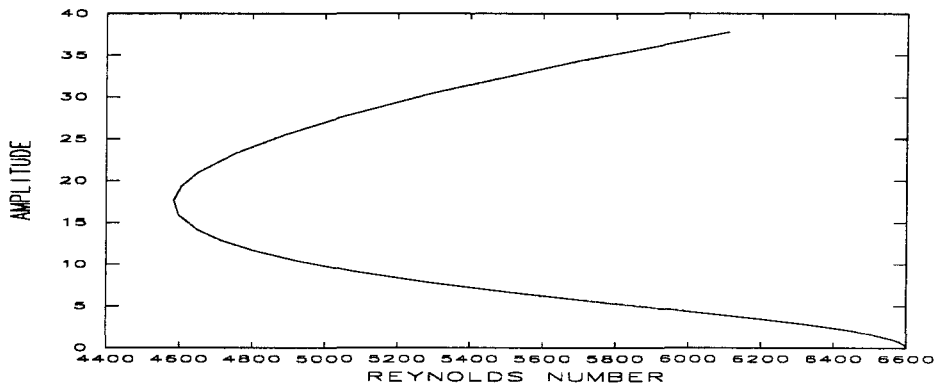Figure 5.11. Bifurcation diagrams for oblique waves. $\beta = 1., \alpha = .213$ (top), $\alpha = .434$ (bottom).
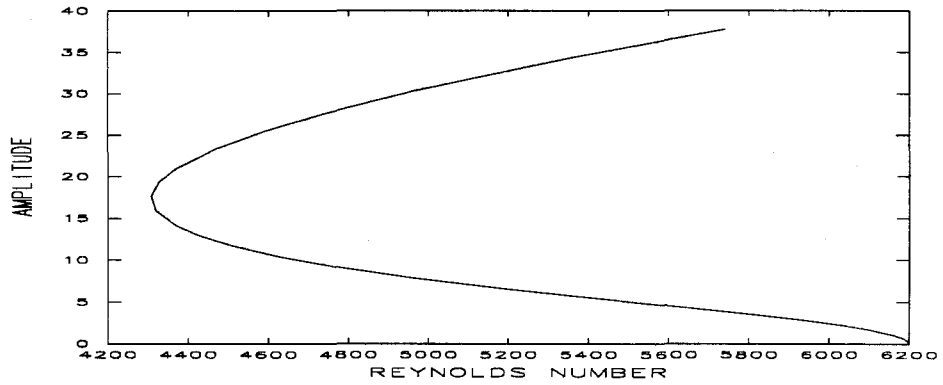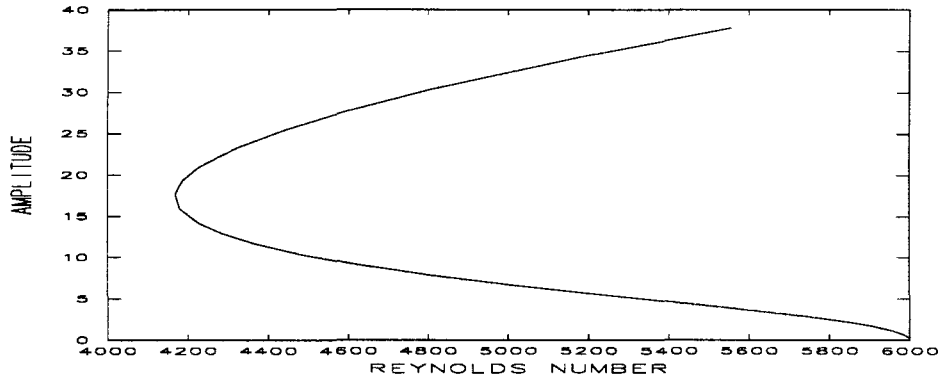
Figure 5.12. Bifurcations from 2D waves. $\beta = 2., \alpha = 1.25, 1.26, 1.28.$

CHAPTER 6

CONCLUSIONS

In summary, we have computed branches of 3D STW and oblique waves which bifurcate from plane Poiseuille flow. In addition, we have calculated branches of STW which bifurcate from 2D waves. These calculations were motivated by the results of Bridges (1988) and Rozdhestvensky and Simakin (1984). Our main result is that these solution branches do not exist at low Reynolds number, i.e., $Re < 2600$.

In Chapter 4, we computed several branches of quasi-periodic solutions which bifurcate from 2D waves. Again, these branches do not extend to low Reynolds number.

It is disappointing that we have been unable to verify Saffman's hypothesis (1983) that vortical solutions should exist at low Reynolds number. However we can not rule out that other solution forms will confirm this hypothesis.

To this effect, Landman (1986) has found several different solutions to the Ginzburg-Landau equation.

The Ginzburg-Landau equation is an amplitude equation which describes the weakly nonlinear evolution of disturbances in plane Poiseuille flow. Landman analyzed quasi-steady solutions to this equation. Among the many solutions he found are solitary waves and other transition type solutions. The existence of these solutions for the Ginzburg-Landau equations suggests that they may exist for the Navier-Stokes equations.

Another hopeful direction is based on the work of Jimenez (1988) who has found period-quadrupling bifurcations with his time dependent formulation. In addition,

there is evidence that solitons (Fokas, 1988) may exist for the 3D Ginzburg-Landau equation.

Because we are interested in unstable solutions, we would hope to apply the methods outlined in this thesis to calculate the solutions described above. The resolution required, however, to model solutions such as the period-quadrupling bifurcation detected by Jimenez would appear to rule out such an approach. A recent method developed by Tuckerman (1988) may be useful to this end. Tuckerman has showed that a time-dependent code can be easily modified to compute unstable and stable steady states. One nice feature of this formulation is the savings in memory and thus the possbility of increasing resolution and the modelling of more complicated solutions.

We hope in future investigations to implement the approach outlined by Tuckerman and study the solutions found by Landman and the other authors.

References

Alavyoon, F., Henningson, D.S. and Alfresson, P.H. (1986) Turbulent spots in plane Poiseuille flow-flow visualization. *Phys. Fluids* **29** (4), 1328–1331.

Bridges, T.J. (1988) The Hopf bifurcation with symmetry for the Navier-Stokes equations in $(L_p(\Omega))^n$, with application to plane Poiseuille flow. *Arch. Rat. Mech. Anal.* (to appear).

Carlson, D.R. Widnall, S.E. and Peeters, M.F. (1982) A flow-visualization study of transition in Plane Poiseuille flow. *JFM* **121** 487–505.

Chen, T.S. and Joseph, D.D. (1973) Subcritical bifurcation of plane Poiseuille flow. *JFM* **58** 337–351.

Davey, A., Hocking, L.M., Stewartson, K. (1974) On the nonlinear evolution of three-dimensional disturbances in plane Poiseuille flow. *JFM* **63**, 529–536.

Doedel and E.J., Kernevez, J.D. (1985) Software for continuation and bifurcation problems. *Applied Math. Tech. Rep.*, Caltech.

Drazin, P.G. and Reid, W.H. (1981) *Hydrodynamic Stability.* Cambridge Univ. Press.

Goldshtik, M.A., Lifshits, A.M. and Shtern, V.N. (1983) The transition Reynolds number for a plane channel. *Akademiia Nauk SSSR, Doklady,* **273** (1), 75–79.

Guckenheimer and J., Holmes, P. (1983) *Nonlinear oscillations, dynamical systems, and bifurcations of vector fields.* Springer-Verlag.

Herbert, Th. (1977) Periodic secondary motions in a plane channel. *Springer Lecture Notes in Physics* **59** 235.

Herbert, Th. (1983) Modes of secondary instability in Plane Poiseuille Flow. *Proceedings of the IUTAM Symposium on Turbulence and Chaotic Phenomena in Fluids* September 1983.

Jimenez, J. (1987) Bifurcation and bursting in two-dimensional Poiseuille flow. *Phys. Fluids* **30** (12), 3644–3646.

Keller, H.B. (1977) Numerical Solution of Bifurcation and Nonlinear Eigenvalue Problems. *Applications of Bifurcation Theory* Academic Press Inc.

Keller, H.B. (1988) *Numerical methods in bifurcation problems.* Springer-Verlag.

Kim, J. (1983) On the structure of wall-bounded turbulent flows. *Phys. Fluids* **26** (8), 2088–2097.

Kleiser, L. (1982) Spectral simulations in laminar-turbulent transition in plane Poiseuille flow and comparison with experiments. *Proc. 8th Intl Conf. on Numerical Methods in Fluid Dynamics, Aachen* (ed. E. Krause) , Springer Lecture Notes in Physics **170** 280.

Krist, S.E. and Zang, T.A. (1987) Numerical simulation of channel flow transition: Resolution requirements and structure of hairpin vortex. *NASA technical paper* **2667**.

Landman, M.J. (1987) Solutions of the Ginzburg-Landau equation of interest in shear flow transition. *Studies in Applied Math.* **76**, 187-237.

Meksyn, D. and Stuart, J.T. (1951) Stability of viscous motion between parallel surfaces for finite disturbances. *Proc. Roy. Soc. A* **208**, 517–526.

Milinazzo, F.A. and Saffman, P.G. (1985) Finite-amplitude waves in plane viscous shear flows. *JFM* **160**, 281–295

Nishioka, M. and Asai, M. (1985) Some observations of the subcritical transition in plane Poiseuille flow. *JFM* **150**, 441-450.

Noether, F. (1921) Das Turbulenzproblem. *ZAMM* **1**, 125–138, 218–219.

Orszag, S.A, (1971) Accurate solution of the Orr-Sommerfeld stability equation. *JFM* **50**, 689–703.

Orszag, S.A. and Gottlieb, D. (1977) *Numerical Analysis of Spectral Methods: Theory and Applications*. Society for Industry and Applied Mathematics **26**.

Orszag, S.A. and Kells, L.C. (1980) Transition to turbulence in plane Poiseuille flow and plane Couette flow. *JFM* **96**, 159–206.

Orszag, S.A. and Patera, A.T. (1981) Subcritical transition to turbulence in planar shear flows. *Transition and Turbulence* (ed. R.E. Meyer), Academic Press, 127–146.

Orszag, S.A. and Patera, A.T. (1981) Secondary instability of wall-bounded shear flows. *JFM* **128**, 347–385.

Pugh, J.D. (1987) Finite amplitude waves in plane Poiseuille flow. Ph.D. Thesis, Caltech

Pugh, J.D. and Saffman, P.G. (1988) Two-dimensional superhamornic stability of finite amplitude waves in plane Poiseuille flow. *JFM* **194**, 295–308.

Reichardt, H. (1956) Über die Geschwindigkeitsverteilung in einer geradlinigen turbulenen Couetteströmung. *ZAMM* **36**, S26–9, 454.

Rozhdestvenksy, B.L. and Simakin, I.N. (1984) Secondary flows in a plane channel: their relationship and comparison with turbulent flows. *JFM* **147**, 261–289.

Saffman, P.G. (1983) Vortices, stability, and turbulence. *Fourth International Conference on Physiochemical Hydrodynamics* (ed. R. Pfeffer), Annals of the New York Academy of Sciences **404**, 12–24.

Tuckerman, L.S. (1989) Steady-state solving via Stokes preconditioning: recursion relations for elliptic operators. *Proceedings of the Eleventh International Conference on Numerical Methods in Fluid Dynamics* (e.d. D.L. Dwoyer, M.Y. Hussaini and R.G. Voigt) Springer-Verlag, Berlin.

Zahn, J.P., Toomre, J., Spiegel, E.A. and Gough, D.O. (1974) Nonlinear cellular motions in plane Poiseuille channel flow. *JFM* **64** part 2, 319–345.